Master's thesis

NTNU
Norwegian University of Science and Technology
Faculty of Engineering
Department of Mechanical and Industrial Engineering

Bettina Horn Myhre

Effects of chloride, sulfate and pH on the corrosion of tensile wires in grouted tendon ducts in Herøysundet bridge

Master's thesis in Materials Science and Engineering
Supervisor: Roy Johnsen
Co-supervisor: Andreas Erbe, Mette Geiker
June 2022

NTNU
Kunnskap for en bedre verden

Bettina Horn Myhre

Effects of chloride, sulfate and pH on the corrosion of tensile wires in grouted tendon ducts in Herøysundet bridge

Master's thesis in Materials Science and Engineering
Supervisor: Roy Johnsen
Co-supervisor: Andreas Erbe, Mette Geiker
June 2022

Norwegian University of Science and Technology
Faculty of Engineering
Department of Mechanical and Industrial Engineering

NTNU
Norwegian University of
Science and Technology

Preface

This master thesis represents finishing work for the integrated master's degree of Materials Science and Engineering at the Department of Materials Science and Engineering at the Norwegian University of Science and Technology (NTNU). The work included in this thesis was carried out at the Department of Mechanical and Industrial Engineering over the course of 20 weeks during the spring of 2022 and corresponds to 30 credits. This thesis is a continuation of the specialization project written during the fall of 2021.

Professor Roy Johnsen from the Department of Mechanical and Industrial Engineering has been the main supervisor, with professor Andreas Erbe from the Department of Materials Science and Engineering and professor Mette Geiker from the Department of Structural Engineering as co-supervisors. The thesis is being written in cooperation with Statens Vegvesen, which is being represented by Karla Hornbostel.

Firstly, I wish to thank my supervisor, professor Roy Johnsen, for giving me the opportunity to be a part of this project and for his support and guidance during both the specialization project and the master's thesis. By showing an immense interest in the project and by pushing me to reach further, you have given me a deeper understanding and a newfound interest within the field of corrosion. A thank you is also given to my co-supervisors, Andreas Erbe and Mette Geiker, for their appreciated help and valuable inputs during meetings. Then a thank you goes out to Karla Hornbostel and the rest of the representatives from SVV for showing an interest in the work and enthusiasm about the results. I would also like to thank Faezeh Mojtahedi for all her help getting me started with the project and the laboratory work. A big thank you goes out to Cristian Torres Rodriguez for academic inputs and help with laboratory work, but also for the smiles, the good conversations and for making the laboratory a place I enjoyed being.

Lastly, I would like to thank my roommates, friends and fellow students at Materials Science and Engineering for five unforgettable years!

Abstract

The corrosion of steel reinforcement in concrete structures has proven to create problems for a long time, which is why much research have been devoted to discovering the cause. Numerous studies have focused on determining the effect of factors such as pH-levels, aggressive ion concentrations, carbonation, grout conditions and surface conditions. A selection of these studies has been presented in this thesis. The thesis also includes summaries of inspections and preliminary reports performed on Herøysundet bridge, which were used to provide the basis for experimental testing.

Further, this study investigates how chloride and sulfate ions, pH levels and the presence of oxygen effect the corrosion of tensile wires immersed in a saturated $Ca(OH)_2$ solution. Steel samples extracted from Farriseidet bridge were prepared for testing by being grinded, coated to create a specified exposure area and immersed in a concrete pore solution for seven days. The oxide layer built on the surface was found through inspections with scanning electron microscopy (SEM) to consist of $CaCO_3$, which consist with the inspections of oxide layer made on samples extracted from Farriseidet bridge through similar test methods. Corrosion testing were conducted in saturated $Ca(OH)_2$ solutions with varying concentrations of aggressive ions, pH levels and oxygen content, following values measured in inspections of Herøysundet bridge and results from preliminary reports and from the specialization project. Cyclic polarization (CP) curves measured according to ASTM G61 standards revealed a chloride threshold level of 0.0025 M for solutions with a pH of 12.5. The removal of oxygen lead to a decrease in the corrosivity, while the addition of magnesium sulfate made the solution more aggressive. From the CP curves it also became clear that the source of sulfates affects the corrosivity of the solution. Open circuit potential (OCP) and linear polarization resistance (LPR) were measured during long-term exposure, followed by potentiodynamic polarization scans in order to see effects of real exposure conditions. Results suggested chloride threshold values above 0.01 M and gave indications of reduced corrosivity following the removal of oxygen. All tests indicate that ion contents and pH-levels measured in Herøysundet bridge are consistent with levels that cause corrosion attacks on the tensile wires.

Sammendrag

Over lang tid har korrosjon av armering skapt problemer for betong strukturer og det er lagt ned mye forskning for å forstå hva som forårsaker det. Effektene av faktorer som pH-nivå, aggressive ioner, karbonatisering, stål overflate og tilstanden til injeksjonsmassen har vært hovedfokuset til en rekke studier. Et utvalg av disse er presentert i denne oppgaven. I tillegg inneholder oppgaven et sammendrag av inspeksjoner og tidligere rapporter som benyttes som grunnlag for eksperimentelt arbeid.

Oppgavens eksperimentelle arbeid baserer seg på å teste hvordan klorid og sulfat ioner, pH nivå og oksygeninnhold påvirker korrosjonen av spenntråder nedsenket i en mettet $Ca(OH)_2$ løsning. Stål prøver hentet fra Farriseidet bru ble pusset, gitt et bestemt eksponerings område og senket ned i en simulert poreløsning i syv dager før korrosjonstesting. Oksidet som ble dannet på overflaten til stålet ble funnet til å bestå av $CaCO_3$ ved hjelp av et elektronmikroskop. Dette samsvarer med oksidet som ble funnet på spenntrådene hentet fra Farriseidet bru, også testet med et elektronmikroskop. Korrosjonstester ble utført i mettede $Ca(OH)_2$ løsninger med varierende ion innhold, pH verdier og oksygen innhold, og var basert på inspeksjoner og tidligere arbeid utført på Herøysundet bru. Fra sykliske polariseringskurver (CP), målt etter ASTM G61 standarder, ble det funnet en kritisk klorid grenseverdi på 0.0025 M for løsninger med en pH på 12.5. Fjerning av oksygen fra løsningen viser en reduksjon i korrosiviteten til løsningene, mens en tilsats av magnesium sulfat viser en økning. Kurvene viste også at kilden til sulfat spiller en rolle på korrosiviteten til løsningen. For å teste effekten av mer realistiske eksponeringsforhold ble det gjort målinger av åpen krets potensial (OCP) og lineær polariserings motstand (LPR) over lengere eksponeringsperioder, etterfulgt av potensiodynamisk polariserings målinger. Resultatene antydet en kritisk klorid grenseverdi på over 0.01M. I tillegg antydet testene at fjerning av oksygen førte til en reduksjon i korrosivitet. Alle tester gir en indikasjon på at ion innhold og pH-nivå målt i Herøysundet bru tilsvarer nivåer som fører til korrosjonsangrep på spenntrådene.

Contents

Preface . . . . . **i**
Abstract . . . . . **ii**
Sammendrag . . . . . **iii**
Contents . . . . . **iv**
Acronyms . . . . . **vii**
List of Symbols . . . . . **ix**
List of Figures . . . . . **x**
List of Tables . . . . . **xv**
1 Introduction **1**
1.1 Objective 2
1.2 Disclaimers 2
2 Background **3**
2.1 Corrosion of Steel in Concrete Structures 3
2.2 Elements Affecting Corrosion of Steel in Concrete 4
2.2.1 pH-level 4
2.2.2 Oxygen Content 5
2.2.3 Steel Surface Conditions 6
2.2.4 Electrochemical Properties 8
2.2.5 Ion Content 10
2.2.6 Carbonation 13
2.2.7 Galvanic Couplings 14
2.2.8 Concrete Parameters 15
2.2.9 Concrete vs. Grout 16

3 Herøysundet Bridge . . . 18
3.1 Components . . . 18
3.2 Inspections Performed on Herøysundet Bridge . . . 22
3.2.1 A Summary from the Inspections . . . 25
4 Previous Research . . . 26
4.1 Composition of Concrete Pore Solution . . . 26
4.2 Forming an Oxide Layer on the Surface . . . 26
4.3 Corrosion Testing . . . 30
4.4 Previous Research on Herøysundet Bridge . . . 40
5 Method . . . 42
5.1 Outline of Tests . . . 42
5.2 Test Material . . . 42
5.3 Sample Preparation . . . 43
5.4 Oxide Layer Development . . . 44
5.5 Corrosion Testing . . . 44
5.5.1 Electrolyte . . . 44
5.5.2 Exposure Conditions . . . 45
5.5.3 Equipment . . . 46
5.5.4 Corrosion Tests . . . 48
5.5.5 Test Programs . . . 50
5.6 Surface Investigation . . . 52
5.6.1 Oxide Layer . . . 52
5.6.2 Visual Inspections . . . 53
6 Results . . . 54
6.1 Oxide Layer . . . 54
6.1.1 SEM Analysis . . . 55
6.1.2 EDS Analyses . . . 56
6.2 Corrosion Testing . . . 58
6.2.1 Method A . . . 58

6.2.2 Method B . . . 65
7 Discussion . . . 78
7.1 Observations from the Bridge . . . 78
7.2 Experimental Findings . . . 79
7.2.1 Oxide Layer . . . 79
7.2.2 Method A . . . 81
7.2.3 Method B . . . 86
7.3 New Test Methods . . . 91
8 Conclusions . . . 93
9 Recommendations for Future Work . . . 96
Bibliography . . . 97
A Results from Method A . . . I
A.1 Cyclic Polarization Curves . . . II
A.2 Visual Inspections . . . IV
B Results from Method B . . . VII
B.1 OCP Measurements . . . VIII
B.2 LPR Measurements . . . X
B.3 Visual Inspections . . . XII
C Results from Oxide Layer Analysis . . . XVI
C.1 Mapping Analysis . . . XVI
D Results from the Specialization Project . . . XIX
D.1 Method A . . . XIX
D.2 Method B . . . XXIII
D.3 Oxide Layer . . . XXVI
E Images From the Site . . . XXXII
E.1 Focus on corrosion . . . XXXII
E.2 Focus on the grout . . . XXXV
F Image descriptions . . . XXXVIII

Acronyms

C_3A tricalsium aluminate. 12, 13

CCTL critical chloride threshold level. 10, 11

CP cyclic polarization. ii, 32, 37, 38, 42, 59–63, 66, 81–86, 93

DEF delayed ettringite formation. 12, 13

EDS energy-dispersive X-ray spectroscopy. 53, 54, 57, 79, 80

EIS electrochemical impendance spectroscopy. 34, 37

ITZ interfacial transition zone. 16

LPR linear polarization resistance. ii, 27, 30, 37, 40, 42, 46, 49, 52, 65, 70, 72, 74–76, 81, 89, 90, 94

NDT non-destructive testing. 22

OCP open circuit potential. ii, 8, 27–29, 33, 34, 40–42, 44, 46, 48–50, 55, 59, 60, 62, 64–67, 71, 72, 74–76, 81–86, 88, 89, 94

OM optical microscope. 53, 75–77

RC reinforced concrete. 1, 3

RH relative humidity. 8, 11, 13, 15

SCE saturated calomel electrode. 9, 10, 27–29, 32, 35, 37

SCI steel-concrete interface. 16, 17

SCM supplementary cementitious materials. 13, 15, 17

SEM scanning electron microscopy. ii, 7, 42, 43, 52–54, 56, 79, 80, 93

SHE standard hydrogen electrode. 8, 9

SVV Statens Vegvesen. i, 1, 22, 23

ZRA zero resistance ammetry. 37, 39

List of Symbols

Symbol	Standard unit	Definition
A	cm^2	Area
α	-	Composite transfer coefficient
B	V	Stern-Geary constant
b_a	mV/decade	Anodic Tafel constant
bc	mV/decade	Cathodic Tafel constant
E	V	Electrochemical potential
E_{corr}	V	Corrosion potential
E_{pass}	V	Passivation potential
E_{pit}	V	Pitting potential
E_{rep}	V	Repassivation potential
F	C/mol	Faraday constant
I	A	Current
I_{corr}	A	Corrosion current
I_{pass}	A	Passive current
I_{pit}	A	Pitting current
i_A	A/m	Anodic current density
i_C	A/m	Cathodic current density
i_{corr}	A/m^2	Corrosion current density
i_{pass}	A/m^2	Passive current density
i_{pit}	A/m^2	Pitting current density
R	J/K mol	Gas constant
R_P	Ω	The linear polarization resistance
T	K	Temperature
v_{corr}	mm/year	Corrosion rate
w/b	-	Water-to-binder
w/c	-	Water-to-cement

List of Figures

2.1 The Pourbaix diagram of $Fe - H_2O$. 4

2.2 Relative volume of iron and some of its oxides. 6

2.3 SEM image of cross section, depicting an as received sample with mill scale. 7

2.4 An illustration of polarization and overvoltage curves. 8

2.5 Anodic polarization curves for iron in water and concrete. 9

2.6 Cathodic polarization curves in concrete given different moisture levels. 10

2.7 An illustration of i_{corr} and E_{corr} from anodic and cathodic polarization curves of steel in concrete. 10

2.8 An illustration of chloride-induced pitting corrosion. 11

2.9 A schematic presentation of a cyclic polarization curve. 12

2.10 An illustration of macrocell corrosion due to local differences in passivity. 14

2.11 Porosity next to the ITZ and SCI. 16

2.12 A schematic representation of size gradation of aggregates. 17

3.1 A sketch of the bridge and the cross section containing the tendon ducts. 18

3.2 An illustration of the reinforcement in Herøysundet bridge. 19

3.3 Typical post-tensioned tendon placement. 20

3.4 A typical post-tensioning anchorage for wire tendonds. 20

3.5 Images of tendon ducts in Farriseidet bridge. 21

3.6 Inspection areas on Herøysundet bridge. 22

3.7 Tendon duct and tensile wires. 23

3.8 Grout gathered from different locations in the bridge. 23

4.1 Results from a study by Chen et al. 28

4.2 Polarization curves measured by Krishna Vigneshwaran et al. 31

4.3 Cyclic polarization curves measured by Xu et al. for different salts. . . 32

4.4 Polarization curves for different levels of Cl^- for the pre-stressed wires measured by Moser et al. 33

4.5 The results from Li et al. showing the evolution of corrosion potential as the chloride content increase over time. 35

4.6 Results from tests for single wire specimen under different test environments measured by Lee and Zielske. 36

4.7 An illustration of the sample designs and setup for coupled cells used by Dong and Poursaee. 38

4.8 The potential development for different passive/active areas following the research of Dong and Poursaee. 38

4.9 Specimens used in the research by Castel et al. after sawing and coating was performed. 39

4.10 Setups used to monitor macrocell corrosion in the research by Castel et al. 40

4.11 A summary of the results found in the report by Roy Johnsen. 40

5.1 Test materials from Farriseide bridge. 43

5.2 Test sample dimensions and marked areas with and without coating. . 44

5.3 An illustration of the experimental setup for the buildup of an oxide layer. 45

5.4 Equipment for ASTM G61 tests. 46

5.5 Equipment for long-term tests. 47

5.6 Correlations between common electrodes. 47

5.7 Test programs - method A. 51

5.8 Test programs - method B. 52

6.1 OCP measurements made during the development of oxide layers on the surfaces. 55

6.2 Image taken with SEM at a magnification of 5000x. 56

6.3 Overview of the sites used for the point analysis on the as-delivered sample. 56

6.4 Shows the element overlay map with color explanations and results from the EDS mapping analysis of the as-delivered sample. 57

6.5 All CP plots measured according to method A. 60

6.6 CP plots of solutions with a pH of 12.5 and varying chloride concentrations. 61

6.7 CP plots of solutions with a pH of 13 and varying ion concentrations. . 62

6.8 CP plots of solutions containing sulfate 63

6.9 OCP development in different solutions. 67

6.10 Solution 4. 68

6.11 Tests run with and without a pre-made oxide layer. 69

6.12 Corrosion current density for all solutions tested. 70

6.13 Corrosion current density for all solutions with a pH of 12.5 and 13. . . 72

6.14 Potentiodynamic scans performed after ended OCP/LPR measurements for solutions in method B. 73

6.15 OM imaging of solution 15. 76

6.16 OM imaging of solution 10. 76

6.17 OM imaging of solution 9. 77

7.1 A comparison of the different oxide layers. 80

7.2 CP plots of solutions containing sulfates. 84

7.3 CP plots of solutions with a chloride concentration of 0.1 M. 85

7.4 OCP developments in solution 5B and 19. 88

7.5 OCP vs. i_{corr}. 89

7.6 Illustration of the average slope of the anodic branch. 91

A.1 All individual CP curves measured according to method A. III

A.2 Images depicting the situation after ended CP measurements for the corroded samples. V

A.3 Visual inspections of samples displaying signs of corrosion. VI

B.1 OCP measurements performed using either or both a Gamry potentiostat and a potential logger. IX

B.2 Plot showing the OCP development for all solutions during the exposure time. X

B.3 Corrosion rates for all solutions tested. X

B.4 Corrosion rates for solutions with a pH of 12.5. XI

B.5 Corrosion rates for solutions with a pH of 13. XII

B.6 Image depicting the situation after ended OCP/LPR and polarization measurements for solution 19. XII

B.7 Visual inspections of samples displaying signs of corrosion. XIII

B.8 OM imaging of solution 13. XIV

B.9 OM imaging of solution 14. XIV

B.10 OM imaging of solution 16. XV

B.11 OM imaging of solution 21. XV

B.12 OM imaging of solution 22. XV

C.1 Live map from EDS mapping analysis. XVI

C.2 The sum of the spectrum recorded during the mapping analysis. XVI

C.3 Individual element overlays from the EDS mapping analysis. XVIII

D.1 Plot showing all cyclic polarization curves measured according to ASTM G61 during the specialization project. XIX

D.2 Images depicting the situation after ended measurements for a selection of the samples. XXI

D.3 Visual inspections on the samples that showed corrosion. XXII

D.4 Sample 5 after 14 days of testing. XXIV

D.5 OCP development for solution 5 during 2 weeks of exposure. XXIV

D.6 Calculated corrosion current density development based on LPR measurements during 2 weeks of exposure. XXV

D.7 Calculated corrosion rate development based on LPR measurements during 2 weeks of exposure. XXV

D.8 The potential development on sample during the buildup of oxide layer. XXVI

D.9 Left sample: with oxide layer. Right sample: without oxide layer. XXVI

D.10 Image taken with SEM at a magnification of 5000x. XXVII

D.11 The overview over the sites used for the point analyses. XXVII

D.12 Spectrum analyses from the EDS point analysis. XXVIII

D.13 Shows the element overlay map with explanations and results from the EDS mapping analysis. XXIX

D.14 Live map from EDS mapping analysis. XXIX

D.15 Shows the sum of the spectrum recorded during the EDS mapping analysis.XXX

D.16 Individual element overlay from EDS mapping analysis. XXXI

E.1 Images of corrosion from inspection site 1. XXXII

E.2 Images of corrosion from inspection site 2. XXXIII

E.3 Images of corrosion from inspection site 3. XXXIV

E.4 Images of the grout from inspection site 1. XXXV

E.5 Images of the grout from inspection site 2. XXXVI

E.6 Images of the grout from inspection site 3. XXXVII

List of Tables

3.1 The chemical composition of the wire given in wt%. 20

3.2 Select U.K. Grout requirements. 21

3.3 The elements found in the grout after analysis by SINTEF. 24

3.4 Moisture content measured in grout samples by SINTEF. 24

3.5 The composition of the pore solution measured by SINTEF. 24

4.1 Composition of synthetic pore solution in the research by Poursaee et al. 27

4.2 Composition of the solution used in the research by Chen et al. 27

4.3 Composition of the solution used in the research by Ghods et al. 29

4.4 Compositions of the solutions used for electrochemical tests in the research by Krishna Vigneshwaran et al. 30

4.5 Composition of simulated concrete pore solution used in research by Moser et al. 33

4.6 The solutions created for the experimental testing in the research by Li et al. 34

4.7 The chemical composition of the test solutions used in the research by Lee and Zielske. 36

4.8 Composition of the solution used for testing in the research by Dong and Poursaee. 37

5.1 Composition of the synthetic pore solution used for creating an oxide layer on the samples. 44

6.1 Average results from the point analysis performed on the as-delivered sample. 57

6.2 Results from the mapping analysis performed on the as-delivered sample. 58

6.3 Results from method A. 59

6.4 The percentage of the surface area subjected to corrosion. 64

6.5 Results from method B. 65

6.6 Tafel constants measured from potentiodynamic scans performed after ended OCP/LPR measurements. 74

6.7 The percentage of the surface area subjected to corrosion. 75

B.1 Results from method B. XI

D.1 Results from method A - specialization project. XX

D.2 The percentage of the surface area subjected to corrosion. XXIII

D.3 Results from method B - specialization project. XXIII

D.4 Lists the average results from the EDS point analysis given in Figure D.12.XXVII

D.5 Results from the EDS mapping analysis. XXIX

D.6 Results from the FeL/O K/CaK/C K phase (blue area). XXX

Chapter 1

Introduction

Reinforced concrete (RC) is one of the most common types of structural materials used due to low costs, wide availability of raw materials and because in most cases it exhibits good performance and high durability. As is the case when dealing with metal components, the risk of corrosion is always present. The passive layer that forms on the surface of the steel when immersed in concrete was formerly thought to make the reinforcement resistant towards corrosion, however time has revealed that this layer can be broken down. Many factors can cause the loss of passivity, and various researchers have investigated how these different factors affect the corrosion of steel reinforcement in concrete. Important factors such as aggressive ions [1–4], the lack of grout in contact with the steel [5] and decreases in pH-level [6, 7], have all been discovered to have an impact on the service life of RC structures.

Statens Vegvesen (SVV) is responsible for the construction and maintenance of a number of concrete bridges in Norway, which uses reinforcement in order to secure the desired strength. Inspections have revealed that the reinforcement in some cases had not shown any signs of corrosion after more than 30 years of service, while in other cases, severe corrosion attacks had occurred only years after the bridge was completed.

The corrosion of the tensile wires observed in Herøysundet bridge provides the background for this thesis, and the main focus will be on determining the effects of some of the elements that could be the source of the corrosion. In Herøysundet bridge, the reinforcement is made up of tendon ducts containing strung up and prestressed tensile wires embedded in grout. All the components mentioned are affected on different levels, but the most critical component affected is the corroded tensile wires. This thesis will include theory on typical elements affecting corrosion in concrete, information regarding the bridge and an overview of some of the previous research published on the sub-

ject. Furthermore, scientific experiments are carried out to determine how the different factors affect the corrosion rates of the tensile wires in question. Previous studies have been performed on as-delivered samples from the bridge, whereas this thesis will use samples that have been pre-treated for the purpose of recreating the surface conditions present on steel when embedded in grout.

1.1 Objective

The objective of this thesis is to determine the effects of the different elements that could potentially be the cause of corrosion found on the tensile wires in Herøysundet bridge. Research questions that are relevant:

- Will pre-treatments effect how the different elements affect corrosion?
- What factors affect the corrosion of the wires the most?
- Can a combination of factors have worsened the corrosion?
- With regards to pH-levels and chloride contents, are there any limiting values for corrosion initiation?
- What can we learn from earlier published work on the same topic?
- Are there any new test methods that can be used in order to take into account the complexity of the environment inside voids in tendon ducts?

1.2 Disclaimers

This thesis is a continuation of a specialization project performed during the fall of 2021. Therefore, parts of the background, research and findings made during that project have been included in this thesis. Experimental work builds on the work performed during the specialization project, and results from this thesis will be compared to the previous work. Previous results are therefore displayed in the appendixes, see section D.1, D.2 and D.3.

Chapter 2

Background

2.1 Corrosion of Steel in Concrete Structures

The use of steel reinforcement in concrete structures is a common practice as it increases the strength of the structure. However, there have been numerous reports of corrosion found on the reinforcement, which can affect the structure's life expectancy and durability [8]. The service life of reinforced concrete (RC) can be broken down into two phases: initiation and propagation [9]. The initiation phase begins as the steel loses its passivity due to external factors and corrosion is initiated. In this phase, the structure is still functioning as designed to. When the protective layer begins to dissolve due to depassivation, the second phase has begun. Corrosion now proceeds at different rates depending on environmental conditions such as humidity and temperature. As the reinforcement deteriorates, the second phase continues until the component no longer serves its purposes.

In order for corrosion to arise on the reinforcement, certain conditions need to be in place. Most types of corrosion require the presence of moisture and oxygen, as well as a breakdown of the protective layer on the surface of the steel, to be initiated [8, 10]. The corrosion of the reinforcement is affected by the environment present inside the concrete and external conditions that are able to diffuse through. Moisture in the form of pore solution will always be present within the pores of concrete, which allows for oxygen to diffuse through. There are several factors that can further influence the corrosion initiation and the corrosion rate, such as pH level, steel surface conditions, chloride- and sulfate content, and several related to the quality of the concrete, see Section 2.2.

2.2 Elements Affecting Corrosion of Steel in Concrete

2.2.1 pH-level

In general, concrete provides a good protection against corrosion due to the high alkalinity of the pore solution. As can be seen in Figure 2.1, high pH levels keep the steel in a passive state. The level of alkalinity is therefore one of the main parameters determining whether or not corrosion can be initiated [11].

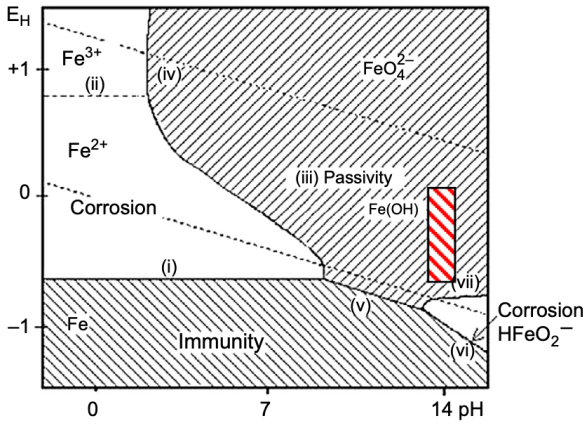

Figure 2.1: Pourbaix diagram showing the passive, active and immune area of $Fe - H_2O$ [12].

If concrete is not subjected to external influences, it usually exhibits a pH between 12.5 and 13.5, ensuring that the steel is within the passive state area. In Figure 2.1, a red area is drawn, marking a typical potential-pH region for steel in concrete. Below a pH level of ~ 9, there is a risk of the steel entering into an active area, depending on the electrochemical potential. Above a pH of 13.5, the steel can once again enter an active area where corrosion is possible. When the steel is within the passive area, a thin protective oxide layer forms on the surface (<10 nm) [13, 14]. This layer is made up of corrosion products that form on the surface, and due to a high permeability, makes the rate of corrosion become extremely low (~ 0.1 μm/year) [15]. Passive film formation begins with the dissolution of the metal, represented by Equation 2.1 [13, 16]. This reaction is the anodic part of the two half-cell reactions taking place during the electrochemical process that is corrosion of steel [17].

$$Fe \rightarrow Fe^{2+} + 2e^{-} \tag{2.1}$$

The protective oxide layer that forms on the surface of the steel as it comes into contact

with concrete usually consists of Fe^{3+} and Fe^{2+} rich oxides [18]. The protective Fe^{2+} rich oxides form a thin oxide film in contact with the surface, while the Fe^{3+} layer form near the free surface. As the immersion in concrete continues and there is a surplus of ions available to diffuse towards the surface, the Fe^{3+} layer will continue to grow thicker through the formation of new oxides and through mechanisms of mass transportation, causing a more robust and protective layer [19–21]. For corrosion to occur, the passive oxide layer has to be broken down. This process is known as depassivation.

2.2.2 Oxygen Content

Oxygen has several roles when it comes to the protection of, as well as the corrosion of steel in concrete environments. Along with moisture, oxygen is essential for the breakdown of the passive layer [9, 22]. In passive conditions, oxygen must be dissolved in the pore solution in order to take part in a cathodic reaction that thickens the passive layer [22]. The amount of oxygen available around the steel reinforcement determines what type of cathodic reaction takes place on the surface [23]. The amount also contributes to controlling the corrosion rates. If the oxygen diffusion towards the steel becomes limited, the cathodic reaction rate slows down, causing the corrosion rate to slow over time. [16, 24].

There are two cathodic reactions that can take place, and the one that becomes the dominant reaction depends on pH level, potential level and the amount of oxygen available. Given enough oxygen present, the dominating cathodic reaction will be an oxygen reduction reaction, see Equation 2.2. If there are very low levels of oxygen present, the dominant reaction will be in the form of hydrogen evolution, see Equation 2.3. The electrons consumed in the cathodic reactions stem from the anodic half-cell reaction given in Equation 2.1. For hydrogen evolution to become the dominant reaction there has to be a depletion of oxygen and highly negative potentials, as is the case in pits and crevices, Section 2.2.5, [9, 24]. Therefore, oxygen reduction is in most cases the dominant cathodic reaction.

$$\frac{1}{2}O_2 + H_2O + 2e^- \rightarrow 2OH^-. \tag{2.2}$$

$$2H^+ + 2e^- \rightarrow H_2. \tag{2.3}$$

Even though oxygen is usually present for initiation of corrosion, it is not required for the continuation. Corrosion can proceed with the reduction of the oxides or hydroxides

formed and with water hydrolysis, but the presence of oxygen can intensify the corrosion process [16, 22]. The iron ions in the passive film will react further, and depending on the amount of oxygen present, different anodic reactions are possible. [14, 16]. A common type of corrosion product to form is Fe_2O_3, which forms as the iron ions in the solution reacts with hydroxides and oxides, see Equation 2.4 [13, 25].

$$\begin{aligned} Fe + 2OH^- &\rightarrow Fe(OH)_2 \\ 4Fe(OH)_2 + O_2 + 2H_2O &\rightarrow 4Fe(OH)_3 \\ Fe(OH)_3 &\rightarrow Fe_2O_3 * H_2O + 2H_2O \end{aligned} \tag{2.4}$$

When the access to oxygen becomes limited, the initial iron hydroxides will react further to create corrosion products such as Fe_3O_4 [26]. If the film becomes composed primarily of Fe_3O_4, the corrosion rate will become similar to that of a film free surface as the layer is porous which allow for ions to diffuse easily through.

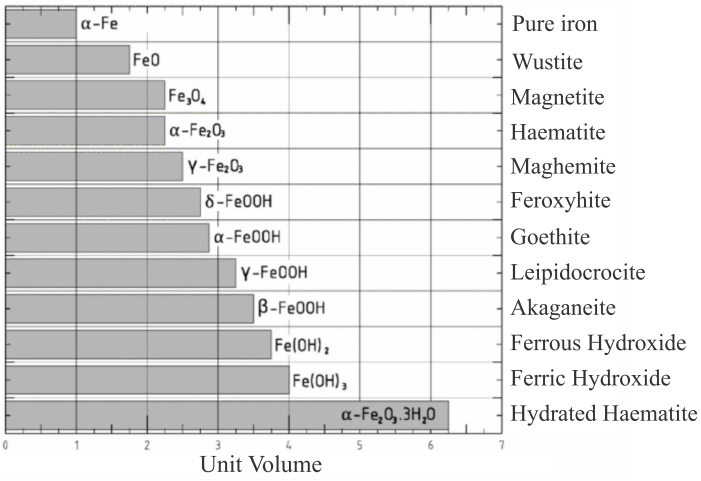

Figure 2.2: Relative volume of iron and some of its oxides [27].

The formation of the different corrosion products leads to varying increases in volume, which again can lead to crack formation in the concrete [14, 27]. When the corrosion products become hydrated, they take up an even bigger volume, see Figure 2.2. Cracks in the concrete can cause exposure of the reinforcement to the atmosphere.

2.2.3 Steel Surface Conditions

The state of the surface of the steel will play a role in what chemical and electrochemical reactions take place [5]. Typically, the surface is either consisting of bare steel, covered

with mill scale or covered with pre-existing rust. If the surface of the steel consists of bare steel, it will passivate when immersed in alkaline, chloride free environments. This will create a passive film on the surface, as previously mentioned.

Steel subjected to hot rolling tend to form an oxide layer on the surface known as mill scale. This layer is made up of iron oxides, typically FeO, Fe_3O_4 or Fe_2O_3 [28]. These layers of oxides vary in thickness and are often brittle. This creates a high risk of cracks forming if the steel is not handled with care. On the interface between the mill scale and the steel substrate there are often voids and crevices present, see Figure 2.3 [29, 30]. Cracks in the mill scale can cause pore water to fill these voids and crevices, causing corrosion beneath the mill scale layer. Even though the mill scale is stable in the alkaline pore solutions, it it less protective against corrosion than the passive film created on bare steel due to the imperfections that are present.

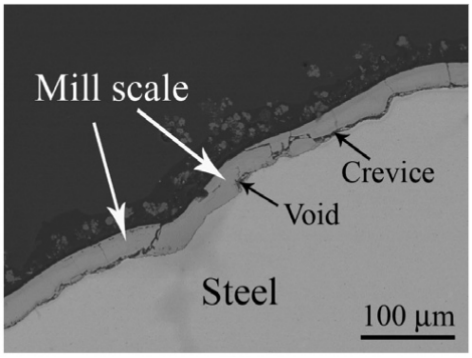

Figure 2.3: SEM image of cross section from research by Ghods et al., depicting an as received sample with mill scale. [29].

Between being manufactured and being mounted in its intended structure, the steel may be exposed to situations that can cause the surface to corrode. These layers of superficial rust usually consist of FeOOH, with traces of Fe_2O_3 and Fe_3O_4 also present [31–34]. The hydroxide layer is naturally porous and adheres poorly to the substrate. This makes it easy for corrosive species to penetrate the rust layer, which causes the steel surface to corrode further underneath.

Another surface parameter that play an important role in the corrosion process of steel is the surface roughness. A smoother and polished surface will provide better resistance against localized attacks as there are less possible initiation sites. The smooth surface will also be able to form a firmer passive layer that will be harder to penetrate [7, 35, 36]. These highly polished surfaces are often used for laboratory testing and will not necessarily represent the surface conditions of the steels used on site. The variation of surface roughness can explain why some rebars corrode under low chloride situations, while other remain passive with much higher chloride concentrations present.

2.2.4 Electrochemical Properties

Another important parameter controlling whether or not corrosion can be initiated is the electrochemical potential, E, on the surface of the steel [11]. The passive surface layer is affected by parameters such as cement type, temperature, porosity, RH, oxygen content and the surface roughness of the steel, but also by the electrical potential on the steel surface [37], see Figure 2.1. It is the electrochemical potential that determines the rate of the anodic and cathodic process that takes place during corrosion [16]. By using polarization curves the corrosion behavior can be described by relating the potential to the anodic or cathodic current, as displayed in Figure 2.4.

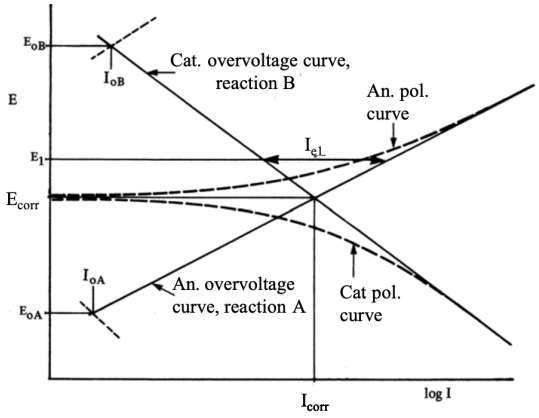

Figure 2.4: An illustration of polarization and overvoltage curves [38].

The polarization curve plots the logarithm of the external current as a function of the potential with respect to both the anodic and cathodic reaction current. The overvoltage curves, also called Tafel lines, are found by extrapolating the polarization lines [38].

Iron submerged in water will give an anodic polarization curve as shown in Figure 2.5a, measured against a standard hydrogen electrode (SHE). The corrosion potential is the potential that the electrode has when no external current is applied [39]. This potential is often denoted E_{corr} or E_0, and is the same as the open circuit potential (OCP). When the potential is below the corrosion potential, denoted E_0 in Figure 2.5a, iron has a tendency for oxidation, leaving it in an immune state [16]. In the area above the passivation potential, E_{pass}, the anodic current density is again very low, resulting in the thin passive oxide layer forming on the surface. The low current density corresponds to low dissolution rates, which is why the steel is in a passive state. Current density values between 0.1 and 1 $\mu\mathrm{A/cm}^2$ are typically considered passive [36, 40]. In between E_0 and E_{pass} the passive oxide layer does not form on its own, leaving the steel in an active state of corrosion.

In solutions simulating the conditions of concrete the polarization curve will look somewhat different, see Figure 2.5b, where the anodic polarization curve is measured against a saturated calomel electrode (SCE). As can be seen in Figure 2.5b, the addition of carbon and chlorides will minimize the passive area, making the steel reach an active state at lower potentials.

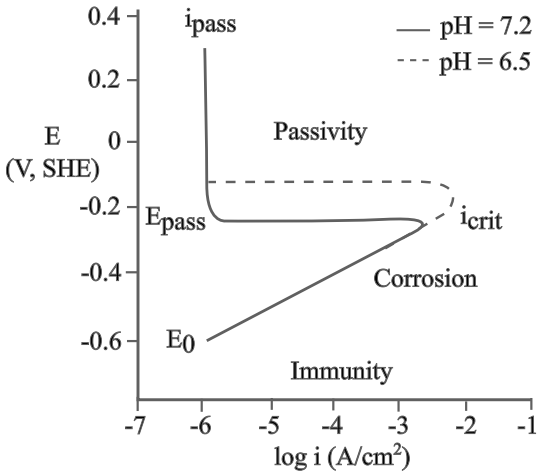

(a) The anodic polarization curves for $Fe - H_2O$ measured against a SHE [38].

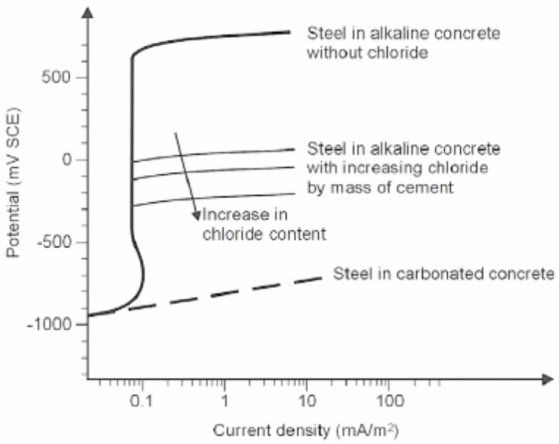

(b) An illustration of the anodic polarization curve of steel measured against a SCE in concrete with chlorides and carbon [16]

Figure 2.5: Anodic polarization curves for iron in (a) water and (b) concrete.

The cathodic polarization curves are determined by the kinetics of oxygen reduction [16]. Below potentials of 0 mV vs. SCE, the rate of the cathodic process is dependent on the amount of oxygen available on the steel surface, see subsection 2.2.2. The rate of the cathodic process and the corrosion potential also decreases with the increase of moisture content in the concrete, see Figure 2.6. Hydrogen evolution, Equation 2.3, will start alongside oxygen reduction when reaching potential levels below -900 mV vs SCE. When there is no oxygen present, i.e. in a completely saturated concrete, the only possible cathodic process will be the hydrogen evolution.

$$2H^+ + 2e^- \rightarrow H_2. \qquad \text{(2.3 revisited)}$$

When combining the plots of the anodic and cathodic curves it is possible to find the corrosion current density, i_{corr}, and the corrosion potential, E_{corr}, from the intersection between the two, see Figure 2.7. E_{corr} and i_{corr} can be found from the intersection given that the ohmic drop is negligible [16].

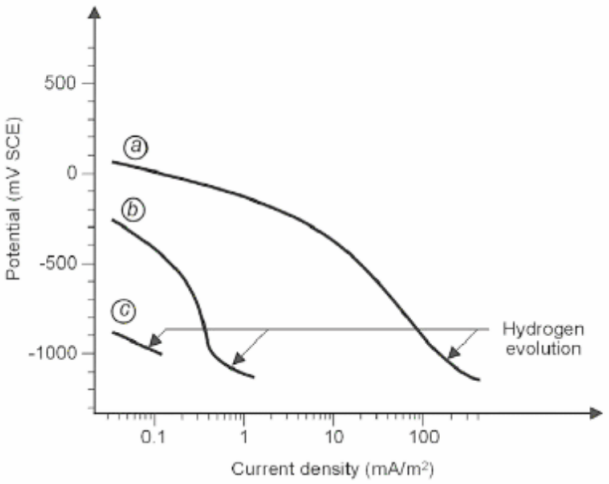

Figure 2.6: An illustration of the cathodic polarization curve of steel in concrete measured against SCE. Divided by different moisture content: (a) semidry; (b) wet; (c) completely saturated [16].

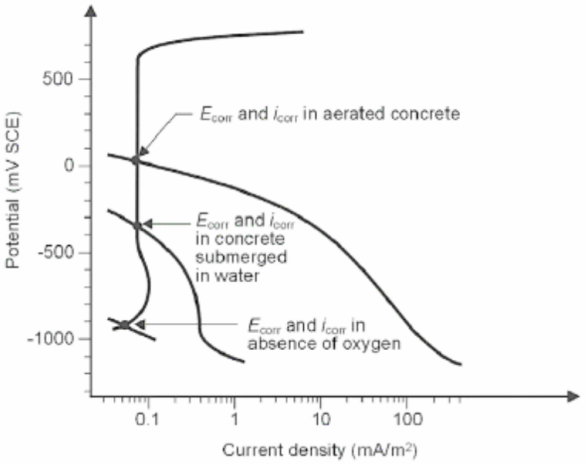

Figure 2.7: An illustration of i_{corr} and E_{corr} from anodic and cathodic polarization curves of steel in concrete [16].

2.2.5 Ion Content

Chlorides

As mentioned previously, for corrosion to proceed, the passive layer needs to be broken down. One of the most common ions to attack the steel and break down the passive surface layer is the chloride ion [41]. When a critical chloride threshold level (CCTL)

is reached a breakdown of the passive layer can occur, depending on the potential on the surface of the steel [42]. This critical chloride threshold level is not a set value but vary with factors such as the pH level, concrete properties, w/c ratio, relative humidity (RH), the surface roughness of the steel and the source of the chlorides, among others [6, 37, 42, 43]. This being said, the American Concrete Institute (ACI) has set an ASTM standard called ACI 318-08 that states that the chloride ion by weight of cement ratio should not exceed 0.06 percent by weight of cement for prestressed concrete [44] Similar limits have been set by other design codes from America, Canada and New Zealand, while Europe and Hong Kong have set limits at 0.10 kg/m^3 for prestressed concrete [45].

In concrete, the chloride ions can either come from internal or external sources [46]. External sources are typically environmental factors such as seawater in marine environments or deicing salts in colder environments. Internal sources for chloride ions usually come from chloride containing admixtures, contaminated aggregates or from the mixing water. Regardless of the source, the chlorides can either be dissolved in the pore solution, known as free chlorides, or they can be bound to the cement hydrates, known as bound chlorides. Only the free chloride ions are able to initiate localized breakdowns of the passive layer, which can allow for pitting corrosion to occur [8, 35, 47].

When the chloride ions have managed to break through the passive layer, a pit or crevice is formed where a local "differential environmental cell" is created [48]. An oxygen depletion will take place in the pit, making the local environment more acidic than the one surrounding the passive film, and hydrogen evolution becomes the dominant anodic reaction. From here on, the growth becomes autocatalytic as the chloride ions are not consumed in the process, but continue to react further with the metal, see Figure 2.8. The local corrosion system created, with an adjacent active and passive area as shown in Figure 2.8, is known as a microcell.

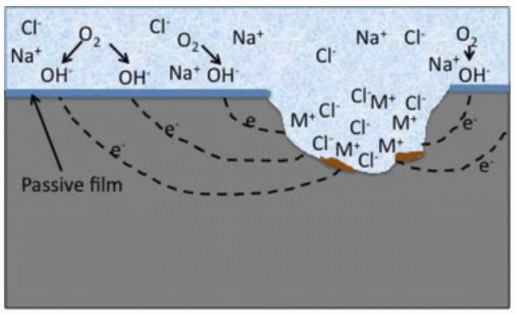

Figure 2.8: An illustration of how chloride-induced pitting corrosion takes place on a metal with a passive layer [49].

The potential required for the chlorides to locally break down the passive layer is known as the pitting potential, E_{pit}, [38]. By analyzing the anodic polarization curves the pitting potential can be found as shown in Figure 2.9. In an active pit, the lower limit for corrosion is given by the repassivation potential, E_{rep}. Therefore, the critical potential must be more positive than the repassivation potential in order to initiate corrosion.

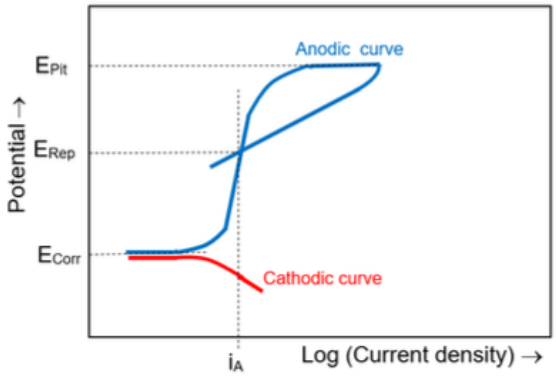

Figure 2.9: A schematic presentation of a cyclic polarization curve depicting E_{Corr}, E_{Pit} and E_{Rep} [50].

Sulfates

Another type of ion known to affect the corrosion of steel in concrete is the sulfate ion. These ions can either come from infiltration from external sources like groundwater and soils or from the concrete itself [51, 52]. In external sulfate attacks, the sulfate ions can react with either calcium hydroxide or tricalsium aluminate (C_3A) in the concrete and form gypsum and ettringite, respectfully [51, 53–55]. Both reactions are presented in Equation 2.5 and 2.6.

$$Ca(OH)_2 + SO_4^{2-} + 2H_2O \rightarrow CaSO \cdot 2H_2O + 2OH^- \tag{2.5}$$

$$C_3A + 3CaSO_4 + 32H_2O \rightarrow 3CaO \cdot Al_2O_3 \cdot 3CaSO_4 \cdot 32H_2O \tag{2.6}$$

The most important reaction of these two is the formation of ettringite, Equation 2.6, as it forms as crystals that causes greater expansive effects. If secondary ettringite develops in the walls of air voids, it become stable and will not cause cracking of the cement [51, 54]. However, internal sulfate attacks can result in delayed ettringite formation (DEF).

A problem then arises as the delayed ettringite formation (DEF) forms as massive clusters, which can lead to a swelling of the concrete that may increase microcracking and capillary porosity.

Different salts are known to have different effects. Particularly, the magnesium sulfate, ammonium sulfate and sodium sulfate are known to disrupt the integrity of the reinforcement [2, 51]. High concentrations of free sulfates can inhibit the formation of the passive surface layer, making way for general corrosion. When found in crevice environments they can allow for localized corrosion. The most common modes of deterioration caused by sulfates are the acidic type and the expansive type. In the acidic type, the hydrated cement paste is reduced to granular mass, which creates voids next to the reinforcement. The second mode causes cracking of the cement and therefore exposure to the environment.

In addition to raising problems on their own, the sulfate ions can also affect the effect chloride ions have on corrosion [56–58]. A presence of sulfate ions will not speed up the corrosion initiation process but it can increase the corrosion rate. A use of supplementary cementitious materials (SCM) can minimize deterioration caused by sulfates due to a reduction of C_3A.

2.2.6 Carbonation

Carbonation is a problem that arise when the concrete come into contact with air, as calcium hydroxide, $Ca(OH)_2$, in the concrete reacts with CO_2 from the air and water [14], see Equation 2.7.

$$Ca(OH)_2 + CO_2 \rightarrow CaCO_3 + H_2O \tag{2.7}$$

The carbonation process is dependent on water and therefore concrete parameters, such as the RH, the w/c-ratio and the moisture content of the aggregates, are important parameters influencing the rate of carbonation [8, 59]. Carbon dioxide diffuses through the concrete pores and the reaction reduces the pH value of the concrete to below 9, which is low enough to depassivate the steel. As the passive layer breaks down, a relatively homogeneous corrosion process takes place. The corrosion products are soluble and therefore often diffuse to the surface of the concrete causing visible rust stains.

2.2.7 Galvanic Couplings

When local differences in the electrochemical state gets generated on separate locations of the surface of the reinforcement steel, a macrocell may form [14, 17, 60]. In this case, the steel can have both active and passive surfaces that are spatially separated from to each other. Macrocells arise due to local depassivation, which can be the result of local areas with high chloride concentrations, partial carbonation or when the steel gets partly covered by grout and partly exposed to a void. This creates a galvanic coupling between the passive steel and the depassivated steel and causes a current to flow between the two, see Figure 2.10. The current is known as the macrocell current and is highly dependent on the conductivity of the electrolyte surrounding the steel [38].

Due to nobility, the active area will function as an anode, while the passive area becomes the cathode [38]. The current circulating from the anode to the cathode will contribute to accelerate the corrosion attack on the active surface simultaneously to increasing the passivity on the passive surface. A larger difference in free corrosion potential, E_{corr}, between the passive and active surface will cause a higher magnitude of the macrocell current. However, the current will decrease as the dissipation produced at both surfaces increase. In addition to the magnitude of the macrocell current and the conductivity of the electrolyte, another factor determining the corrosion rate on the active steel is the area ratio between the active and the passive steel [38, 61, 62].

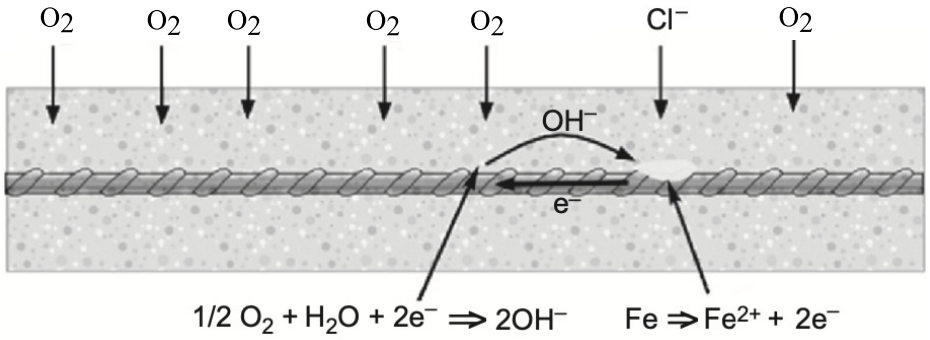

Figure 2.10: An illustration of macrocell corrosion due to local differences in passivity [14].

In chloride contaminated situations, the amount of oxygen present around the passive metal will control the macrocell current [38]. With a sufficient amount of oxygen present, the galvanic coupling will increase the alkalinity surrounding the passive steel. In such cases, the macrocell will contribute to maintaining the passivity on the passive steel as the active steel corrodes as explained above. However, when the amount of oxygen is limited, the macrocell current will be reduced over time as the oxygen is consumed.

This will result in a lowering of the potential on the passive steel until it reaches levels similar to that of the corroding steel.

2.2.8 Concrete Parameters

The main constituent in concrete is Portland cement, which is rich in hydroxides of calcium, potassium and sodium [63, 64]. These contribute to the alkaline pH levels, which, as mentioned previously, gives the concrete its protective properties. This being said, the factors mentioned in the previous sections are able to decrease the protectiveness of the concrete. In order for chloride ions or carbon dioxide to diffuse through the concrete, certain concrete parameters come into play. The transport and diffusion rates are dependent on the porosity, permeability, curing time and temperature, w/b-ratio or w/c-ratio and aggregate size [14, 64–66].

There are several types of porosity in cement paste, but it is the capillary pores that are the most critical. They are the largest of the pores and it is their interconnectivity that sets the limit for diffusion of chloride ions, CO_2, oxygen and moisture through the concrete. The capillary porosity is affected by the w/b-ratio, admixtures and the use of supplementary cementitious materials (SCM) [67]. A higher w/b-ratio will increase the interconnectivity of the capillary pores, leading to increased diffusion. An advantage with admixtures, like plasticizers, is the ability to lower the water needed to give the same workability of the fresh concrete. For that reason will an addition of plasticizers lower the w/b-ratio and consequently the porosity. A use of SCM, such as silica fume, can also contribute to reduce the connectivity of the capillary pores [65, 66].

The relative humidity (RH) is another factor that can affect the permeability of the concrete. It is the intermediate levels of the RH that allow for the highest rates of diffusion [15, 68]. At low RH levels, the corrosion rate is low due to limited conductivity. When the RH becomes to high, the corrosion rate again decreases due to the limited amount of oxygen present. Other important parameters affecting permeability are the curing conditions, especially the curing time [69]. Increasing the curing time will make the structure denser and therefore make diffusion harder [14, 70].

As corrosion is not only affected by what is able to diffuse through the concrete, it is also important to consider what is already inside the concrete. Within the pores of the concrete there is a fluid that is left after the hydration process is finished. This pore solution consists of elements that it absorbs from the concrete, such as CaO, K_2O and Na_2O [5, 71, 72]. The pore solution provides a presence of moisture needed for corrosion to initiate [30]. In cases where the w/c-ratio is too high or the setting time

is too long, there is a risk of concrete bleeding. This can cause settlement areas under the reinforcement, which acts as empty voids. If bleeding arises, then bleed water may accumulate in the settlement areas next to the steel-concrete interface (SCI).

Next to the SCI a higher porosity is often naturally present. This is similar to the interfacial transition zone (ITZ), and is caused by a reduced packing density, see Figure 2.11.

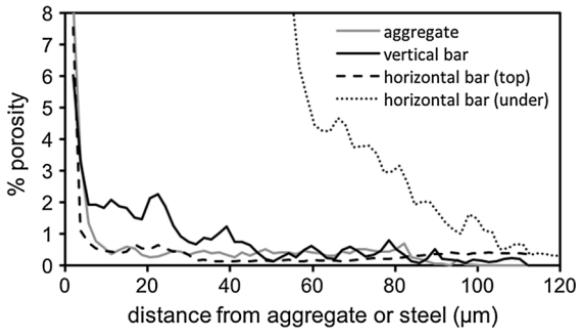

Figure 2.11: Porosity next to the ITZ and SCI [5].

Larger air voids can also arise at the SCI as air bubbles rise during compaction and either adhere to the surface or become trapped underneath horizontal reinforcement [5]. These air voids usually have larger volumes than the pores and will usually fill up with moisture, oxygen and aggressive ions. Even larger voids can also appear inside ducts as the result of poor filling or frost deterioration. If these voids are next to the steel, they can create corrosive environments.

2.2.9 Concrete vs. Grout

Important to note, is that there is a difference between concrete and grout. Concrete is considered a composite material and consist of hydrated cement paste and both coarse and fine aggregates, often with a presence of admixtures [52, 64, 73]. In general, aggregates makes up 70-80% of the volume of concrete and is therefore of great importance to its properties. The variation in aggregate size, or grading, gives concrete an inhomogeneity that causes good packing abilities, and therefore result in small pores with sizes varying from nm - mm, see Figure 2.12. Porosity and pore size are important factors influencing the resistance towards frost attacks, which can cause the concrete to crumble [52]. This is due to the fact that in smaller pores, a lower temperature is required in order for the water inside to freeze.

Grout used for post-tensioning tendon ducts typically consist of a homogeneous mixture of cement, admixtures and water [74, 75]. The main component of grout is ordinary

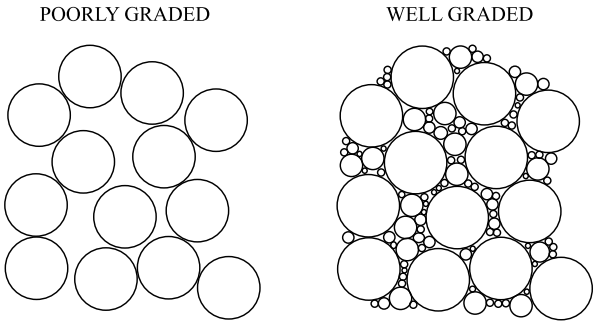

Figure 2.12: A schematic representation of size gradation of aggregates.

Portland cement. An addition of other supplementary cementitious materials can enhance properties such as corrosion resistance and reduce the permeability of the final products [76]. These SCM are typically fly ash, slag cements and dry silica fume, each with its different contribution to the properties. Admixtures are also often used to reduce the w/c-ratio, improve workability and pumping properties.

Even though grout consists of many similar components as concrete, it exhibits different qualities. The lack of large aggregates causes poor grading and therefore causes the mixture to require a higher w/c-ratio to obtain good workability. A higher w/c-ratio results in an increased risk of segregation, which can lead to void formation along the steel-concrete interface. [77, 78]. The poorer grading creates pores in a size range of mm, which can increase diffusion coefficients and give the grout a lower resistance towards frost attacks.

Chapter 3

Herøysundet Bridge

Herøysundet bridge is a girder bridge built in 1966 and located in Herøy in Nordland County. It is a part of FV828 and serves as the main connection between Sør-Herøy and Nord-Herøy. The bridge has a length of 154 meter and consist of one lane with sidewalks on each side, giving its widest point a width of 5.3 meters [79]. Its foundation is made up of 5 piers and 2 abutments, with a largest span of 60m.

During maintenance work in 2019, extensive corrosion on the reinforcement was discovered [80, 81]. These findings have led to limitations regarding use and a plan to build a new bridge is now in motion.

3.1 Components

The bridge has four concrete girders, each being 0.4 m thick and have 4 reinforcement bars running through each side [82], see Figure 3.1. This gives a total of 8 reinforcement bars within the girders.

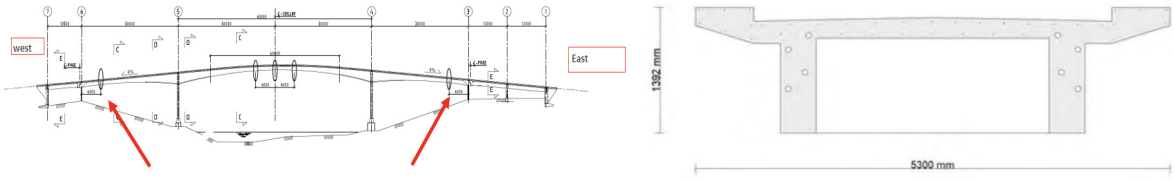

Figure 3.1: A sketch of the bridge and the cross section of a girder [82].

In Herøysundet bridge, the reinfocement used is known as post-tensioned BBRV re-

inforcement bars. These are in the form of bundled tensile wires inserted into tendon ducts filled with grout, see the illustration in Figure 3.2. The BBRV reinforcement allow for both pre-stressing and post-tensioning and are cast into concrete to increase the strength of the structure [83]. Concrete has a tensile strength about 10% of its compressive strength, which can result in cracking when a concrete structure is under load [76]. Introducing stresses to the structure can offset anticipated tensile stresses that can present themselves under loading situations and in turn reduce cracking and increase durability.

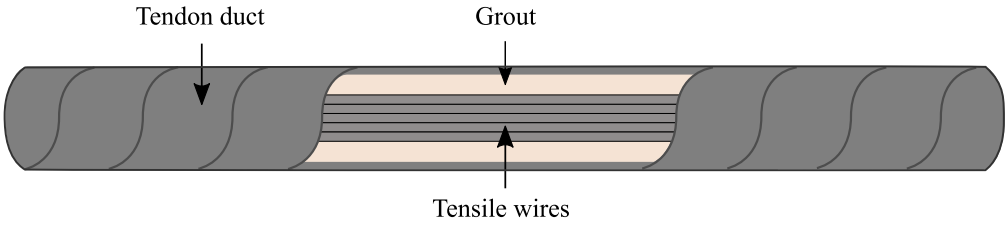

Figure 3.2: An illustration of the reinforcement setup present in Herøysundet bridge.

Tendon Ducts

The tendon ducts are the outer shell of the reinforcement. In the case of Herøysundet bridge, the tendon ducts are made from steel, with a wall thickness of 0.3 mm and an external diameter of 60 mm. They run the length of the bridge and have two joints, each located 15 meters from the center of the bridge [82]. As is the practice with post-tensioned reinforcement, the tendon ducts are cast on site into the structure before the wires are are installed and pulled into tension and the grout is injected [76, 78, 84]. To reflect the parabolic bending moments that gets generated in a simply supported beam structure, the tendon ducts are draped accordingly. An example of a potential placement of a duct is shown in Figure 3.3. These complex layouts allow for very high stressing forces and are able to neutralize external loading by matching the shape of bending moment diagrams.

Tensile Wires

The wires are the innermost component of the reinforcement, and this is where most of the corrosion has taken place in Herøysundet bridge. Each wire has a diameter of 6 mm and is made up of carbon steel without any coating. The chemical composition of the wires is given in Table 3.1.

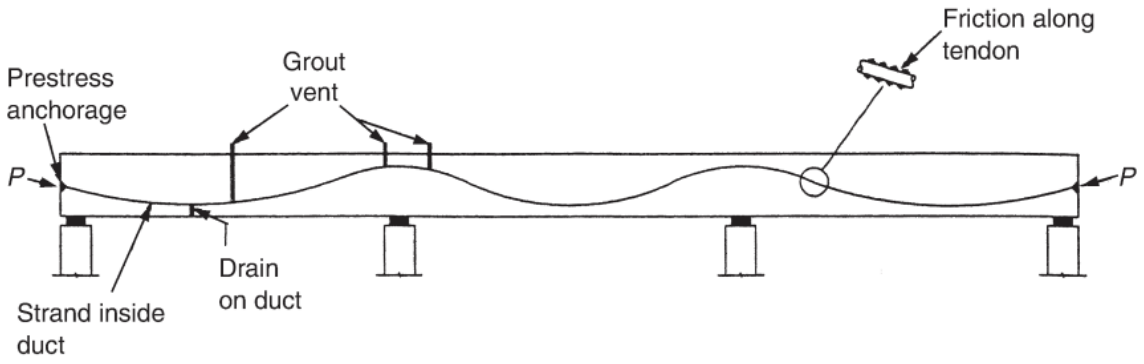

Figure 3.3: An illustration of typical post-tensioned tendon placement [84]

Table 3.1: The chemical composition of the wire given in wt%.

C	Si	Mn	P	S	Cr	Ni	Cu
0.75-0.87	0.15-0.35	0.5-0.8	0.03	0.03	0.10	0.10	0.15

Before being cast into the grout, the wires are prestressed in order to create compressive stresses in the concrete [85]. Hydraulic jacks are used to pull the wires to a predetermined value for the purpose of inducing a force in the wires that makes them elastically elongate [76]. The compressive stresses created will counteract any tensile stresses that can present itself during service loads. After the wires have obtained the full required force from the jack, the force is transferred to the end anchorage, see Figure 3.4. Lastly, the wires are secured by a wedge plate that separate the strands.

On the surface of these tensile wires, a passive oxide layer is formed due to the alkaline environment and high pH level in which the wires are embedded [38]. It has been reported that the smooth surface gained by the process of prestressing the wires creates a firmer passive layer that is harder to break down [7, 35].

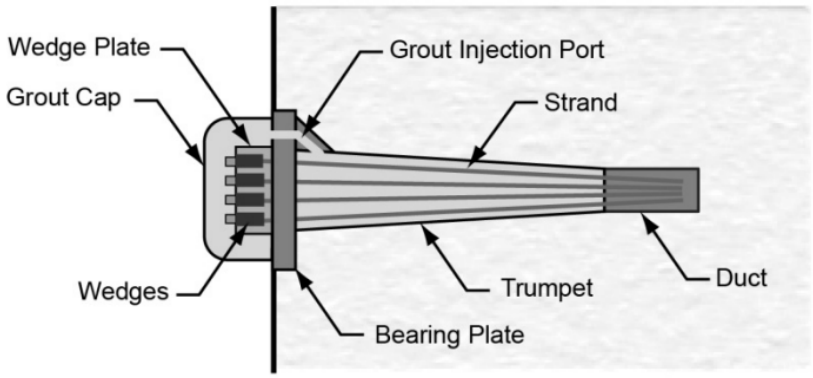

Figure 3.4: A typical post-tensioning anchorage for wire tendonds [76].

Grout

In order to protect the tensile wires and ensure durability to the structure, the duct is filled with grout. The grout is typically pumped into the tendon duct through an injection port after the wires have been pulled and locked into place by the wedge plate [74, 76]. The inlet point is typically a part of the anchorage and is located at the lowest point of the duct layout. As can be seen in Figure 3.3, there are grouting vents placed at the highest points of the layout to ensure complete filling of the duct. After grouting is finished, the anchorage is protected from the environment by being covered with multiple levels of protection.

Traditionally, grout for post-tensioned ducts is made up of cement, water and admixtures [74]. It is important that the grout has flow properties that allows it to flow easily through the ducts in order to properly cover the wires. Incomplete filling of the ducts can result in voids next to the wires, which can serve as locations for initiation of corrosion. The voids can be a result of blockages, entrapped air or leakages in the duct [86]. Given a complete fill of the ducts, the risk of corrosion will be low due to the high alkalinity of the grout [87]. It is also important that the grout is of good quality, which was standardized in the United Kingdom in 1999 according to Table 3.2 [88].

Table 3.2: Select U.K. Grout requirements.

Property	**Common Grout**
Maximum w/c ratio	0.40
Volume change	-1% to $+5\%$
Bleeding	less than 1%
Strength at 7 days	27 MPa (3916 psi)

Figure 3.5 shows a typical example of tendon ducts containing tensile wires embedded in grout. These images are gathered from Farriseidet bridge during its demolition in 2018.

Figure 3.5: Images from Farriseidet bridge [79]. Left: tensile wires in a tendon duct covered in grout. Right: a tendon duct cast into the concrete.

3.2 Inspections Performed on Herøysundet Bridge

Following inspections were performed mainly on three locations. These are illustrated in Figure 3.6

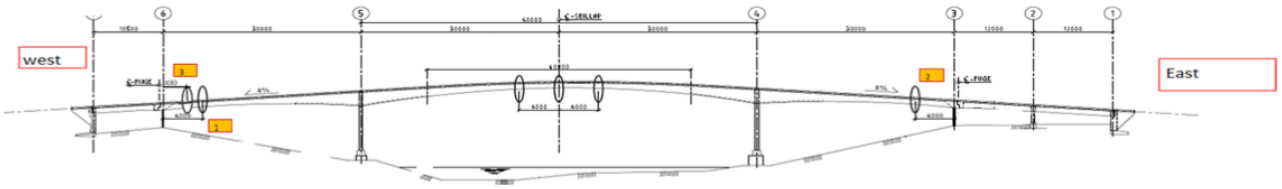

Figure 3.6: An illustration of Herøysundet bridge depicting the areas where samples have been collected [82].

A 2017 inspection lead by Multiconsult on the behalf of SVV was performed in order to determine the chloride content in the concrete of Herøysundet bridge and the corrosion potential of the reinforcement. The results deemed maintenance necessary due to relatively high levels of chlorides in certain areas. High levels of chlorides might prove of big importance to the amount of corrosion found on the reinforcement.

In 2020 Dekra Indrustrial performed an inspection of the bridge using non-destructive testing (NDT) methods in order to locate voids in the grouted tendon ducts [82]. The inspection revealed several areas within the ducts that contained voids of various volumes due to a lack of or crumbled grout. All 8 ducts in the girders were revealed to have areas with missing grout. In the most severe case, there was a 6 meter length missing of grout. In this location it was also discovered three wire breakages. Areas containing voids are typically high-risk areas with regard to reinforcement corrosion.

SVV, in cooperation with NTNU, performed an inspection in 2019 to determine the state of the tendon ducts, grout and tensile wires. The inspection revealed areas where the wires showed signs of general corrosion, some areas with severe pitting damages and other areas completely covered with grout and without sign of corrosion, see Figure 3.7. In one of the tendon ducts, fractured tensile wires were discovered. The state of the tendon ducts varied from unaffected by corrosion on both the inside and outside to highly corroded on both sides. In most cases, the state of the tendon ducts showed corrosion on the internal side, while the outside was without corrosion. With regards to the grout, areas were found with large voids that were completely lacking grout, while in other areas the grout filled the tendon duct completely. There were also areas where the consistency of the grout varied from normal dry to moist and from intact to completely frost deteriorated. Different states of the grout gathered from the bridge is displayed in Figure 3.8. More images from the inspection are given in Appendix E.

Figure 3.7: Tendon duct and tensile wires - Left: missing grout and corrosion on both duct and wires. Right: filled with grout and no sign of corrosion on either component [79].

Figure 3.8: Grout gathered from different locations in the bridge [79].

in 2020, SINTEF was brought in to analyze the grout inside the tendon ducts after the inspection SVV did in 2019 [89]. The grout analysis revealed elements given in Table 3.3. A separate chloride analysis revealed the chloride content in dry grout to be:

- Sample 1: 0.036 %Cl
- Sample 2: 0.026 %Cl

These levels of chlorides are relatively low and it was therefore determined to remove the option of seawater being used as mixing water [89]. Visual inspections and analyzes also revealed a high porosity in the grout and a high w/b-ratio. This led to an assumption of the grout having low viscosity.

Later that year, SINTEF performed an analysis of the grout with regards to moisture content and composition, and analysis of the pore solution [90]. Samples were gathered from two different inspection sites, one sample had dry, firm grout and the other was a moist sample. The results from the moisture analysis are given in Table 3.4.

Table 3.3: The elements found in the grout after analysis by SINTEF [89].

Elements	**Samples**	
	Firm grout [wt%]	Crumbled grout [wt%]
CaO	31.7	23.2
Fe_2O_3	19.6	24.4
SiO_2	10.3	16.5
Al_2O_3	2.71	4.22
MgO	0.86	0.97
Na_2O	0.86	0.90
K_2O	0.436	0.548
TiO_2	0.220	0.233
MnO	0.122	0.114
P_2O_5	0.042	0.051

Table 3.4: Moisture content measured in grout samples by SINTEF [90].

Sample	Moisture content [wt%]	Corrected moisture content (removal of metal and rubber) [wt%]
Dry sample	18	21
Moist sample	39	44

Testing of the pore solution composition from the moist grout sample revealed the major components to be sodium, potassium, sulfur, calcium and chloride [90]. The dry grout consisted mostly of the same elements, though in slightly different amounts, see Table 3.5.

Table 3.5: The composition of the pore solution measured by SINTEF [90].

Element	Moist sample [mmol/L]	Dry sample [mmol/L]
Na	43.406	1.982
K	13.088	1.070
Ca	5.729	15.361
S	8.999	1.138
Cl	0.677	0.536

Note to Table 3.5: Only elements with a concentration above 0.1 mmol/L was included in the table.

A separate chloride analysis was performed on both dry and moist grout samples [90], confirming the measurements previously performed by SINTEF [89]. The following

chloride contents were measured:

- Moist sample: 0.037 %Cl
- Dry sample: 0.035 %Cl

Lastly, the pH of the pore solution was measured to 13, using pH paper strips [90].

3.2.1 A Summary from the Inspections

The following main findings can be summarized from the inspections:

- Metal components:
  1. Corrosion was present on the tensile wires in areas with incomplete filling of the grout and in areas where the grout did not follow requirements.
  2. The corrosion found on the wires was either general corrosion or pitting corrosion. A general trend was that the corrosion was worse on the wires close to the bottom of the duct compared to the ones on top.
  3. On one of the locations a wire was found fractured, most likely a result of corrosion.
  4. The state of the ducts varied, but in most cases, the inside was highly corroded while the outside was untouched by corrosion.
- Grout:
  1. The state of the grout varied from dry to moist and from intact to frost deteriorated.
  2. The degree of filling varied a lot and in some areas there were large voids observed.
  3. The composition of the grout varied throughout the bridge, but main components were found to be Na, K, Ca, S and Cl.
  4. Chloride contents in both grout and pore solution was relatively low.
  5. Low probability of carbonation.
  6. High moisture contents. Cause to assume segregation.

Chapter 4

Previous Research

In the 1980s, corrosion in post-tensioned tendons became a concern regarding the durability of structures on an international level [91]. Since then, there have been a lot of research devoted to discovering the cause of corrosion of steel in concrete. Worth noting is that a lot of research performed is based on corrosion of steel in concrete and not in grouted tendons.

4.1 Composition of Concrete Pore Solution

In 1983, Page and Vennesland tested ordinary Portland cement and silica in order to determine the composition of the pore solution [72]. To determine the major ionic constituents, standard procedures such as titration, graviometric determination and atomic absorption spectrometry was carried out. The results of the procedures showed that the pore solutions consisted primarily of Na^+, K^+ and OH^-, while Ca^{2+} and SO_4^{2-} were only minor specimens. Later research on the composition of cement pore solutions have concluded in similar compositions [5, 92, 93]. These findings have been used in order to create simulated pore solution for further corrosion research.

4.2 Forming an Oxide Layer on the Surface

A lot of research base itself on directly exposing steel samples to chlorides or sulfates. This does not give the steel the time to passivate, as it does when embedded in concrete. Therefore, research have been performed to achieve an estimate of the time it takes to

passivate the steel in synthetic pore solutions and in mortar [94]. The composition of the synthetic pore solution used by Pursaee et al. is given in Table 4.1. This study used steel samples with different surface conditions, i.e as-received and sandblasted.

Table 4.1: Composition of synthetic pore solution in the research by Poursaee et al. [94].

NaOH (g)	KOH (g)	$CaSO_4 \cdot 2H_2O$ (g)	$Ca(OH)_2$ (g)	Water (L)
9.17	31.4	0.96	4.2	1.75

In order to determine the required time for passivation, Poursaee et al. [94] deployed potentiostatic linear polarization resistance (LPR) and half-cell potential techniques. The research concluded that it takes approximately three days for the steel to develop a passive layer with potentials of approximately - 200 mV vs. SCE, but the potential continued to slowly increase after that. This led to a recommendation that steel should be kept in the solution for at least a week prior to adding chlorides.

In a study by Chen et al., they looked at the corrosion behavior of ASTM A416 steel in simulated pore solutions under active aeration [95]. The alkaline solution used to simulate the environmental conditions within cement grout is given in Table 4.2. After the solution was mixed, the suspended $Ca(OH)_2$ solids was filtered out of the electrolyte. The working electrode (the ASTM A416 steel rod) was polished with silicon carbide papers up to 600 grit. The reference electrode equipped was a Hg/HgO electrode and the counter electrode was made of platinum.

Table 4.2: Composition of the solution used in the research by Chen et al. [95].

$Ca(OH)_2$ (g/L)	NaOH (g/L)	KOH (g/L)	pH
2	8.33	23.3	13.8

Measurements, performed using a potentiostat, suggested the formation of an oxide film on the surface of the steel [95]. This film thickness increased with increasing immersion time. Through open circuit potential (OCP) measurements it was discovered that it could require up to 300 ks ($\sim$ 3.47 days) for the system to reach a steady state at a potential of approximately - 80 mV vs. Hg/HgO, see Figure 4.1a. Though, the oxide started stabilizing already after $\sim$100 ks. They also discovered that by applying different potentials during the OCP measurements, the time until stabilization differed, see Figure 4.1b. At a potential of +0.22 V vs. Hg/HgO it took 250 ks to reach a steady state, while at other potentials it could suffice with 50 ks for the system to reach a steady state current, see Figure 4.1. Lastly, cyclic voltammetry revealed possible corrosion products to be FeO, $Fe(OH)_2$ and Fe_3O_4.

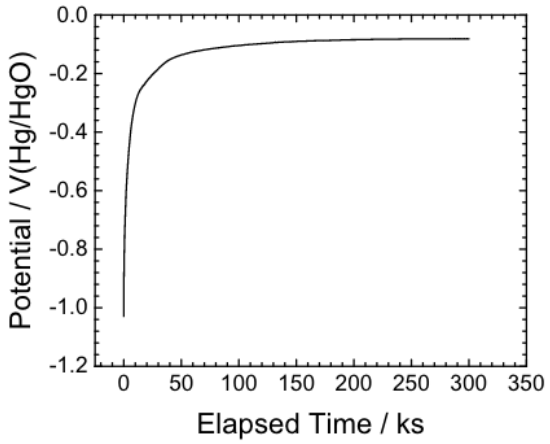

(a) OCP as a function of time.

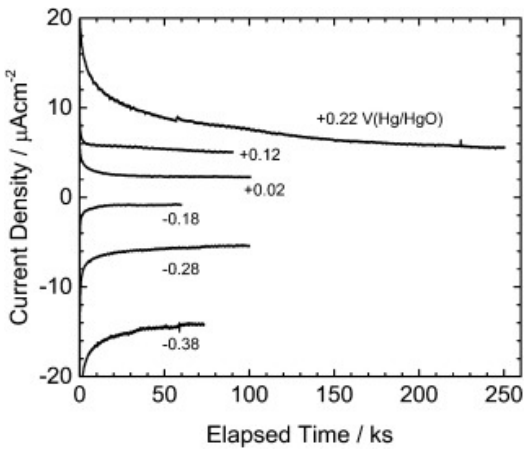

(b) Current density as a function of time, with varying applied potentials.

Figure 4.1: Results from a study by Chen et al. [95].

Other studies have also been performed on the time it takes for the OCP of steel to reach a steady state in alkaline solutions. Sánchez et al. ran tests on steel rebars submerged in simulated concrete pore solutions, created with saturated $Ca(OH)_2$ [19]. They discovered that a natural growth of the passive layer on the steel surface starts reaching a stable state after 3 days and is stable at -0.27 V vs. SCE after 5 days. This corresponds to the three days until reached passivity at -0.2 V vs. SCE discovered by Pourasee et al. [94] and at -80 mV vs. Hg/HgO (∼-0.22 V vs. SCE) discovered by Chen et al. [95]. Researchers have noted steady state behavior after shorter periods of time, such as Abd El Haleem et al. [96], who reported signs of a steady OCP already after 250 minutes. However, other researchers, such as Flis et al. [97], noted that the OCP started to shift towards the active direction after 30 days and was still changing after 100 days. Minor differences in the composition of the electrolytes and small variations in pH, could amount to some of the differences in results.

Research was performed by Ghods et al. to study the properties of the passive oxide film that forms on the surface of steel when exposed to a saturated calcium hydroxide solution, and how chlorides affects the film [18]. Sample preparation consisted of creating rebar specimens with a length of 8 mm each. These were polished with anhydrous isopropyl alcohol to prevent oxidation. Three samples were then immersed in a saturated calcium hydroxide solution meant to simulate a concrete pore solution. The solution had a pH of 12.5, a conductivity of 8.82 mS/cm and a dissolved oxygen concentration of 2.28 mg/L. It was prepared by dissolving analytical grade calcium hydroxide in distilled water. Two samples were removed after 2 and 9 days, respectively, in order to study

the effect of immersion time on the properties of the passive film. After 9 days, sodium chloride was added to the solution to increase the chloride concentration to 0.05 M.

By using X-ray photoelectron spectroscopy on the samples, it was found that the oxide films formed were approximately 4 nm thick and were not affected by the immersion time in the solution [18]. Analysis revealed that the oxide film consisted of Fe^{2+} rich oxides close to the substrate and Fe^{3+} oxides near the free surface. The amount of Fe^{2+} compared to Fe^{3+} increased with increasing immersion time. The addition of chlorides resulted in a reduction of the oxide film, which supports the theory that the interaction with chlorides causes the oxide to dissolve into the solution.

In a later study by Ghods et al., the passivity and chloride-induced depassivation of steel immersed in simulated concrete pore solutions were studied again [98]. Samples were prepared in the same fashion as the previous research by Ghods et al. [18]. The solution used for passivation of the steel samples is given in Table 4.3. Three samples were immersed in the solution and kept there for two weeks. Passivation of the samples was confirmed by OCP measurements, which after passivation was relatively constant at -220 ± 10 mV vs. SCE.

Table 4.3: Composition of the solution used in the research by Ghods et al. [98].

$Ca(OH)_2$ (M)	NaOH (M)	KOH (M)	$CaSO_4$ (M)	pH
0.1	0.1	0.2	0.003	13.3

After two weeks of exposure, a sample was removed before sodium chloride was added to the solution [98]. This brought the chloride concentration in the solution to 0.45 M, which Ghods et al. discovered to be below the depassivation threshold of polished steel samples in concrete pore solutions during a previous research [36]. The OCP measurements continued to show stable behavior at values of approximately $-230 \pm$ 10mV vs. SCE. After two more weeks of exposure, a second sample was removed and the chloride concentration in the solution was increased to 3 M. The sample was kept in the solution for four weeks in order for the chlorides to have time to react with the passive film. The OCP measurements of the third sample showed stable behavior with values measured to -350 ± 10mV vs. SCE.

Once the last sample was removed, X-ray photoelectron spectroscopy was performed to analyze the results [98]. The oxide film formed on the samples was determined to be approximately 5 nm thick and consisting of Fe^{2+} close to the substrate and Fe^{3+} near the free surface, which is similar to the results of the previous study [18]. The addition of chlorides resulted in a thinner oxide layer with a reduction of the Fe^{2+}/Fe^{3+} ratio.

Fe^{2+} oxides were determined to be the protective oxides, as a decrease in Fe^{2+} with respect to Fe^{3+} caused depassivation of the steel.

4.3 Corrosion Testing

Sulfate Concentration

After severe corrosion related to grout segregation was discovered on bridges in Florida related to grout segregation, research began to determine the cause [1]. The grout was discovered to have high pore water pH, moisture content and sulfate concentration, but a low chloride content. For the experimental part of the study, steel samples were exposed to alkaline solutions meant to simulate pore solutions with pH of 12.6 and 13.3, and with varying sodium sulfate levels, see Table 4.4. In the experiment, some of the samples were exposed to early fixed sulfates, while other were exposed to sulfates later on. This was to determine the impact of allowing an oxide layer to form on the surface of the steel.

Table 4.4: Compositions of the solutions used for electrochemical tests in the research by Krishna Vigneshwaran et al. [1].

Solution	NaOH (g/L)	KOH (g/L)	$Ca(OH)_2$ (g/L)	pH
1	-	-	2.1	12.6
2	3.7	10.5	2.1	13.6

Electrochemical testing performed in the research by Krishna Vigneshwaran et al. [1] included steady-state condition tests measuring E_{corr} and linear polarization resistance (LPR). In addition, potentiodynamic polarization tests were run. The research found that pH was a really important parameter in the corrosion development. In highly alkaline solutions, with pH above 13, the sulfates were not able to break down the passive film. There were, however, corrosion on some of the samples in more moderately alkaline solution with a pH around 12.6. In the cases where early fixed sulfates were present, there was damage on the passive layer which resulted in pitting corrosion. When the sulfates were added in later, they were not able to depassivate the steel, even at the lower levels of pH, see Figure 4.2.

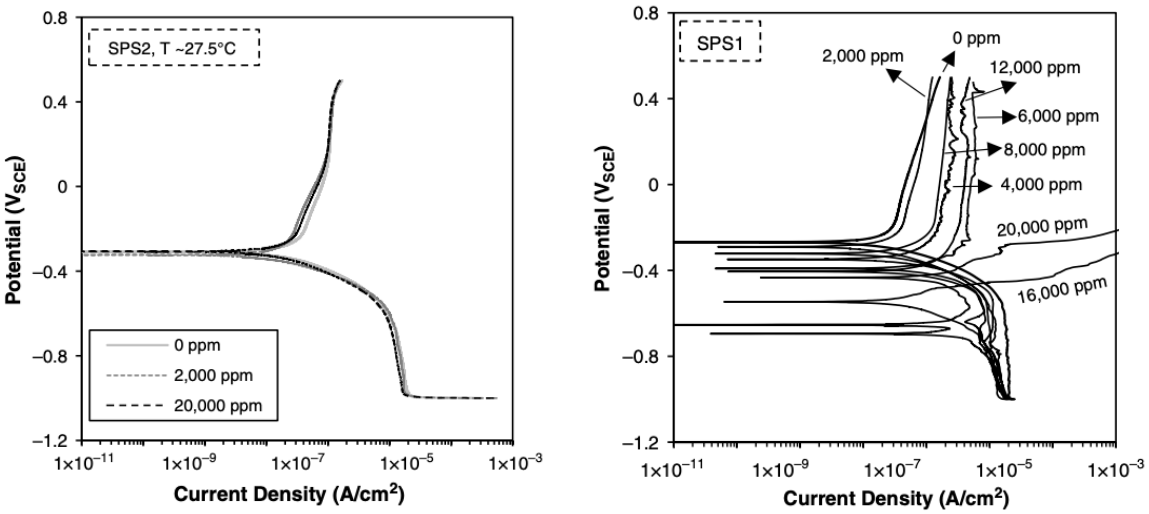

(a) pH = 13.3 **(b)** pH = 12.5

Figure 4.2: Anodic polarization curves with late exposure of varying contents of sulfate ions measured by Krishna Vigneshwaran et al. [1].

Krishna Vigneshwaran et al. are only some of many who have devoted research on the subject of how sulfate concentrations affect the corrosion rate of steel in concrete. The general conclusion is that increasing the sulfate concentration increases the corrosion. In 1988, Al-Tayyib et al. [99] tested steel samples polished to 600 grit in a saturated $Ca(OH)_2$ solution with a pH of 12.5 and varying concentrations of Na_2SO_4. They discovered that sulfate ions actively participate in corrosion and noted an increase in corrosion rate when sulfates were combined with increasing temperatures. Dehwah et al. [57] tested in 2002 steel reinforcement samples in different types of Portland cements with an addition of NaCl and varying contents of Na_2SO_4 and $MgSO_4$. They found that the addition of sulfates did not affect the time to initiation of corrosion, but increased the current density compared to solutions only containing chlorides. It was also discovered that the magnesium sulfate caused bigger increases in i_{corr} compared to sodium sulfate.

How the different types of sulfate salts influence the passive film on steel in simulated concrete solution was the topic of the research performed by Xu et al. in 2019 [2]. In their research they used carbon steel rods with a diameter of 10 mm and a length of 10 mm as test material. The samples were grinded with emery paper up to 1200 grit, rinsed and degreased with acetone before being covered with epoxy resin to give an exposure area of 0.785 cm^2. The base solution was made of saturated $Ca(OH)_2$ to simulate a concrete pore solution. For the purpose of creating a passive layer on the surface, the samples

were kept in the simulated pore solution for 7 days prior to testing. The samples were then immersed in separate containers containing the solution and four different types of sulfate salts, respectively. The salts in question were magnesium sulfate ($MgSO_4$), ammonium sulfate ($(NH_4)_2SO_4$), sodium sulfate (Na_2SO_4) and calcium sulfate ($CaSO_4$). There was also created a solution with sodium chloride (NaCl) for reference. The salts were replenished stepwise each day at a dosage of 0.01 mol/L. For the experiments, a SCE was used as working electrode and a platinum electrode as reference electrode. Cyclic polarization (CP) was measured from 200 mV below E_{corr} up to 1200 mV vs. E_{corr} and then reversed, with a scan rate of 1 mV/s. All tests were run at room temperature. Results are displayed in Figure 4.3.

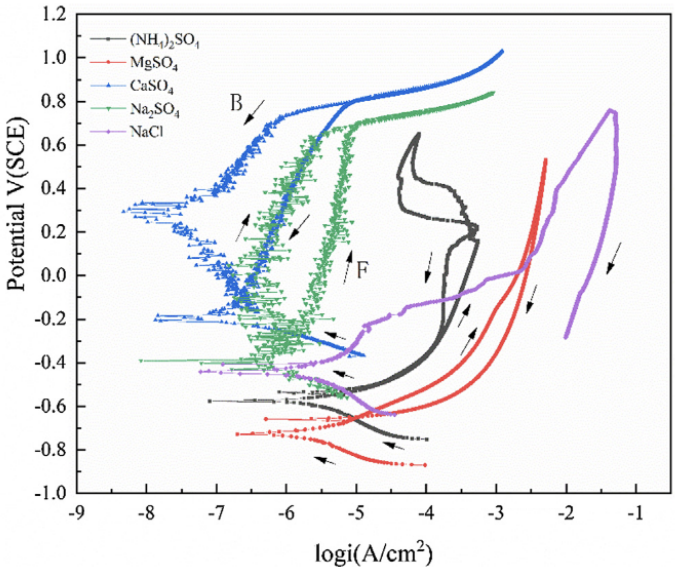

Figure 4.3: Cyclic polarization curves measured by Xu et al. for different salts [2].

From experimental testing, Xu et al. [2] discovered that the magnesium sulfate and ammonium sulfate induced higher corrosion rates than sodium chloride and sodium sulfate. This observation was based on the measurements of i_{corr}. From the current density measurements, they concluded that calcium sulfate had an almost negligible corrosion effect on the passive layer, compared to the other sulfate salts and the sodium chloride. They also discovered that the chloride ions were more prone to induce pitting corrosion compared to the sulfates.

Chloride concentration

In a 2011 report by R.D. Moser et al., the topic of chloride induced corrosion of prestressed steel was researched [3]. Cold drawn specimens in the shape of both single wires and 7-wire strands were used as testing material. The prestressed steel was coated with $ZnPO_4$, which prior to testing was determined to be flawed as a result of cold drawing. The wire samples were coated with a silicon adhesive sealant at the top and bottom of the exposure area to prevent crevice corrosion. This left an exposure area of 3.5 cm^2. All experiments were performed in a solution simulating the composition of a typical concrete pore solution, see Table 4.5. Prior to testing, all samples were immersed in the simulated pore solution without the presence of chlorides for 90 minutes, in order for a passive layer to form on the surface. The samples were then directly transferred to a solution containing chlorides and left for 30 minutes to acclimate before testing began.

Table 4.5: Composition of simulated concrete pore solution used in research by Moser et al. [3].

KOH (g/L)	NaOH (g/L)	$CaSO_4 \cdot 2H_2O$ (g/L)	$Ca(OH)_2$ (g/L)	pH
17.94	5.24	0.55	2.40	13.6

Cyclic potentiodynamic polarization techniques were used to measure the corrosion resistance of the samples when exposed to different concentrations of chlorides [3]. Tests began at -25 mV vs. OCP and ran with a scan rate of 0.1 mV/s until it reached a current density of 0.25 mA/cm^2. In Figure 4.4, only chloride concentrations that resulted in corrosion initiation were included.

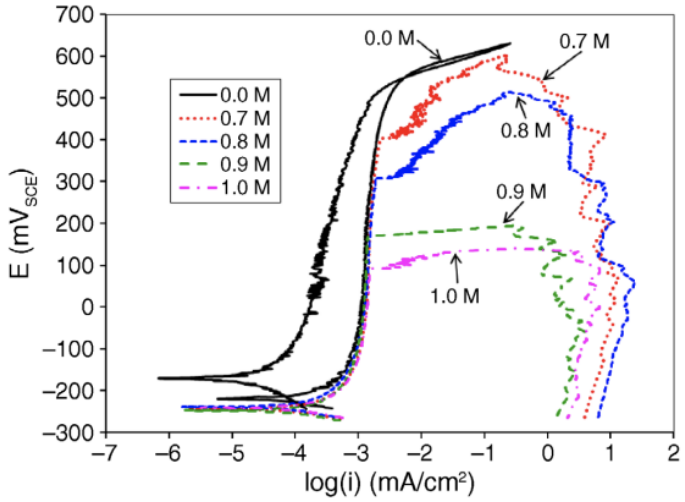

Figure 4.4: Polarization curves for different levels of Cl^- for the pre-stressed wires measured by Moser et al. [3].

As can be seen in Figure 4.4, Moser et al. [3] found that an increase in chloride content leads to a decrease in the pitting potential, E_{pit}, and a slight decrease in the E_{corr}. The corrosion was initiated as localized pitting attacks, primarily at imperfections on the surface. The pitting corrosion was then followed by uniform attacks on the surface of the samples.

Li et al. tested the chloride corrosion threshold of reinforcing steel in alkaline solutions [6]. Test material was made using samples made from reinforcement steel bars with a diameter of 12 mm. The samples were then divided into three groups: 1) as-received condition, including some rust; 2) sandblasted; 3) immersed in sodium chloride to create a pre-rusted condition. Three different solutions were created according to Table 4.6. The pH of the solutions dropped up to a order of ∼3 as the chlorides were added to the solutions.

Table 4.6: The solutions created for the experimental testing in the research by Li et al. [6].

Solution	NaOH (g/L)	KOH (g/L)	$Ca(OH)_2$ (g/L)	pH
1	0	0	2	12.6
2	3.70	10.5	2	13.3
3	8.33	23.3	2	13.6

Through OCP measurements, electrochemical impendance spectroscopy (EIS) and polarization resistance, R_p, measurements, Li et al. [6] discovered that the chloride threshold level was not constant but varied with pH. As can be seen in Figure 4.5, the increase in pH level demanded higher chloride concentrations in order to initiate corrosion. In the solution with a pH of 13.6, active corrosion was started in the sandblasted samples, but not sustained as the chloride content reached 3.0M. This can be seen in Figure 4.5c from the fluctuations of the corrosion potential, denoted E_{OC} in Figure 4.5, between -400 mV, indicating active corrosion, and -200 mV, which indicates passivity.

Ioan Pepenar performed a study in 2017 regarding the influence of chloride ions on the electrochemical behavior of prestressing steel in alkaline solutions [100]. The materials tested were two types of high strength steel, typically used as tendons for prestressed concrete structures. The samples were covered in epoxy resin to leave a sample area of 20 mm^2 and 40 mm^2 for steel type 1 and 2, respectively. The samples were then grinded with emery paper up to 1000 grit and degreased with benzene and washed with acetone. No passive layer was ensured prior to testing. The electrolyte used was made up of an aqueous suspension of Portland cement with a pH of 12.7 and a w/c ratio of

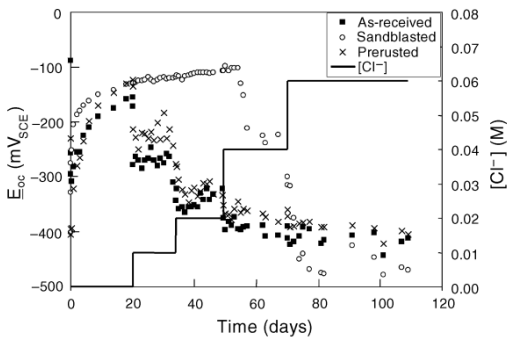

(a) pH = 12.6

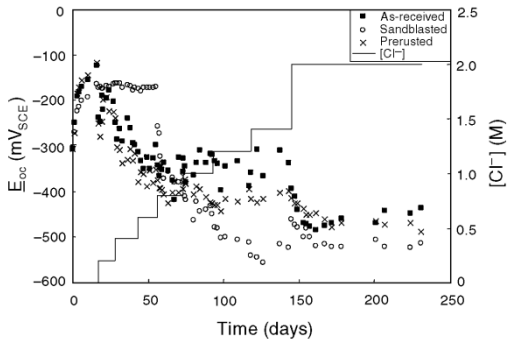

(b) pH = 13.3

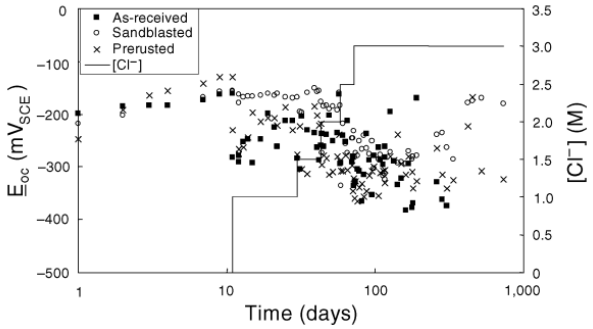

(c) pH = 13.6

Figure 4.5: The results from Li et al. showing the evolution of corrosion potential as the chloride content increase over time [6].

10. Different concentrations of chlorides were added to the solutions for electrochemical testing.

Anodic potentiodynamic polarization curves were measured from a potential of -1000 mV vs. SCE with a scan rate of 0.556 mV/s [100]. The scan was reversed once the oxygen release potential was reached. Measurements led to the conclusion that depassivation of the steel started occurring once the chloride concentration exceeded 0.01 M. Further increasing the chloride concentration caused a shift in the electrode potentials in a more negative direction. Lastly, it was found that the pitting potential decreased linearly with the logarithmic value of the chloride concentration.

In 2014, Lee and Zielske wrote a report on the behalf of the Federal Highway Administration on the subject of chloride threshold levels in post-tensioning tendon grout [4]. They ran tests on single-wire specimens, single-strand specimens and multi-strand specimens. The single-wire specimens were electrochemically tested in aqueous solutions with different pH and chloride concentrations, while the single- and multi-strand specimens were tested in grout. The solutions used for testing of the single-wire specimen is

given in Table 4.7, in addition the chloride concentration by weight of cement was varied between 0.00 and 5.00 percent. The single-wire tests had the intention of evaluating the effects that chloride concentration, pH and stress levels have on corrosion.

Table 4.7: The chemical composition of the test solutions used in the research by Lee and Zielske [4].

pH	Na_2CO_3 (g/L)	$NaHCO_3$ (g/L)	$Ca(OH)_2$ (g/L)	NaOH (g/L)	KOH (g/L)
9.0	4.10	24.41	0	0	0
13.6	0	0	1.96	8.11	22.76

The experimental test setup used a Ag/AgCl electrode as a reference electrode [4]. Tests were run both with wires subjected to no external stresses and on wires prestressed to 60% of the guaranteed ultimate tensile strength. The results of the corrosion potential data is given in Figure 4.6.

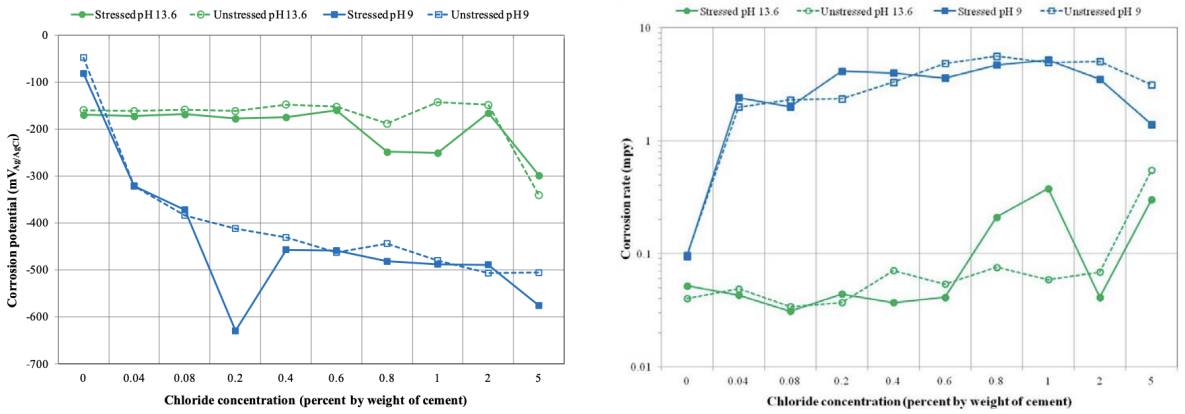

(a) Corrosion potential **(b)** Corrosion rate

Figure 4.6: Results from tests for single wire specimen under different test environments measured by Lee and Zielske [4].

From the results of Lee and Zielske [4], it was clear that, at a pH of 13.6, the wires were protected by the passive film that gets created at high pH levels. This is indicated by relatively high potentials and low corrosion rates. The potential was stable, and the wires withstood any significant corrosion with chloride concentrations up to 0.6%. The lower pH tests yielded results with lower corrosion potential and higher corrosion rates compared to the equivalent tests run at pH 13.6, as is displayed in Figure 4.6. The increase in chloride concentration resulted in lowering the corrosion potential for the solutions with a pH of 9.0. At the same pH level, there was a drastic increase in corrosion rate measured between the chloride free solution and the solution with a chloride concentration of 0.04 wt%, indicating very low resistance towards corrosion already at very low chloride concentrations.

Lee and Zielske [4] noted a reduction in corrosion rate at a 5% chloride concentration, which could be caused by a reduction in dissolved oxygen due to the amount of chloride ions. They also noted a significant difference in corrosion product between pH 9.0 and 13.6. At the higher pH level, corrosion products observed were negligible, while for pH 9.0, the corrosion products were more visible and as the corrosion rate increased, the color of the solution darkened from dissolved corrosion products.

Galvanic Couplings

Dong and Poursaee performed a study on the subject of coupled reinforcing steel in simulated concrete pore solutions in 2019 [62]. Test material consisted of ribbed steel bars that were sandblasted and cleaned, then coated with an epoxy resin in order to isolate specified surface areas. The samples were divided between active and passive steels, where the passive samples had a constant exposure area, while the active samples were given three different exposure areas. This resulted in three different active-to-passive area ratios, see Figure 4.7a. The chemical composition of the simulated concrete pore solution is given in Table 4.8.

Table 4.8: Composition of the solution used for testing in the research by Dong and Poursaee [62].

NaOH (Mol/L)	KOH (Mol/L)	$Ca(OH)_2$ (Mol/L)	$CaSO_4 \cdot H_2O$ (Mol/L)	pH
0.1	0.3	0.03	0.002	13.1

All samples were immersed in the chloride-free solution for 14 days prior to testing [62]. Then, an addition of 3wt% of NaCl was given to the active cells. After 90 days, the chloride concentration in the active cells were increased to 10wt%. For testing of coupled cells, a salt bridge was used in order to keep the passive cell from being contaminated by the chlorides in the active cell. The salt bridge was filled with 1 mol/L KOH which was sealed in by two sintered discs at the ends of the U-shaped glass tube. The setup, illustrated in Figure 4.7b, was sealed in order to minimize effects of carbonation and to prevent evaporation.

Measurements performed included LPR, CP, EIS and zero resistance ammetry (ZRA) [62]. A SCE served as the reference electrode and a 316L stainless steel rod as the counter electrode. All experiments were performed at room temperature ($\sim$23°C). LPR tests were performed within the range of $\pm$ 10 mV vs. corrosion potential, E_{corr}, with a scan rate of 0.166 mV/s. CP tests were run from -200 mV vs. E_{corr} to +500 mV vs. SCE and decreased to -200 mV vs. E_{corr}, with a scan rate of 0.166 mV/s. From the measurements, it was discovered that the area-ratio between the passive and active

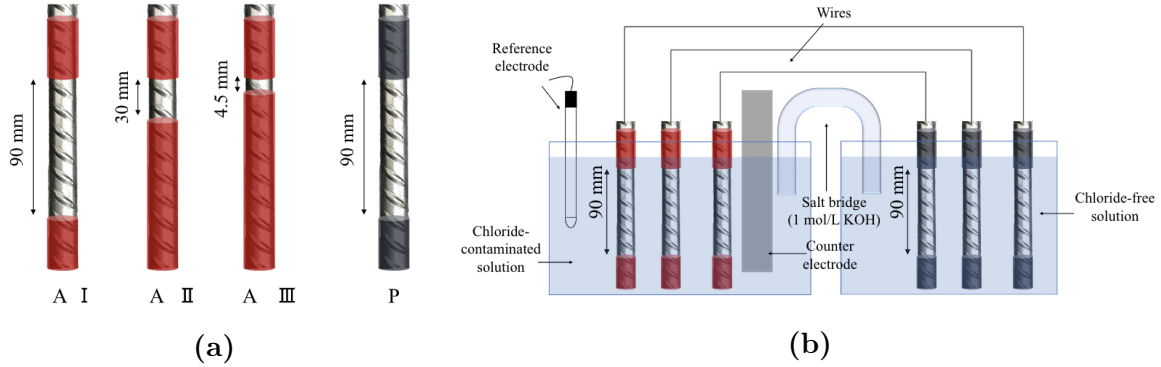

Figure 4.7: An illustration of the sample designs and setup for coupled cells used by Dong and Poursaee [62].

areas played a part. In the experiments where the active area was smaller than the passive area, the galvanic coupling did not seem to affect the potential development of the active steel. However, in the experiments with a 1:1 ratio, the galvanic coupling caused an increase in potential of the active steel, see Figure 4.8. CP tests revealed that coupled samples with an active area smaller than a passive area displayed very small hysteresis loops compared to individual samples. This could indicate a tendency towards more severe general corrosion instead of the localized attacks presenting itself on individual samples.

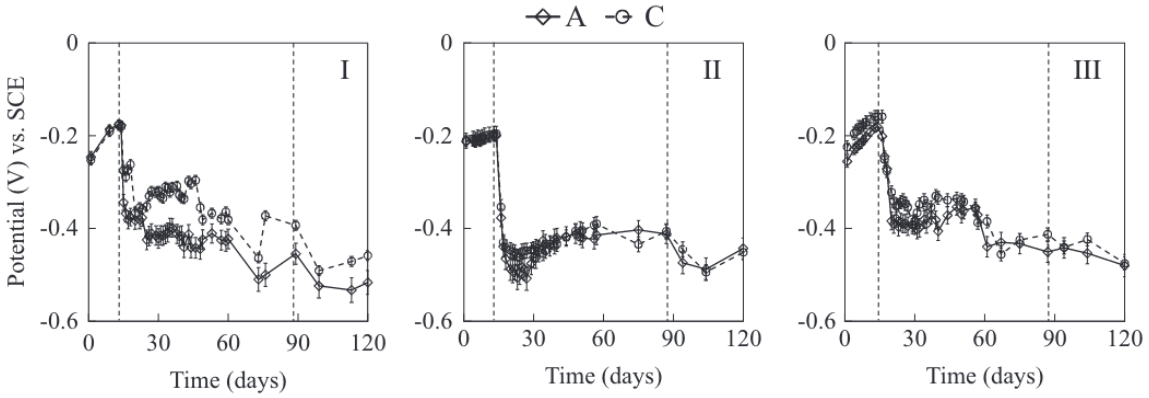

Figure 4.8: The potential development for different passive/active areas following the research of Dong and Poursaee [62]. The numbering in the top right corner correspond to the sample geometry displayed in Figure 4.7a.

The research concludes that couplings with an A/P-ratio less than 1:1 resulted in little potential changes [62]. This being mentioned, galvanic couplings increased the anodic and cathodic Tafel slopes compared to individual samples. An increase in iron oxidation rates resulted in heightened corrosion rates.

Castel et al. performed several studies on the effect of galvanic couplings of steel reinforcement in carbonated concrete [61, 101]. Test samples were prepared by casting 10 horizontal steel samples into a 1100 mm high concrete member. The steel samples were made of two 12 mm diameter ribbed steel bars with an electric wire welded onto an end, glued together with PVC tubes. After a curing period of 28 days in water, the concrete member was sawed into ten pieces, each containing one PVC-steel bar. Due to the top-bar effect, the samples cast on the top section of the member displayed steel-concrete interfacial defaults. The ten pieces were then sawed in two across the center PVC section. An epoxy resin was used to coat the concrete samples, as shown in Figure 4.9, in order to control the area susceptible to carbonation. In these studies, the carbonation process was accelerated by placing the samples in a confined room with an optimal relative humidity (∼65%) and with 50% CO_2 and 50% air. The samples were left for 16 weeks in these conditions. Passive specimens were created by being cast into smaller members and using steel bars with a length of 100 mm.

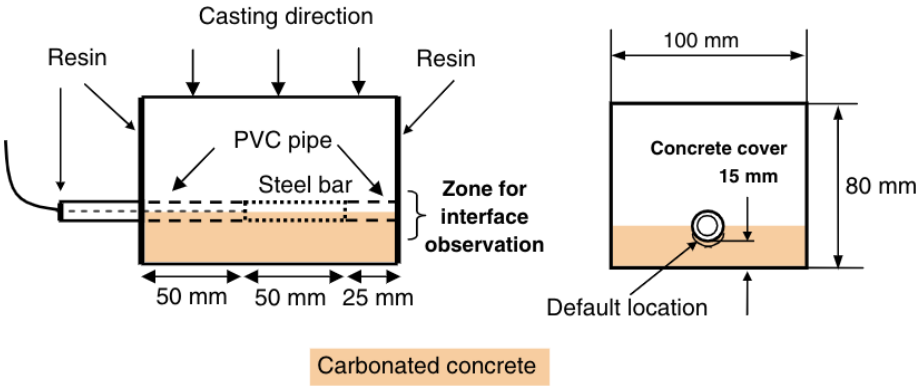

Figure 4.9: Specimens used in the research by Castel et al. after sawing and coating was performed [61, 101].

The experimental setup used is displayed in Figure 4.10, and shows that the macrocells consisted of an active and a passive sample that was electrically connected and partially submerged in water. During the 2010 research [101], the macrocell current was measured regularly during a 6 to 17 week immersion time using zero resistance ammetry (ZRA). Results showed that samples containing interfacial defaults displayed significantly lower potentials on the depassivated sample, compared to samples without defaults. The 2014 report also included microcell corrosion testing in order to compare microcell and macrocell currents [61]. Through testing they concluded that galvanic current densities were of great importance and much higher than the measured microcell current density. In addition, they noted that the active-passive ratio strongly influenced the macrocells, as the galvanic current density increase with increasing surface ratios.

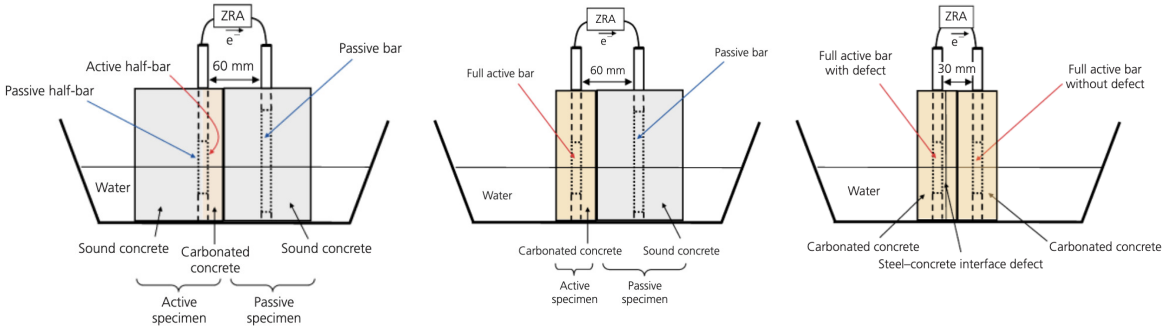

Figure 4.10: Setups used to monitor macrocell corrosion in the research by Castel et al.. Setup a) is the one used in the 2010 report [101], while all three are equipped in the 2014 report [61].

4.4 Previous Research on Herøysundet Bridge

After severe corrosion was detected on Herøysundet bridge, research began in order to determine the cause [50]. Corrosion testing was performed on materials from Farriseidet bridge, which was built at the same time as Herøysundet bridge, had the same type of tensile wiring and presented similar corrosion attacks. The wires used for testing was not cleaned in any way, and therefore had minor traces of grout present on the surface, as well as the natural oxide layer which had been created during its service lifetime.

Testing consisted of ASTM G61 and OCP/LPR measurements. Results from the testing are displayed in Figure 4.11

Test	Electrolyte composition				G61					OCP/LPR development			
No.	pH	Cl^- (g/l)	SO_4^{2-} (g/l)	Oxygen?	Ecorr	Epit	Erep	Ipass1	Ipass2	OCP-start	OCP-finish	icorr-start	icorr-finish
1	12	3,545		Yes	-313	620	-475	6,9	2220	-230	-620	0,117	2,185
2	12	3,545		No	-46	575	NA	0,27	0,056				
3	12	14,18		Yes	-352	-94	-511	6,8	1430				
4	12,5	3,545		Yes	-350	100	-480	5	1170	-300	-390	0,753	0,708
5	12,5	3,545		No	-455	> 200	NA	2,28	0,9	-500	-500	0,132	0,151
6	12,5	14,18		Yes	-360	-70	-500	1,91	1480				
7	12,5	14,18		No	-400	> 200	NA	1,4	1				
8	12,5	35,4		Yes	-410	-25	-440	3,7	45				
9	12,5	35,4		No	-506	-230	-580	1,59	475				
10	13	3,545		Yes	-320	520	NA	0,86	0,3	-150	-506	0,0248	1,201
11	13	14,18		Yes	-240	140	-600	0,11	120				
12	12		20	Yes	-310	600	NA	1,54	0,16	-145	-560	0,074	1,490
13	12,5		20	Yes	-175	600	NA	2,95	NA				
14	12	3,545	20	Yes	-270	500	NA	0,6	0,5	-260	-590	0,142	1,223
15	12,5	3,545	20	Yes	-220	600	NA	1,33	NA	-140	-564	0,120	2,660
16	14,5	3,545		No	-880	-350	NA	12,4	4,2	-160	-565	0,120	2,664
					$mV_{Ag/AgCl}$	$mV_{Ag/AgCl}$	$mV_{Ag/AgCl}$	µA	µA	$mV_{Ag/AgCl}$	$mV_{Ag/AgCl}$	$µA/cm^2$	$µA/cm^2$

Figure 4.11: A summary of the results found in the report by Roy Johnsen [50].

The results concluded that for solutions with pH levels of 12 and 12.5, with a chloride concentration of either 3.545 or 14.18 g/L, the removal of oxygen from the solutions decreased the corrosivity. This was indicated by increased values of E_{pit}, less clear E_{rep}

and decreased anodic current during the decrease in potential. The results also showed that for pH levels of 13, an increase in the chloride content from 3.545 g/L to 14.18 g/L caused increased corrosion by lowering E_{pit} and increasing the anodic current during the decrease in potential. It was also found that the presence of sulfates reduced the corrosivity of the electrolyte. This was indicated by either no or a reduction in the hysteresis loop after reaching maximum potential, noted by Ipass1 $\leq$ Ipass2 or NA in the table in Figure 4.11. It was also found that at pH levels of 14.5 the OCP was more negative than for lower levels of pH. In addition to this, the polarization curve showed unstable current values between -900 to -600 mV vs. Ag/AgCl, which could indicate that the oxide layer is unstable between these potentials.

Chapter 5

Method

5.1 Outline of Tests

In the experimental work, carbon steel samples will be cut from tensile wires into a length of ∼80 mm before being grinded with emery paper. Sections of the samples will then be coated to expose a predefined surface area to the electrolyte. In order to create a passive layer on the exposed surface, the samples will be exposed to a simulated concrete pore solution with a pH of 13.5 for a duration of a week.

All experiments will be performed in saturated $Ca(OH)_2$ solutions with varying pH levels and ion contents. The experimental work will include measurements of potentiodynamic cyclic polarization (CP) curves according to ASTM G61 and long-term exposure measurements of open circuit potential (OCP) and linear polarization resistance (LPR) curves. After ended OCP/LPR measurements, the samples will be subjected to potentiodynamic scans to measure the polarization curves. The oxide layer created will be analyzed using a scanning electron microscopy (SEM). An optical microscope will be used for visual inspections to document the surface conditions after exposure.

5.2 Test Material

Due to a limited amount of test material available from Herøysundet bridge, the test materials used in the experiments were gathered from Farriseidet bridge. Farriseide bridge used to be located outside Larvik and was removed in 2014. It was constructed around the same time as Herøysundet bridge and was built using the same type

of reinforcement materials. In Figure 5.1, the test material from Farriseide bridge is displayed. The release of the tensile wires, as depicted on the right side in Figure 5.1, was performed by the Department of Structural Engineering (KT) at NTNU.

Figure 5.1: Test materials from Farriseide bridge. Left: A section of concrete extracted, containing a tendon duct with tensile wires embedded in grout. Right: Tendon duct and tensile wires after removal of concrete and grout [50].

.

5.3 Sample Preparation

The test samples used in the experiments consisted of tensile wires with a diameter of 6 mm, which were extracted from Farriseidet bridge. These were cut into test samples with a length of ∼80 mm using a cutting machine. Grinding was then performed with emery paper up to grade 500 on a polishing machine to remove sharp and uneven edges. The surface of the samples was grinded by hand, also on grade 500 emery paper, to remove corrosion residue and any traces of a previous oxide layer on the surface. To achieve a defined test area, two sections of the samples were painted with Jotamastic 87 from Jotun according to the measurements in Figure 5.2. This left a surface area of 376 mm^2 to be exposed to the electrolyte. One end of the sample was left unpainted in order to serve as a contact point for electrical connections. Once painted, the samples were placed in a ventilated oven for 48 hours in order for the paint to cure completely. The painting process was repeated once to secure full coverage of the sharp edges on the tip of the samples.

In addition to the rods, pieces of the wires were cut to a length of ∼5 mm. The cross section was polished with emery paper up to grade 500. These were made in order for the purpose of later studying the oxide layer with SEM.

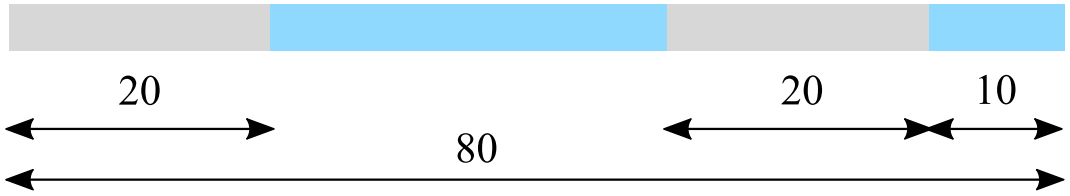

Figure 5.2: The test samples with dimensions given in mm. Areas with coating in blue and areas without coating in gray

5.4 Oxide Layer Development

In order to create conditions similar to the ones found on steel exposed to concrete, a passive oxide layer was created on the surface of the steel. The experimental setup of the cell is schematically shown in Figure 5.3. A simulated pore solution was created according to Table 5.1 using distilled water. The solution was similar to pore solutions used in other tests according to literature, as documented in Chapter 4. As the solution was oversaturated, it was left for 24 hours at room temperature before the suspended $Ca(OH)_2$ solids were filtered out of the electrolyte using filtering paper with a particle size of 5-13 μm. The final solution was clear and had a pH of ~13.5.

Table 5.1: Composition of the synthetic pore solution used for creating an oxide layer on the samples.

NaOH (g/L)	KOH (g/L)	$Ca(OH)_2$ (g/L)
3.7	10.5	2.1

The larger samples were then placed in the solution as shown in Figure 5.3. One of the samples was connected to a potentiostat to measure the open circuit potential (OCP) on the surface of the steel as the oxide layer developed. The smaller samples were left on the bottom of the beaker. After a week in the experimental setup, the samples were placed in a desiccator until they were going to be used in the corrosion testing. Due to the number of samples needed, the process was repeated several times.

5.5 Corrosion Testing

5.5.1 Electrolyte

The base electrolyte solution was made by adding 2 g/L $Ca(OH)_2$ to distilled water. As the solution was oversaturated, it was left for 24 hours at room temperature before the

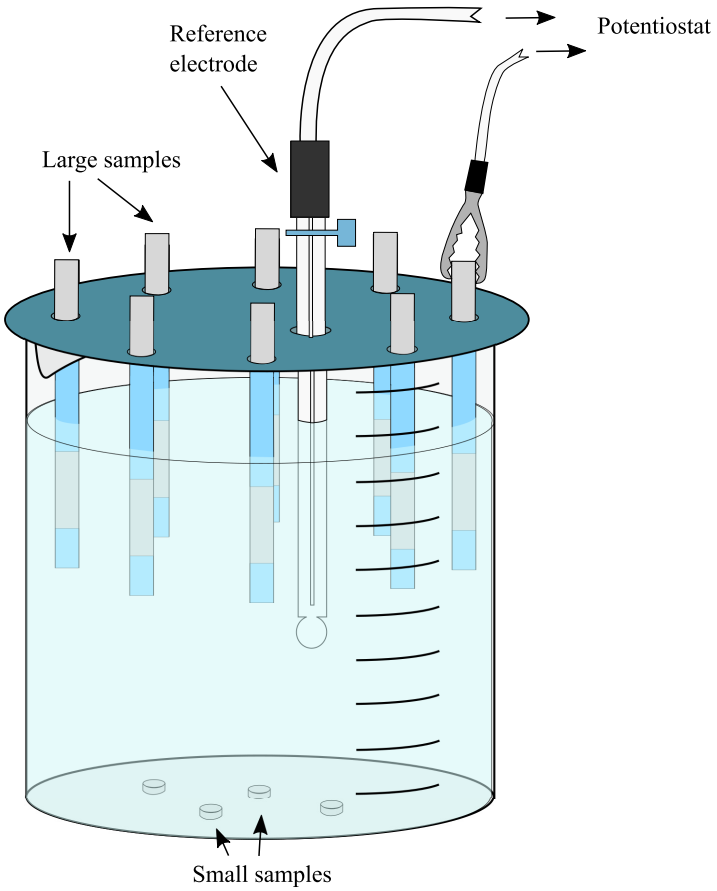

Figure 5.3: An illustration of the experimental setup for the buildup of an oxide layer.

suspended $Ca(OH)_2$ was filtered out of the solution using filtering paper with a particle retention of 5-13 μm. The final solution was clear and had a pH of $\sim$ 12.5.

For some solutions, an addition of NaCl was given to vary the Cl^- ion content. In other solutions, either Na_2SO_4 or $MgSO_4$ were added to vary the SO_4^{2-} ion content. A few solutions were given an addition of both Cl^- and SO_4^{2-} ions, in order to study the combined effect. The $MgSO_4$ salt had a purity of 98%. An addition of either NaCl, Na_2SO_4 or $MgSO_4$ would change the pH, therefore the pH had to be fixed for these solutions. 10M KOH solution was used to increase the pH, as this prevented changing the concentration of the solution. The different solutions created is displayed in Figure 5.7 and 5.8 in Subsection 5.5.5.

5.5.2 Exposure Conditions

All tests were performed at room temperature, corresponding to 21 $\pm$ 2 °C. Oxygen was present in the solution for some of the tests, while removed in others, see Figure 5.7

and 5.8. To remove the oxygen, N_2 gas was used to purge the solution during the test period.

5.5.3 Equipment

For experiments following ASTM G61 and for OCP/LPR measurements run without the presence of oxygen, the test container used was made of glass. The container and the experimental setup are displayed in Figure 5.4. The container had a length of 73 mm and an internal diameter of 40 mm, which corresponds to a total electrolyte volume of 183.4 mL. For electrochemical measurements, the test samples were used as the working electrodes, a platinum wire served as counter electrode and an Ag/AgCl (3 M KCl saturated electrode) served as the reference electrode. The correlations between an Ag/AgCl electrode and electrodes used in literature and previous research are given in Figure 5.6. To measure polarization curves and monitor OCP and LPR, a potentiostat (Interface 600, Gamry instruments ®) was used.

(a) **(b)**

Figure 5.4: a) and b) shows the equipment and setup for the ASTM G61 tests.

For OCP/LPR measurements run with oxygen present in the solution, a setup was created according to Figure 5.5a. A beaker with an internal volume of 600 mL was used as the container in this setup. The reference electrode was an Ag/AgCl (3 M KCL saturated) electrode, a platinum mesh served as the counter electrode, and one or two samples were immersed. One sample was connected to the potentiostat to monitor OCP and measure LPR while the other was connected to a potential logger that continuously measured OCP throughout the entire exposure period.

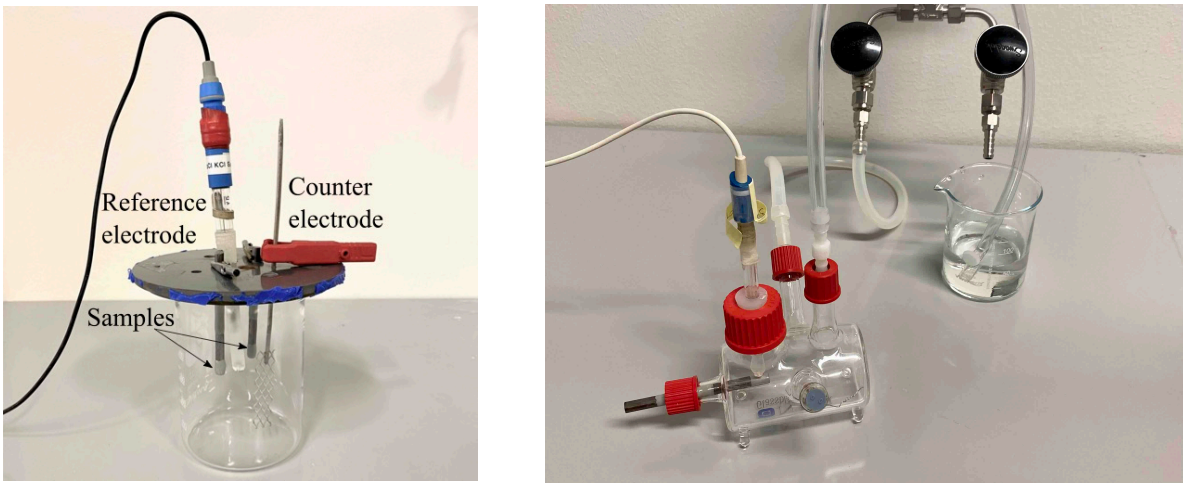

(a) **(b)**

Figure 5.5: a) and b) shows the equipment and setup for OCP/LPR measurements with and without oxygen present, respectively.

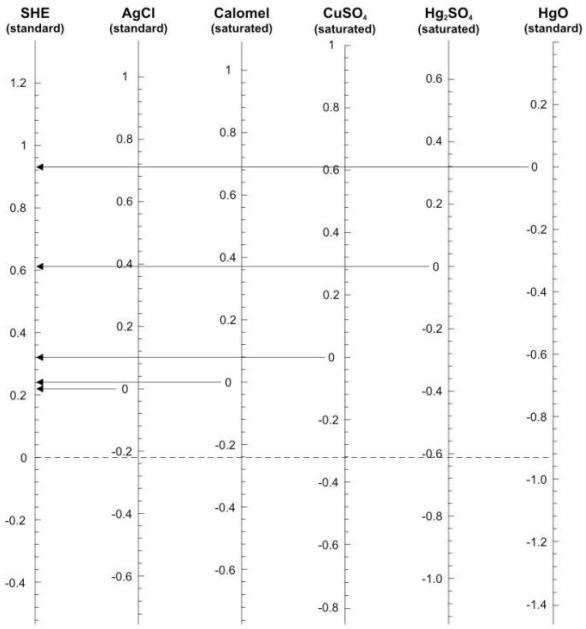

Figure 5.6: Correlations between common electrodes [102].

5.5.4 Corrosion Tests

Method A - ASTM G61

The objective of method A is to find the pitting potential, E_{pit}, and the repassivation potential, E_{rep}.

Procedure:

- Tests run without oxygen:
  - Measure OCP while bubbling nitrogen through the solution for an hour prior to starting polarization.
- Test run with oxygen:
  - Measure the OCP during one hour of exposure to solution prior to starting polarization.
- Polarization measurements according to ASTM G61.
- Visual examination of the sample surface after testing to document possible corrosion attacks.

The polarization was started at an OCP of -100 mV and was polarized with a speed of 600 mV/hour in the anodic direction. This proceeded until the anodic current density reached 100 μA/cm^2. The polarization was then reversed to polarize in the cathodic direction until E_{Rep} was reached.

From the tests using method A, the following results were gathered:

- The OCP development during the initial one hour of exposure.
- Polarization curves.
- An estimation of E_{pit}, E_{Rep} and the anodic current density i_A.
- Visual inspection of the sample surfaces.

Method B - Long-term Exposure

The objective of method B is to i) examine the potential development and the corrosion current density in order to compare it to the pitting potential, E_{pit}, and the repassivation potential, E_{rep}, under true exposure conditions, and ii) investigate the surface condition after the exposure period (i.e. has corrosion been initiated and to what extent).

Procedure:

- Measure the OCP continuously for the entire duration of the experiment
- Measure LPR (± 10 mV) every 24 hours. Begin one hour after starting OCP measurements and measure the corresponding current change I.
- Exposure period varying from 14 to 30 days.
- For tests run with two samples immersed, one shall be used to run a potentiodynamic scan after ended exposure period.
- Visual examination of the sample surface after testing to document possible corrosion attacks.

The LPR scans were performed with a scan rate of 0.1667 mV/s, starting from -5 to +5 mV relative to the OCP. The Stern-Geary equation, Equation 5.2, was used to calculate the corrosion current density, i_{corr}. The potentiodynamic scan ran from OCP - 500 mV to OCP + 500 mV with a scan rate of 0.1667 mV/s.

Corrosion current densities and corrosion rates values were calculated based on polarization resistance values, R_P. These values were extracted from the LPR measurements using the Gamry Echem Analyst software. The R_P values were extracted from the software assuming both Tafel constants, b, to be equal to 120 mV/decade, see Equation 5.1. This is a typical value for the Tafel slope at 25°C, given a composite transfer coefficient for oxidation, α, of 0.5 [39].

$$b = \frac{RT \cdot ln\{10\}}{|\alpha|F} \xrightarrow{25°C} \frac{59.16mV}{|\alpha|}, \tag{5.1}$$

where b represents a Tafel slope, R is the gas constant, T is the temperature, α is the composite transfer coefficient and F is the Faraday constant. The calculations used for determining the i_{corr} follow the Stern-Geary equation, listed below.

$$i_{corr} = B/[R_P A] = \frac{b_A \cdot b_C}{2.3(b_A + b_C)R_P A}, \tag{5.2}$$

where

$$R_P = \Delta E/\Delta I. \tag{5.3}$$

In the equations listed above, B is the Stern-Geary constant, R_P is the polarization resistance, A is the total area of the sample exposed to the electrolyte, b_A and b_C are

the Tafel constants, ΔE is the change in potential and ΔI is the change in current. The Stern-Geary constant is a function of the Tafel slopes and have been found by Andrade et al. to be 26 mV for active steel [103]. This corresponds to Tafel constants of 120 mV/decade, as can be found when inserting the Tafel values into the Stern-Geary equation, Equation 5.2.

Further, the corrosion rate, v_{corr} [mm/year], was calculated using Faradays law, which was simplified for steel into Equation 5.4. Here it was assumed uniform corrosion on the sample surface.

$$v_{corr} = 0.0116 \cdot i_{corr}, \tag{5.4}$$

when $[i_{corr}] = \mu A/cm^2$.

From the tests using method B, the following results were gathered:

- The OCP development as a function of time.
- The R_p values (E/I) during the exposure period.
- Visual inspection of the sample surface.
- For some tests: potentiodynamic scans.

5.5.5 Test Programs

The test programs for the Specialization project were decided upon following the conclusions of preliminary reports, previous work [50, 79] and literary research, see Chapter 4. Further, the test programs used for the specialization project, along with the results from inspections performed on Herøysundet bridge, served as a basis for the test programs used for the Master thesis. As can be seen in Figure 5.7 and 5.8, the content of Cl^- and SO_4^{2-} ions, the presence of oxygen and the pH-level varied throughout the different tests.

Method A

For method A, the different test solutions are given in Figure 5.7.

Solution	pH	Cl^- (M)	Cl^- (g/L)	SO_4^{2-} (M)	SO_4^{2-} (g/L)	H^+	OH^-	$[Cl^-]/[OH^-]$	$[SO_4^{2-}]/[OH^-]$	Oxygen	G61
1	12	0,1	3,545			1E-12	0,01	10		Yes	x
2	12	0,1	3,545			1E-12	0,01	10		No	x
3	12	0,4	14,18			1E-12	0,01	40		Yes	x
4	12,5	0,1	3,545			3,16228E-13	0,03162278	3,16227766		No	x
5	12,5	0,1	3,545			3,16228E-13	0,03162278	3,16227766		Yes	x
6	13	0,4	14,18			1E-13	0,1	4		Yes	x
7	12,5			0,2082032	20*	3,16228E-13	0,03162278		6,583963281	Yes	x
8	13,5			0,2082032	20*	3,16228E-14	0,31622777		0,658396328	Yes	x
9	12,5	0,1	3,545	0,2082032	20*	3,16228E-13	0,03162278	3,16227766	6,583963281	Yes	x
*Na2SO4											

(a) Tests matrix used during the preliminary specialization project for method A.

Solution	pH	Cl^- (M)	Cl^- (g/L)	SO_4^{2-} (M)	SO_4^{2-} (g/L)	H^+	OH^-	$[Cl^-]/[OH^-]$	$[SO_4^{2-}]/[OH^-]$	Oxygen	G61
10	12,5					3,16228E-13	0,03162278			Yes	x
11	13					1E-13	0,1			Yes	x
12	13					1E-13	0,1			No	x
13	12,5	0,001	0,036			3,16228E-13	0,03162278	0,03162278		Yes	x
14	13	0,001	0,036			1E-13	0,1	0,01		Yes	x
15	12,5	0,01	0,36			3,16228E-13	0,03162278	0,31622777		Yes	x
16	13	0,01	0,36			1E-13	0,1	0,1		Yes	x
17	12,5			0,2082032	20**	3,16228E-13	0,03162278		6,583963281	Yes	x
18	13,5			0,2082032	20**	3,16228E-14	0,31622777		0,658396328	Yes	x
19	12,5	0,1	3,545	0,2082032	20**	3,16228E-13	0,03162278	3,16227766	6,583963281	Yes	x
20	12,5	0,01	0,36			3,16228E-13	0,03162278	0,31622777		No	x
21	12,5	0,005	0,17725			3,16228E-13	0,03162278	0,15811388		Yes	x
22	12,5	0,0075	0,265875			3,16228E-13	0,03162278	0,23717082		Yes	x
23	12,5	0,0025	0,088625			3,16228E-13	0,03162278	0,07905694		Yes	x
**MgSO4											

(b) Test matrix used during this thesis following method A.

Figure 5.7: Test programs - method A.

From here on out, the different solutions and corresponding samples are labeled and referred to according to the numbering given in the first column in the test matrix in Figure 5.7.

Notes to method A:

- Solution 1-9, given in Figure 5.7a, were completed during the preliminary specialization project during the fall of 2021. Results are given in Appendix D, section D.1.

Method B

For method B, the different test solutions are given in Figure 5.8.

Solution	pH	Cl^- (M)	Cl^- (g/L)	SO_4^{2-} (M)	SO_4^{2-} (g/L)	H^+	OH^-	$[Cl^-]/[OH^-]$	$[SO_4^{2-}]/[OH^-]$	Oxygen	OCP/LPR
5A	12,5	0,1	3,545			3,1623E-13	0,031623	3,16		Yes	x

(a) Tests matrix during specialization project for method B.

Solution	pH	Cl^- (M)	Cl^- (g/L)	SO_4^{2-} (M)	SO_4^{2-} (g/L)	H^+	OH^-	$[Cl^-]/[OH^-]$	$[SO_4^{2-}]/[OH^-]$	Oxygen	OCP/LPR
3	12	0,4	14,18			1E-12	0,01	40		Yes	x
4	12,5	0,1	3,545			3,1623E-13	0,03162278	3,16227766		No	x
5B	12,5	0,1	3,545			3,1623E-13	0,03162278	3,16227766		Yes	x
9	12,5	0,1	3,545	0,2082032	20*	3,1623E-13	0,03162278	3,16227766	6,583963281	Yes	x
10	12,5					3,1623E-13	0,03162278			Yes	x
13	12,5	0,001	0,036			3,1623E-13	0,03162278	0,03162278		Yes	x
14	13	0,001	0,036			1E-13	0,1	0,01		Yes	x
15	12,5	0,01	0,36			3,1623E-13	0,03162278	0,31622777		Yes	xx
16	13	0,01	0,36			1E-13	0,1	0,1		Yes	x
19	12,5	0,1	3,545	0,2082032	20**	3,1623E-13	0,03162278	3,16227766	6,583963281	Yes	x
21	12,5	0,005	0,17725			3,1623E-13	0,03162278	0,15811388		Yes	x
22	12,5	0,0075	0,265875			3,1623E-13	0,03162278	0,23717082		Yes	x
24	13	0,005	0,17725			1E-13	0,1	0,05		Yes	x
25	12,5	0,01	0,3545	0,2082032	20**	3,1623E-13	0,03162278	0,31622777	6,583963281	Yes	xx
*Na2SO4	**MgSO4										

(b) Test matrix used during this thesis following method B.

Figure 5.8: Test programs - method B.

Notes to method B:

- 1 test, given in Figure 5.8a, was completed during the preliminary specialization project during the fall of 2021. Results are given in Appendix D, section D.2.
- Solutions 3, 5B and 9 in Figure 5.8b were run over Christmas and results will be included in this report.
- Solutions 9 and 15 were run with only one sample, which was connected to a potential logger. Therefore, these solutions lack LPR measurements.
- Solution 15 and 25 were also used to run tests with samples that had the oxide layer grinded away, marked with xx under the OCP/LPR column in Figure 5.8b. This was done to measure the potential development with the bare steel exposed to the solution.

5.6 Surface Investigation

5.6.1 Oxide Layer

In order to analyze the oxide layer developed on the surface, scanning electron microscopy (SEM) was used. Two of the smaller samples created was prepared for the SEM by being rinsed with distilled water and acetone. This would remove unwanted particles, but not damage the oxide layer. The samples were placed with the cross section facing upwards. Visual inspections were performed using a voltage of 10 kW and an aperture of 30 μm. The low voltage was applied to prevent the electrons from penetrating through the oxide layer and into the metal.

To determine the chemical composition of the oxide, energy-dispersive X-ray spectroscopy (EDS) analyses were performed. The aperture was changed to 100 μm. This resulted in poorer resolution in the images, but faster scan rates. With EDS, both a point analysis and a mapping analysis were performed.

SEM and EDS analyzes were also performed on as-delivered samples to compare the composition of the naturally formed and chemically created oxide layers.

5.6.2 Visual Inspections

Visual examinations were performed on all samples after ended corrosion tests in order to determine the approximate size of surface area subjected to corrosion attacks. A simple ruler was used for measurements.

Samples displaying little to no visible corrosion were examined more thoroughly using an optical microscope (OM). The microscope used was an Olympus BX53M optical microscope, and the surfaces were examined using a lens with a 10X magnification.

Chapter 6

Results

Summaries of the results from the specialization project that will later be used in the discussion, see Chapter 7, are included prior to current results.

6.1 Oxide Layer

Results from the Specialization Project

During the preliminary work, the following results were gathered from analyses of the oxide layer:

- The oxide layer began to stabilize after approximately 6 days at a potential of -0.116 V vs. Ag/AgCl.
- SEM analysis revealed oxides of various sizes present on the surface with a tendency to form clusters.
- The main components were found to be oxygen, calcium and carbon from an EDS point analysis.
- An EDS mapping analysis confirmed the findings of oxygen, calcium and carbon as the major components in the oxide. In addition, the analysis revealed areas dominated by iron in between the oxide clusters.

The results are based on the plots and images given in section D.3.

Results from the Master's Thesis

Samples were oxidized in four different sets. Figure 6.1 shows the potential development on the surface of the samples during the development of the oxide layers. It is clear that an oxide layer has started to form during all the different processes due to the increase in potential. As the potential development for all sets follow the same path and end up at potentials of approximately -0.14 V vs. Ag/AgCl after seven days of exposure, the samples developed similar oxide layers prior to testing.

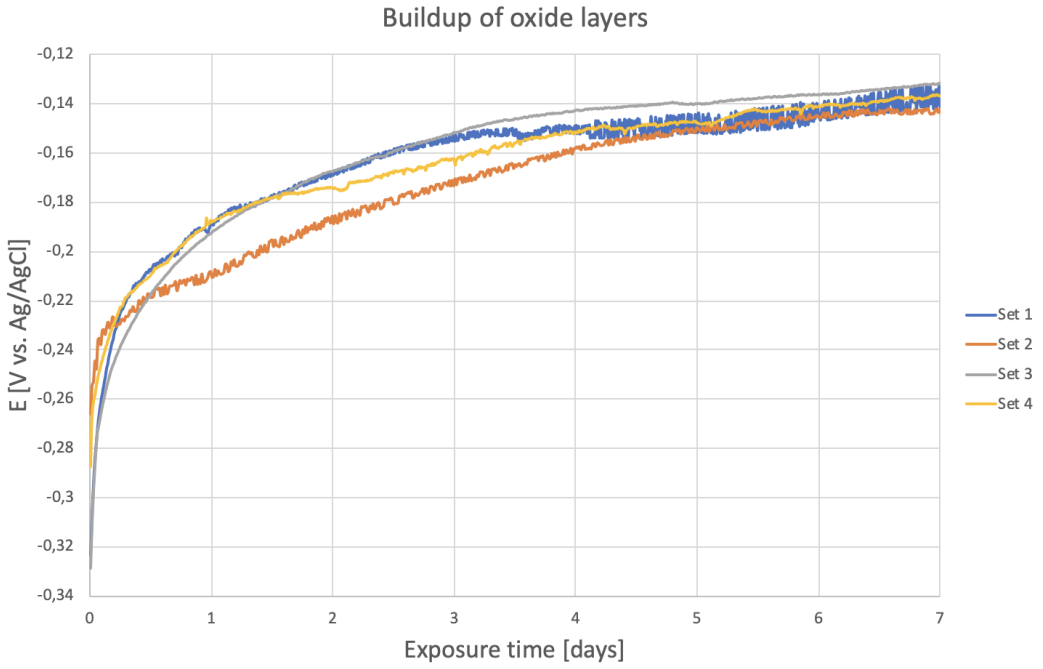

Figure 6.1: OCP measurements made during the development of oxide layers on the surfaces.

6.1.1 SEM Analysis

Figure 6.2 shows the surface of an as-delivered sample at a magnification of 5000x. The sample has not been grinded and the oxide layer visible was built up during its service lifetime in Farriseidet bridge. Peaks and minor groves are in the image, most likely a result of oxide precipitates growing into one another over time. However, the oxide appears to be thick and to provide an overall even coverage of the steel surface.

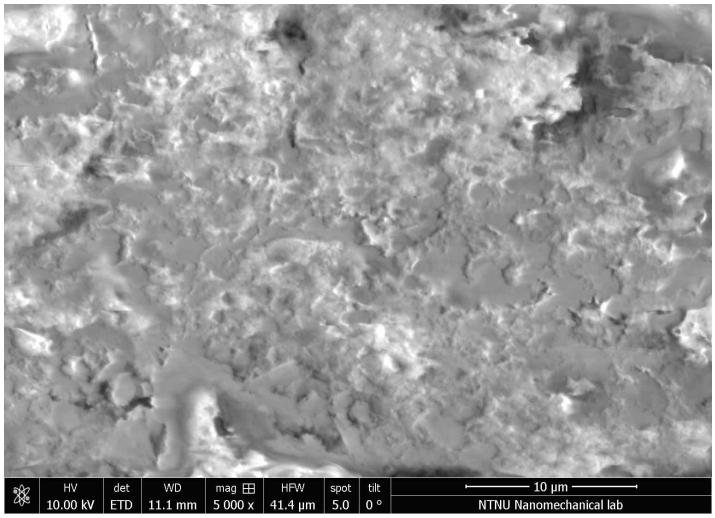

Figure 6.2: Image taken with SEM at a magnification of 5000x.

6.1.2 EDS Analyses

Point Analysis

The sites used for the point analysis is displayed in Figure 6.3. From the different spectrum analyses, the occurrence of elements present on the surface was found. An average from all the sites has been calculated and is displayed in Table 6.1. The point analyses revealed the main elements on the surface to be oxygen, calcium and carbon, when considering atomic%. Traces of sulfur, phosphate, iron, silicon, aluminum and magnesium have also been detected.

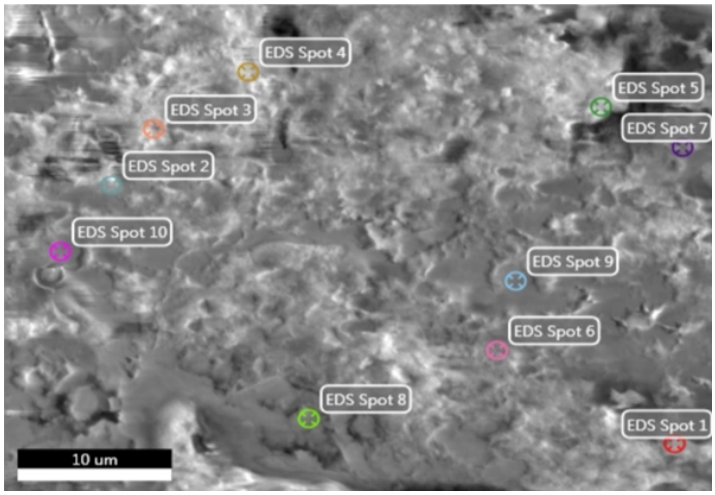

Figure 6.3: Overview of the sites used for the point analysis on the as-delivered sample.

Table 6.1: Average results from the point analysis performed on the as-delivered sample.

Element	Weight %	Atomic %	Error %
O	43.19	56.70	9.15
C	9.57	16.59	8.71
Ca	16.26	8.77	13.50
P	3.12	2.39	26.22
Si	2.76	2.15	6.95
S	3.44	1.76	39.07
Fe	2.92	1.10	22.38
Al	1.10	0.88	18.62
Mg	0.30	0.26	52.66

Mapping Analysis

Figure 6.4a shows an element overlay map created during the mapping analysis. The map illustrates the most dominant elements found on the surface, with color coding according to Figure 6.4b. The map clearly indicates that oxygen and calcium are the dominating elements on the surface, with minor traces of other elements appearing in between. From the mapping analysis, other results gathered includes a live map, a spectrum analysis and individual element overlay maps. These results are displayed in Appendix C.

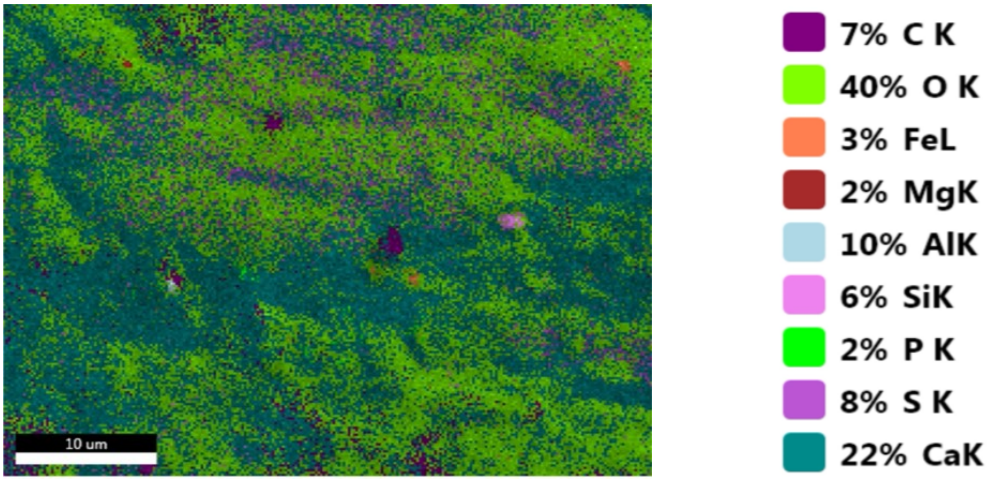

(a) **(b)**

Figure 6.4: Shows the element overlay map with color explanations and results from the EDS mapping analysis of the as-delivered sample.

The mapping analysis also gave an indication of what elements presented themselves on the surface with regards to weight % and atomic %. These are presented in Table 6.2. Main elements, based on atomic%, was found to be oxygen, calcium and carbon.

Table 6.2: Results from the mapping analysis performed on the as-delivered sample.

Element	Weight %	Atomic %	Error %
O	44.90	58.45	8.29
Ca	31.58	16.41	3.01
C	9.00	15.61	7.55
Al	4.20	3.24	3.69
S	4.53	2.94	2.91
Si	2.24	1.66	3.47
Fe	2.58	0.96	8.41
P	0.58	0.39	4.14
Mg	0.40	0.35	4.97

6.2 Corrosion Testing

6.2.1 Method A

Results from the Specialization Project

During the preliminary work, the following results were gathered from method A.

- Among the solutions given in Figure 5.7a, the most corrosive were 4 and 5, which had a pH level of 12.5 and a chloride content level of 0.1 M. They displayed large hysteresis loops and low repassivation potentials in Figure D.1.
- An addition of 0.21 M sulfate caused a reduction in corrosivity, as can be seen in a reduction in the hysteresis loop.
- Solutions containing only sulfates, introduced from $NaSO_4$, caused no visible signs of corrosion on the samples. The reduction in corrosivity can be seen from the lack of and negative hysteresis loops.

The results are based on the plots and images given in section D.1.

Results from the Master's Thesis

Cyclic Polarization Curves

Table 6.3 presents parameters extracted form the cyclic polarization (CP) plots gathered using method A. All individual CP plots are displayed Appendix A, along with images from visual inspections of corroded samples. The corrosion potential is here denoted as OCP. The pitting potential, E_{pit}, is defined here as the potential in the forward scan where there is a sharp increase in current density. The repassivation potential, E_{rep}, is defined as the potential where the reversed scan crosses the average current density in the passive region during the increase in potential.

Table 6.3: Results from method A. Data extracted from the polarization curves shown in Figure 6.5.

Solution[1]	OCP [$mV_{Ag/AgCl}$]	E_{pit} [$mV_{Ag/AgCl}$]	E_{rep} [$mV_{Ag/AgCl}$]	$I_{pass}1$ [μA]	$I_{pass}2$ [μA]
10	-326	523	NA	6.47	NA
11	-349	474	NA	5.43	NA
12	-358	499	NA	5.78	NA
13	-328	528	NA	5.72	NA
14	-352	503	NA	6.05	NA
15	-346	485	-898	4.22	11 600
16	-360	504	-879	12.35	11 263
17	-373	506	-436	6.48	NA
18	-279	490	NA	6.97	NA
19	-275	527	-704	7.32	22 178
20	-270	507	-704	4.51	8195
21	-357	611	-871	25.63	4414
22	-297	526	-888	10.18	4152
23	-331	599	-874	11.88	4775

[1] Solutions referred to according to Figure 5.7.

Notes to Table 6.3:

- $I_{pass}1$: Average anodic current in the passive region during the increase of the potential.
- $I_{pass}2$: Average anodic current in the passive region during the decrease of the potential.
- NA: The polarization curve has a positive hysteresis loop, indicating that after

reaching maximum potential it has no active part.

All cyclic polarization curves measured according to method A are displayed in Figure 6.5. A common denominator for all samples is that they display passive behavior at the corrosion potential, OCP. The corrosion potentials vary little from each other and all solutions display potentials between -270 mV vs. Ag/AgCl and -373 mV vs. Ag/AgCl. As the current density increases and the potentials increase above OCP, all samples stay passive and move into a passive region with current densities in the order of 0.02-3 μA/cm^2.

From the cyclic polarization (CP) plots in Figure 6.5, the corrosion initiation is illustrated by the sudden increase in current density, which arises after the pitting potential has been reached. The current density remains high as the potential decreases with the reversal of the scan. For all corroded samples, see Table 6.4, a key observation is that E_{rep} is not reached during the reversed scan until the potentials are below OCP. This shows that once corrosion is initiated, anodic dissolution continue in the solution without the overpotential applied by the potentiostat. Some of the samples does not show any signs of corrosion, see Table 6.4, and have CP plots that display positive hysteresis loops. These are indicated in Figure 6.5 by arrows showing the direction of the polarization.

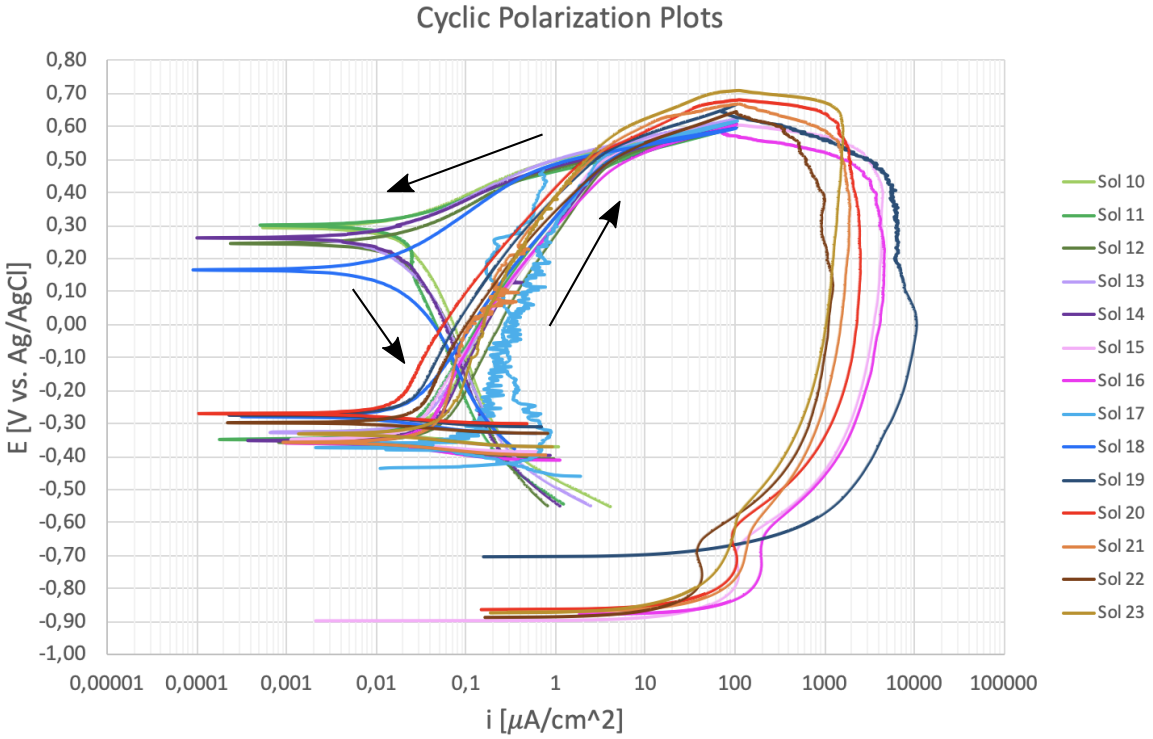

Figure 6.5: All CP plots measured according to method A.

A change is clearly visible in the size of the area beneath the hysteresis loop as the chloride ion concentration exceeds 0.001 M. With a pH of 12.5, samples display large hysteresis loops with chloride concentrations as low as 0.0025 M, see Figure 6.6. Solution 10 and 13, which have no chlorides and a content of 0.001 M Cl^-, respectively, display positive hysteresis loops. The samples immersed in these solutions does not exhibit any visible signs of corrosion.

However, as the chloride content is increased to 0.0025 M and higher, the samples immersed in these solutions visibly corrode, see Appendix A, Figure A.3. With an increase in chloride concentration from 0.0025 M and upwards, follows a decrease in the pitting potential. The slope of the passive region becomes less steep with the increase of chloride concentration, indicating an increase in corrosivity of the solution. In addition, the increasing chloride concentration also results in higher corrosion current densities being reached.

From Figure 6.6, it is clear that the removal of oxygen in solution 20 leads to a decrease in corrosivity. This can be seen by the increase in pitting potential, increase in corrosion potential and from the shift in both the passive area and the active area to lower current densities, compared to solution 15.

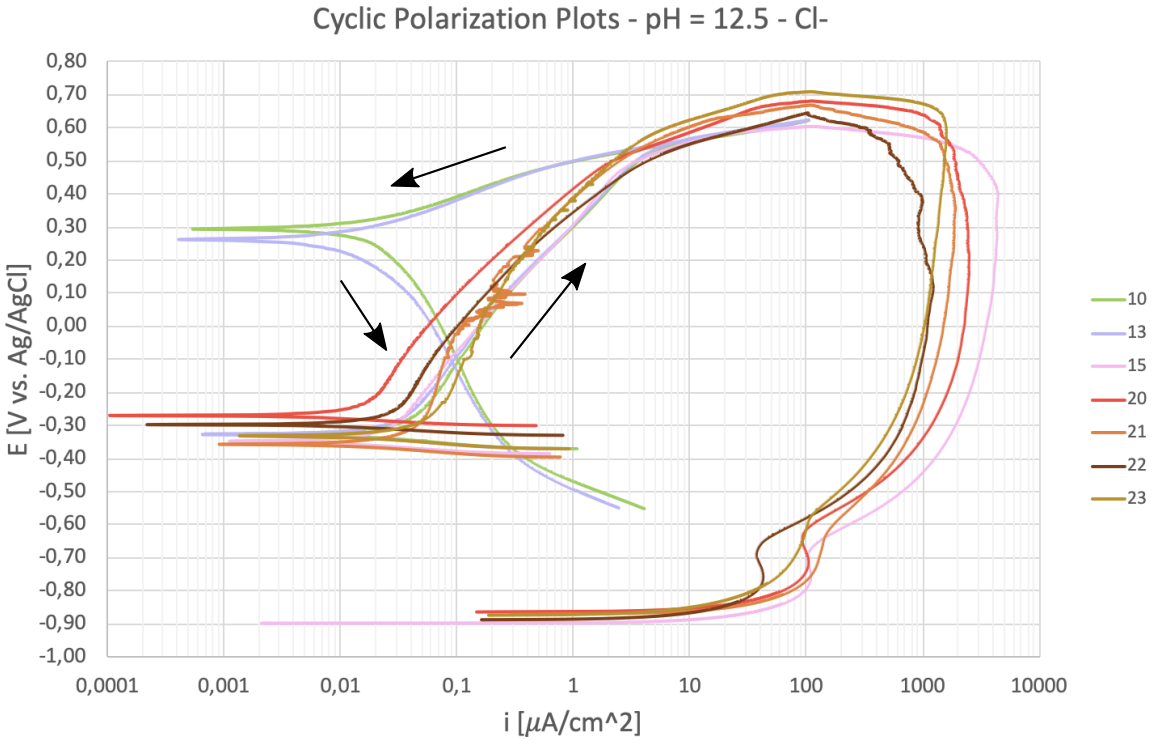

Figure 6.6: CP plots of solutions with a pH of 12.5 and varying chloride concentrations.

With a pH $\geq$ 13, corrosion is only initiated in solution 16, which has a chloride concentration of 0.01 M, see Figure 6.7. Lower concentrations results in positive hysteresis loops and no signs of visible corrosion. In solution 18, there is an addition of sulfate ions instead of chloride ions. At these pH levels, this made the solution less aggressive, demonstrated by an increase in OCP.

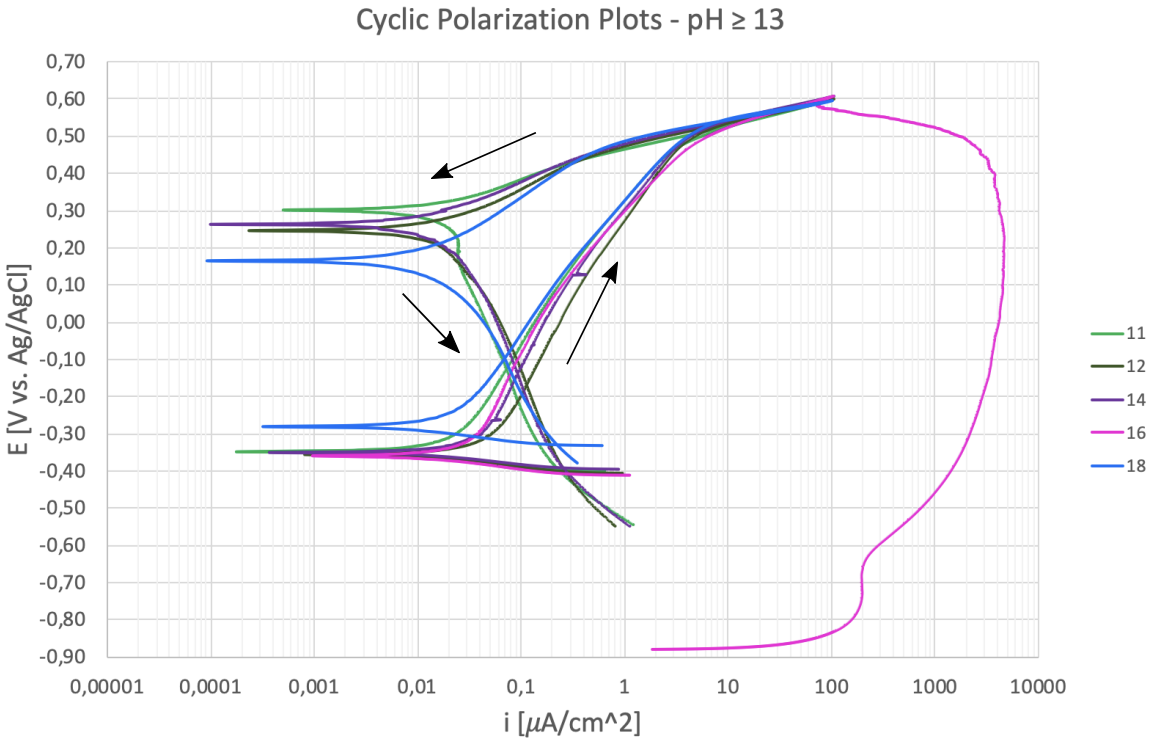

Figure 6.7: CP plots of solutions with a pH of 13. The solutions have varying chloride concentrations, except for solution 18, which only contain a SO_4^{2-} concentration of 0.21 M.

The cyclic polarization plots of the solutions containing magnesium sulfate are displayed in Figure 6.8. Solution 18, which has a pH of 13.5 and no chloride ions present in the solution, display a positive hysteresis loop and no visible signs of corrosion. The decrease in pH to 12.5, as is the case with solution 17, causes the scan to cross itself during the reversal. This entails that the initial positive hysteresis loop turn negative. Solution 17 also display signs of metastable pitting during the passive stage of the forward scan. As can be seen in Figure A.3, the sample in solution 17 show corrosion on the exposed surface area. It is also worth noting that solution 17 display both a lower corrosion potential and a steeper passive region located at higher current densities, compared to the other two solutions containing magnesium sulfate.

The most corroded sample out of all tests run according to method A is the sample

immersed in solution 19. Compared to all solutions displayed in Figure 6.5, solution 19 display the highest anodic current density reached during the reversal of the scan. When only regarding the solutions with magnesium sulfate present, solution 19 is the only solution that display a solely negative hysteresis loop.

During testing, the solutions containing magnesium sulfate separated, leaving a visible difference in the electrolytes, see Figure A.2c.

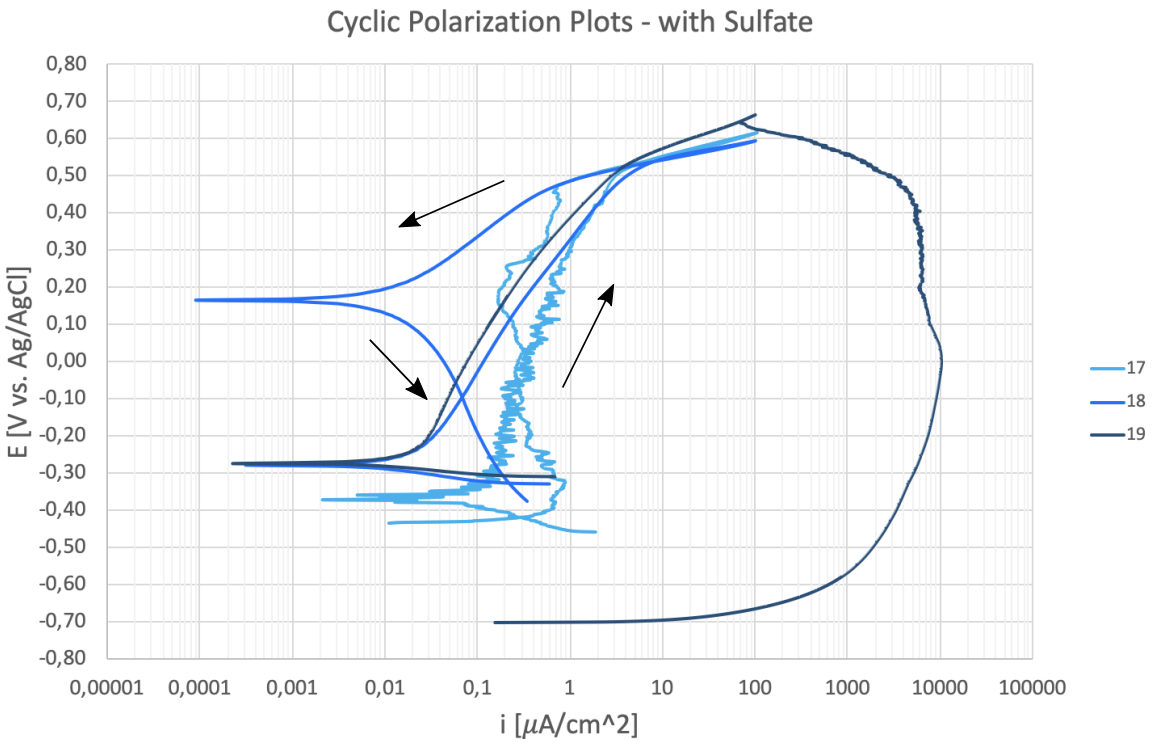

Figure 6.8: CP plots of solutions containing sulfate. Solution 19 also contain an addition of 0.1 M Cl^-.

Visual Inspections

Visual inspections performed on the samples at the end of the corrosion testing results in an approximation of corroded surface area, which is presented in Table 6.4. The table is sorted to display the samples from the most to the least corroded. Images displaying the corroded samples are given in Appendix A, Figure A.3. From Table 6.4, it is clear that an increasing chloride concentration results in an increase in corroded surface area. It can also be seen that the addition of magnesium sulfate contribute to causing the largest corrosion attack among the solutions.

Table 6.4: The percentage of the surface area subjected to corrosion.

Sample[1]	Percentage of Area Corroded [%]
19	65-70
15	20-25
21	20-25
16	15-20
20	15-20
17	5-10
22	5-10
23	5-10
10	0
11	0
12	0
13	0
14	0
18	0

[1] Sample number refers to the solutions given in Figure 5.7.

Summarized Findings from Method A

1. At a pH of 12.5, the samples begin to visible corrode as the chloride concentration exceeds 0.0025 M. This corresponds to the formation of large negative hysteresis loops with repassivation potentials below the corrosion potentials.
2. The removal of oxygen from a corrosive solution causes a decrease in corrosivity, visible by increased OCP and E_{pit} and by shifting the curve to lower current densities.
3. With a pH $\geq$ 13 The chloride concentration has to be raised to 0.01 M in order to cause corrosion of the samples.
4. In solutions only containing magnesium sulfate, there is little to no corrosion visible in the solution. However, the combination of Cl^- and SO_4^{2-} from magnesium sulfate makes the solution highly corrosive. More so than the solution only containing chlorides.

6.2.2 Method B

Results from the Master's Thesis

Most tests performed with oxygen present, according to method B, had two samples immersed in the same solution. On one parallel, connected to the Gamry potentiostat, both OCP and LPR measurements were performed, while on the other parallel, only OCP was measured. The results from the individual measurements of both parallels are displayed in Figure B.1 in Appendix B. Results from the measurements made with the Gamry potentiostat are given in Table 6.5.

As mentioned in Subection 5.5.4, the calculations of i_{corr} and v_{corr} are made from LPR measurements assuming the Stern-Geary constant to be B = 26 mV. In addition, the calculations are made using a constant exposure area equal to the original area of 376 mm^2. Images from visual inspections of corroded samples are displayed in Appendix B, Figure B.7.

Table 6.5: Results from method B. Data extracted from the polarization curves shown in Figure 6.9, 6.13a and 6.13b

Solution[1]	OCP-start [$mV_{Ag/AgCl}$]	OCP-finish [$mV_{Ag/AgCl}$]	i_{corr}−start [$\mu A/cm^2$]	i_{corr}−finish [$\mu A/cm^2$]
3	-342	-666	3.83	38.83
4	-321	-335	0.05	0.52
5B	-309	-553	0.36	5.87
9[2]	-283	-530	-	-
10	-253	-130	0.09	0.05
13	-62	-111	0.05	0.07
14	-71	-107	0.04	0.03
15[2]	-111	-96	-	-
16	-250	-328	0.36	0.20
19	-333	-462	0.63	5.63
21	-159	-122	0.07	0.05
22	-131	-157	0.04	0.04
24	-147	-95	0.03	0.03
25	-242	-81	0.04	0.04

[1] Solution referred to according to Figure 5.8.

[2] Measurements made with the potential logger.

Notes to Table 6.5:

- OCP-start: Potential measured 1 hour after start.
- OCP-finish: Potential measured at the end of the experiment, after either 14, 21 or 30 days.
- i_{corr}-start: Corrosion current density calculated from LPR measurements 1 hour after start.
- i_{corr}-finish: Corrosion current density calculated from LPR measurements at the end of the experiment, after either 14, 21 or 30 days.
- - : No LPR measurements performed

OCP Measurements

Most of the samples have an exposure period of 21 days, with a few exceptions, as shown in Figure 6.9. The potential developments shown in Figure 6.9 are gathered from the samples connected to the Gamry potentiostat, except for solution 9 and 15, where both samples are connected to a potential logger. There is a clear distinction visible between two potential range groups. Solutions with a chloride concentration $\leq$ 0.01 M display relatively stable potential developments with potentials between $\sim$-50 and $\sim$-150 mV vs. Ag/AgCl, indicating passive behavior. As the chloride concentration in the solution exceeds 0.01 M, the potentials becomes significantly lower. These samples display typical corrosive behavior with turbulent potential developments at lower potentials. The potentials range from $\sim$-250 mV vs. Ag/AgCl all the way down to $\sim$-560 mV vs. Ag/AgCl. When the pH is lowered to 12 and the chloride concentration is increased to 0.4 M, as is the case with solution 3, the potential drops all the way down to -666 mV vs. Ag/AgCl.

By comparing OCP measurements from method B and CP plots from method A it can be found that some solutions have OCP developments that either dip under or end at potentials below the measured corrosion potential values from method A. These solutions cause big corrosion attacks on the surfaces of the submerged samples, see Table 6.7. Samples immersed in solution 5B and 19 display OCP developments that are below the corrosion potential measured in method A during the entire time of exposure. Solution 3 had potentials that dropped below the OCP from method A after approximately a week. A common denominator for all the corrosive solutions is that none of the potential developments go below the repassivation potentials measured through the CP curves. The CP measurements for solution 3, 4, 5B and 9 were performed during preliminary work and can be viewed in section D.1, Figure D.1.

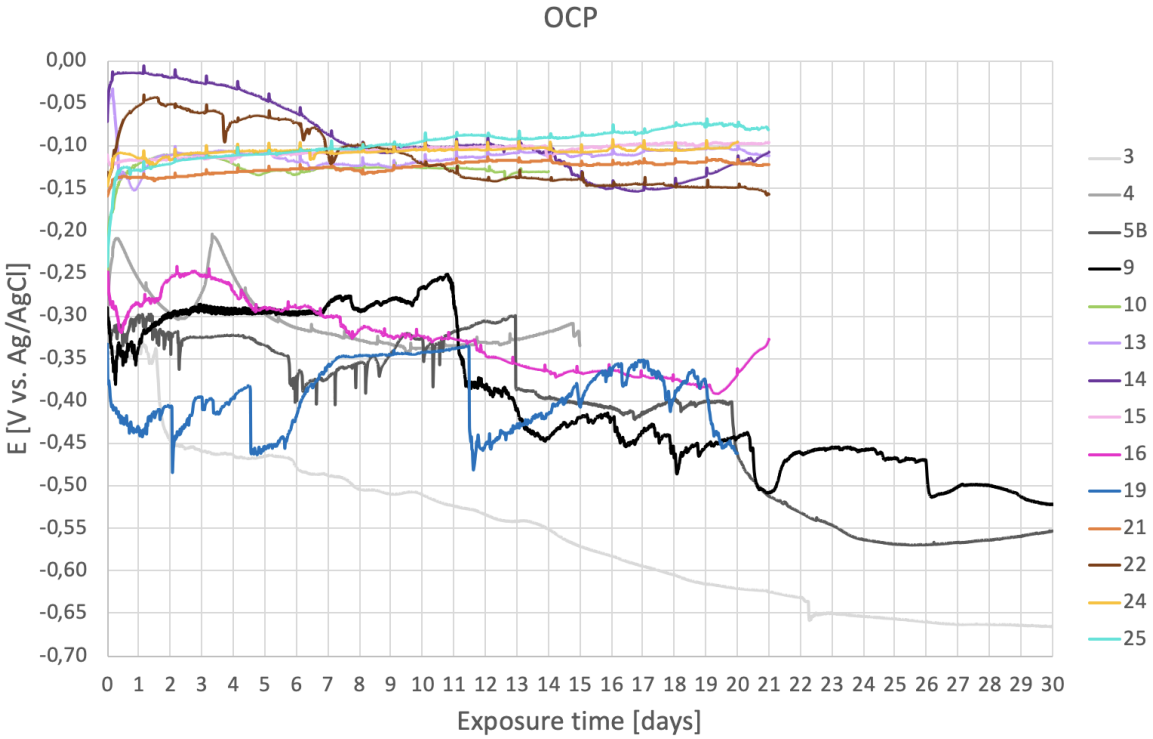

Figure 6.9: OCP development in different solutions.

In order to observe the effects of long-term exposure to oxygen free environments, solution 4 was run with nitrogen bubbling through the system in the setup displayed in Figure 5.5b. Throughout the exposure period, the test encountered two unforeseen problems that affected the results. After approximately one day, the nitrogen supply was cut off, allowing oxygen to enter the system. The aeration of the solution explains the first dip in potential that is visible in Figure 6.10a. It took approximately a day before the nitrogen was returned to the system. The return of nitrogen can be seen by the increase in potential.

After 14 days of exposure, the test was aborted prematurely due to evaporation of the electrolyte, see Figure 6.10b. When considering the potential development of solution 4, the potential begins to drop after three days of exposure, which is consistent with the reduced electrolyte volume following the evaporation. Despite the problems encountered, it is clear that the removal of oxygen initially causes an increase in potential when comparing solution 4 and 5B in Figure 6.9.

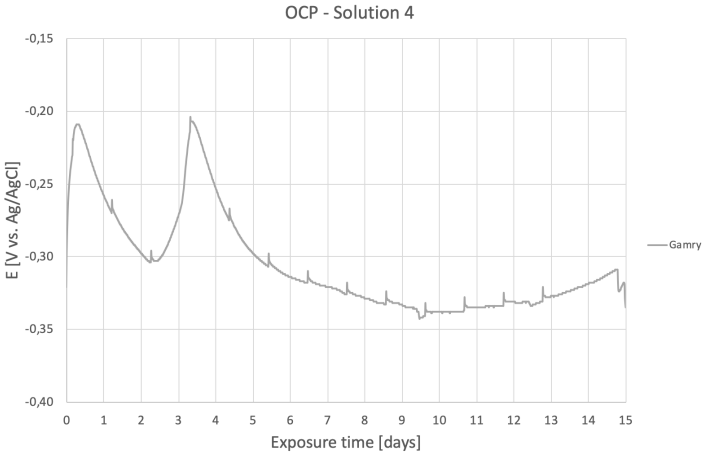

(a) OCP development for solution 4.

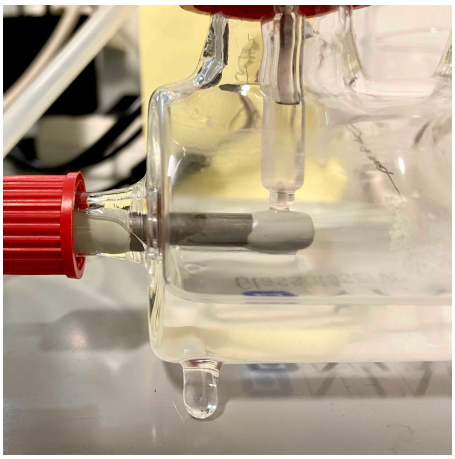

(b) The situation after two weeks of exposure

Figure 6.10: Solution 4.

To test the effect of the laboratory created passive layer, two solutions were chosen to run tests with samples that had the passive layer grinded away prior to testing. The two selected solutions were solution 15 and 25 and the potential developments are displayed in Figure 6.11 along with their oxide covered parallel. Both solutions have a chloride concentration of 0.01 M and solution 25 additionally contain 0.21 M of sulfate. The solutions display low corrosivity when samples with a pre-built passive layer are immersed. A common denominator for both oxide free samples is that they start at potentials below their pre-treated parallels, but end up at similar potentials.

In solution 15 there is a clear increase in potential during the first 5 days, indicating a building of an oxide layer. Even though the measurements display increasing noise after the initial 5 days, it is clear that the oxide layer stabilizes at potential values similar to the parallel sample with a pre-built oxide layer. In solution 25, the oxide layer appears to develop faster. Almost immediately, the potential development takes on a path similar to the pre-built oxide layer, residing only $\sim$10 mV below.

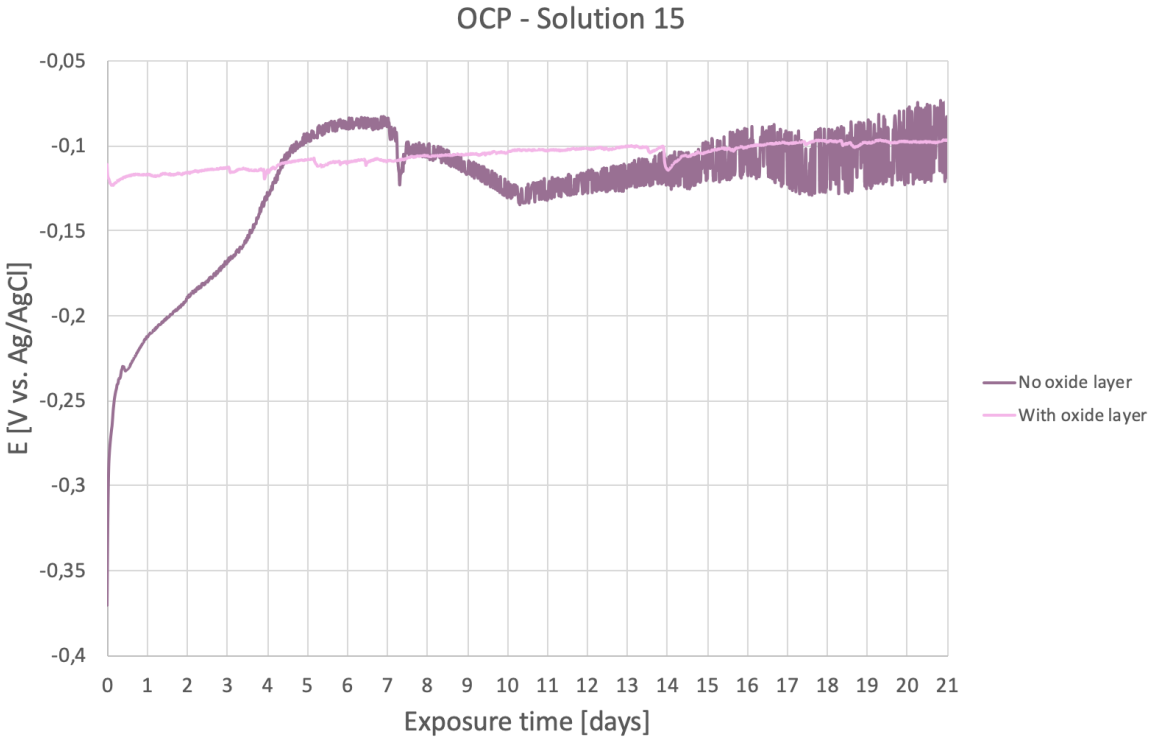

(a) Solution 15.

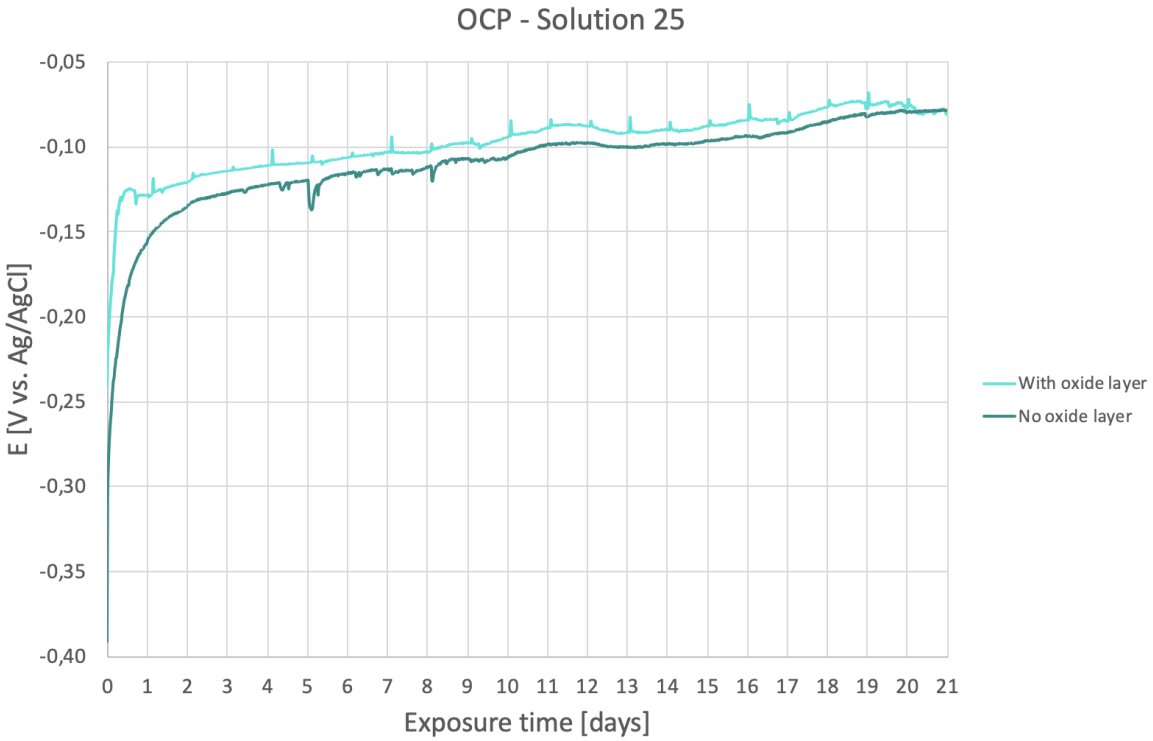

(b) Solution 25.

Figure 6.11: Tests run with and without a pre-made oxide layer.

LPR Measurements

From the LPR measurements, the corrosion current densities for the different solutions were calculated using the total exposure area and a Stern- Geary constant of 26 mV. The corresponding corrosion rates are given in section B.2 in Appendix B. One solution clearly stands out in Figure 6.12. Solution 3, which has a pH of 12 and a chloride concentration of 0.4 M, display an almost continuous increase in current density during the first 21 days of exposure. After three weeks of exposure the electrolyte had evaporated to such a degree that parts of the exposure area were above the solution. A reduction in area will cause a reduction in i_{corr}, which explains the drop in current density visible after 21 days. During the last week of exposure, the current density stabilizes. The high current densities reached corresponds to the large amounts of corrosion found on the sample immersed, displayed in Figure B.7 and in Table 6.7.

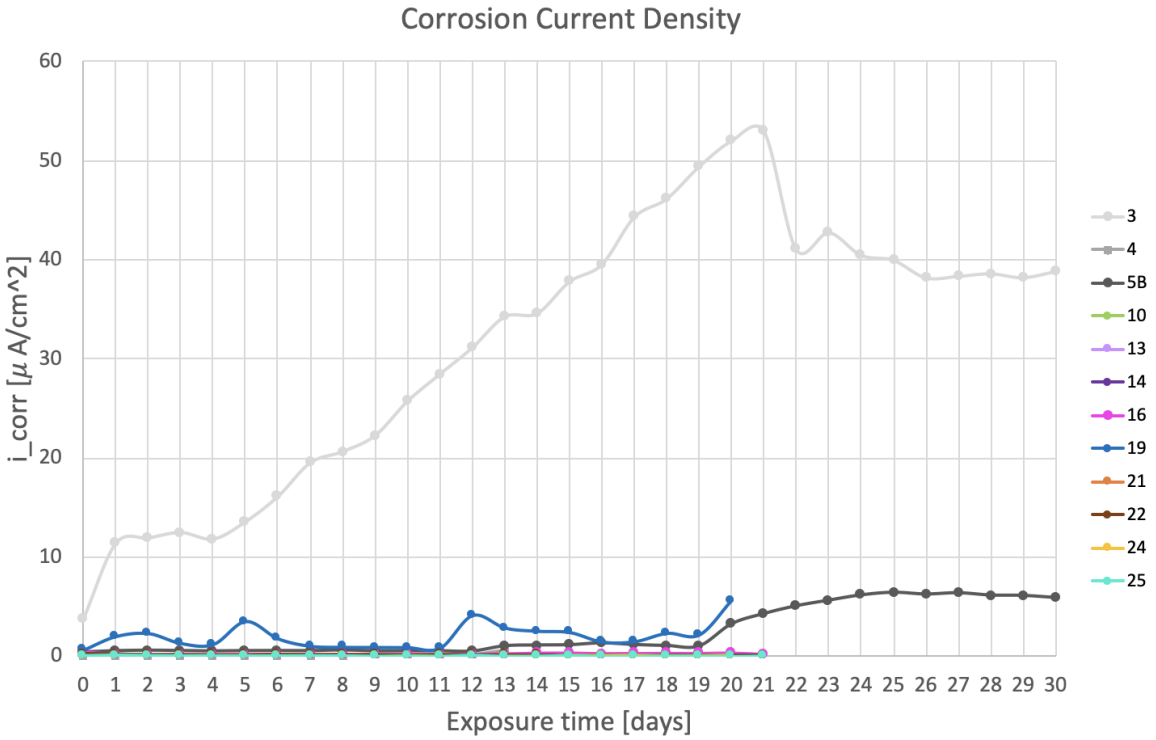

Figure 6.12: Corrosion current density for all solutions tested. Calculated from LPR measurements made once every 24 hours during the exposure time, using the total exposure area.

When considering the corrosion current density development, there is again a clear distinction between two groups in the solutions with a pH of 12.5, see Figure 6.13a. Solution 19, which has a chloride concentration of 0.1 M and a sulfate concentration

of 0.21 M, display relatively high and unstable values of i_{corr}, which coincides with the unstable OCP curve with generally low potential values displayed in Figure 6.9. Solution 5B, which has a chloride concentration of 0.1 M, is stable until approximately 19 days, when the corrosion current density rapidly increases. This corresponds to a sharp dip in OCP measurements after the same amount of time. Both samples mentioned display a high percentage of corroded surface area, see Table 6.7.

In Figure 6.13b the corrosion current density development for solutions with a pH of 13 is displayed. Even though a gap is visible between solution 16 and solutions 14 and 24, the i_{corr} values for all the solutions are still at relatively low values compared to the curves in Figure 6.13a. The i_{corr} values are in the same range as the the solutions displaying low corrosivity with a pH of 12.5. Although solution 16 resides within the lower potential ranges from OCP measurements, it displays here passive behavior similar to the other two solutions in Figure 6.13b. None of the samples with a pH of 13 display any visible signs of corrosion.

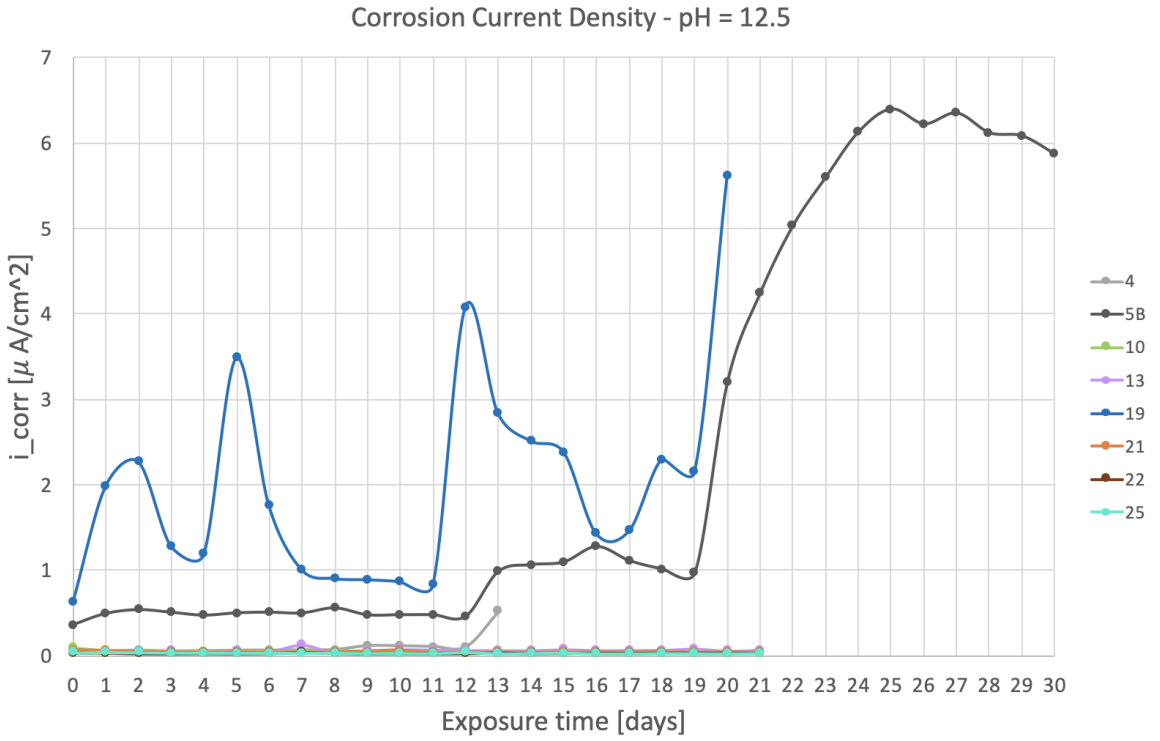

(a) pH = 12.5.

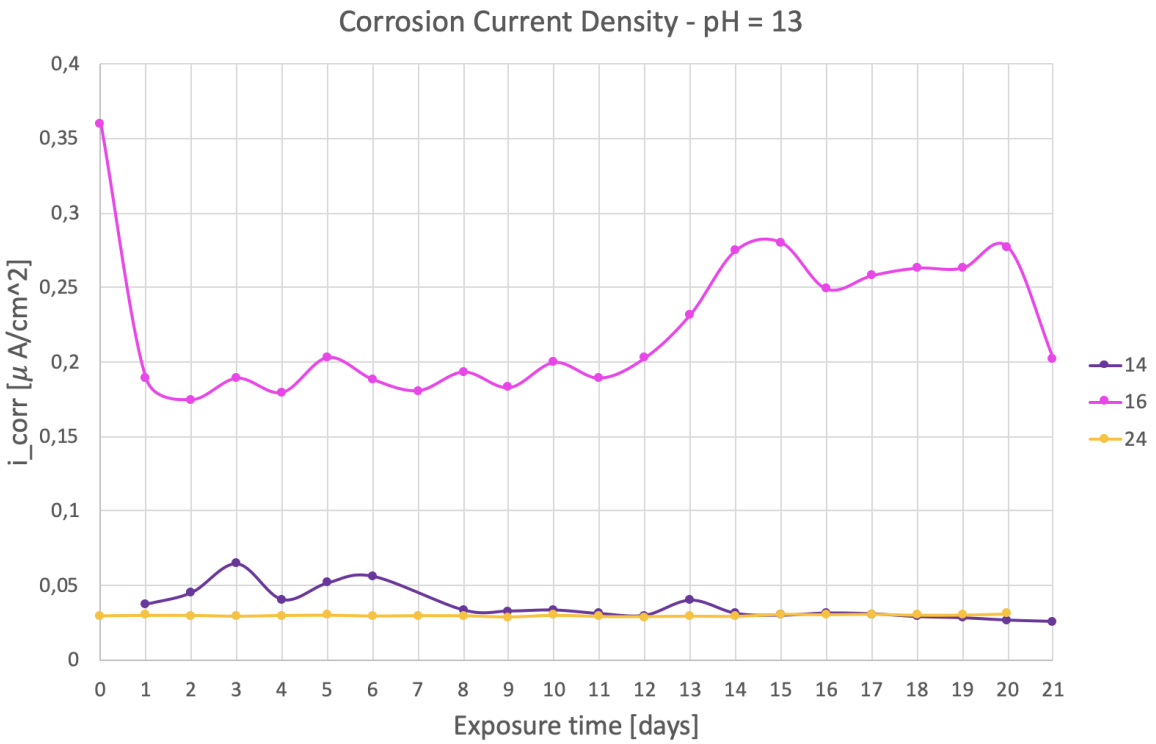

(b) pH = 13.

Figure 6.13: Corrosion current density for all solutions with a pH of 12.5 and 13. Calculated from LPR measurements using the total exposure area.

Potentiodynamic Scans

The potentiodynamic scans performed after ended OCP/LPR measurements have less distinctive groups compared to what the other types of measurements display, see Figure 6.14. However, it is the same corrosive solutions that occupy the lower ranges of potential values and the higher ranges of current densities. Solution 10-15 and 21-25 display passive behavior due to the high potentials and low current densities. The anodic branches have slopes approaching infinite values, $b_a \rightarrow \infty$, which indicates true passive states.

Solution 16, which previously have resided in the lower potential group form OCP measurements, but the passive regions from the LPR measurements, display here a slightly more corrosive behavior. It has a corrosion potential of approximately -700 mV vs. Ag/AgCl, which is in the same potential range as solution 5B. Still, solution 16 have current density values residing within the typical passive range of 0.1-1 μA/cm^2 and an anodic branch that bends until $b_a \rightarrow \infty$.

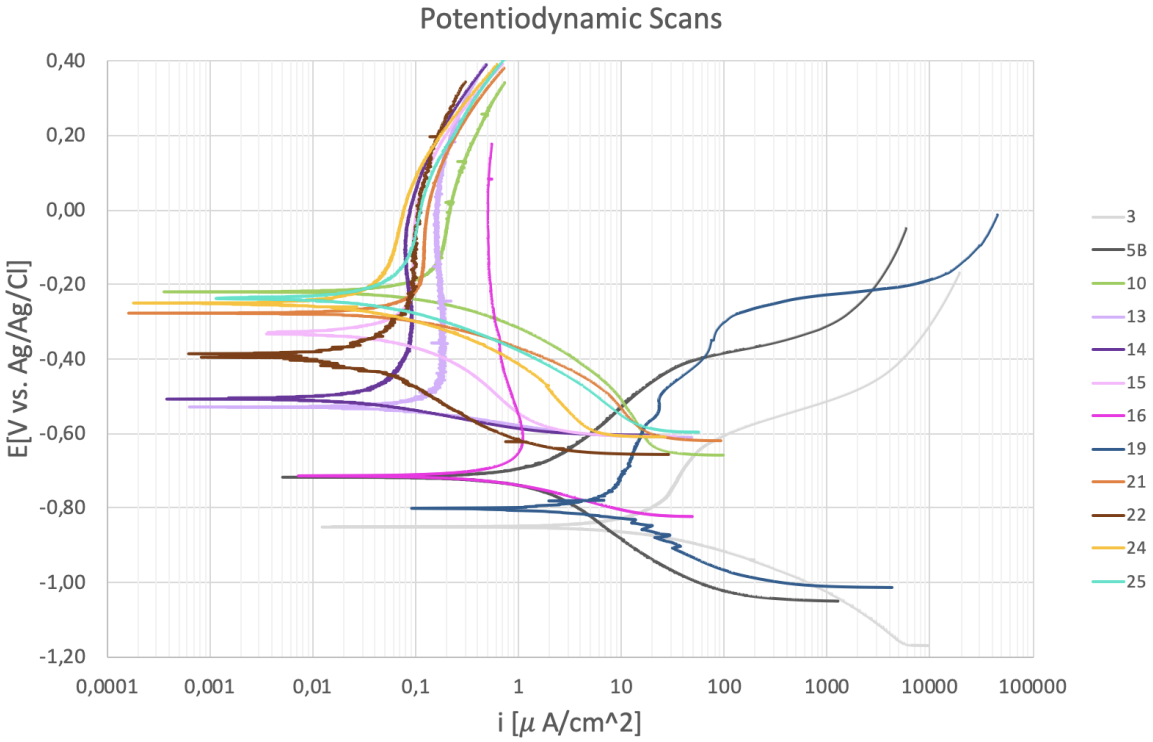

Figure 6.14: Potentiodynamic scans performed after ended OCP/LPR measurements for solutions in method B.

Initially, solution 3, 5B and 19 appear to go through a passivation polarization, indicated by the steep slopes of the anodic branch. As the potentials increase, the current densities rapidly increase, and the solutions enter a stage of activation polarization. Overall, solution 3, 5B and 19 appear to be in an active state of corrosion due to the combination of very low potentials and high current densities.

Corrosion current density, i_{corr}, values are calculated from R_P, which assumes both Tafel constants to be 120 mV/decade. From the potentiodynamic scans, both anodic and cathodic Tafel constants have been measured for solutions displaying corrosive tendencies and solutions residing in the lower potentials of passivity. These are presented in Table 6.6. Most anodic Tafel constants are a lot higher than the assumed value. The steep slopes correspond to the passivation polarization displayed in Figure 6.14. This indicates that the samples are passive, or as is the case with solution 3, 5B and 19, initially passive.

Table 6.6: Tafel constants measured from some of the potentiodynamic scans performed after ended OCP/LPR measurements. Plots are shown in Figure 6.14 in Appendix B.

Solution[1]	b_a [mV/decade]	b_c [mV/decade]
3	409.8	-80.4
5B	247	-172.7
13	$\sim \infty$	-39.1
14	$\sim \infty$	-47.1
16	$\sim \infty$	-65
19	415	-137

[1] Solution referred to according to Figure 5.8.

The absolute value of the cathodic Tafel constant, b_c, of solution 19 is quite close to the assumed value of 120 mV/decade. However, some of the cathodic Tafel constants appear to be closer to a cathodic Tafel slope of -40 mV/decade, which can be calculated assuming a composite transfer coefficient for reduction, α, of 1.5 [39]. A cathodic Tafel slope of -40 mV/decade will result in a Stern-Geary constant equal to -26 mV, using Equation 5.2.

Visual Inspections

After ended testing, all samples have been subjected to visual inspections. Images of the corroded surfaces are displayed in Appendix B, Figure B.7. The amount of surface area subjected to corrosion is measured and the results are displayed in Table 6.7. The table is sorted in order the from most to the least amount of corroded area after OCP/LPR measurements. From measurements it is clear that the solution displaying the most corrosion after OCP/LPR measurements are the ones containing the highest concentrations of chlorides.

Table 6.7: The percentage of the surface area subjected to corrosion.

Samples[1]	Percentage of Area Corroded [%]	
	After OCP/LPR	After OCP/LPR + Polarization
4[2]	90-95	x
3	50-55	95-100
5B	20-25	95-100
9	10-15	x
19	0-5	25-30
14	0-5	0-5
25	0	5-10
25[3]	0	x
15	0	0-5
15[3]	0	x
21	0	0-5
22	0	0
10	0	0
13	0	0
16	0	0
24	-	0

[1] Sample number refers to the solutions given in Figure 5.7.

[2] Errors in corroded surface area may be present due to complications during measurements.

[3] Sample had no oxide layer prior to testing.

Notes to Table 6.7:

- -: Only one sample tested, therefore sample has undergone both OCP/LPR and polarization measurements prior to visual inspections.
- x: Polarization measurements were not performed on sample.

In order to further inspect the surfaces, an optical microscope (OM) was used. The surface of the sample subjected to OCP/LPR measurements in solution 15 was examined more closely, see Figure 6.15. Initial inspections, without any magnification, does not reveal any corrosion damage. However, a 10X magnification reveal varying states of the oxide layer. In the middle of the exposure area, there are sections where the oxide appeared intact and sections with defects in the oxide layer. Along the edge of the exposure area, the oxide appear the most damaged showing larger areas lacking of oxides.

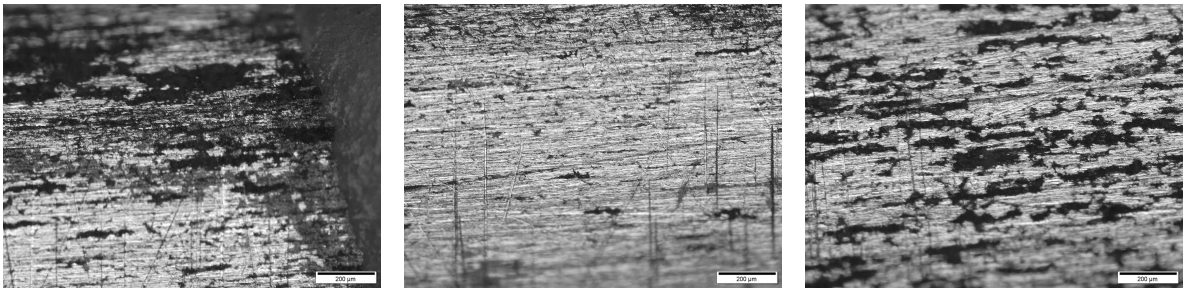

(a) Edge **(b)** Midsection **(c)** Midsection

Figure 6.15: OM imaging of solution 15.

Inspections performed with an optical microscope on the surface of the sample immersed in solution 10 and subjected to OCP/LPR measurements are displayed in Figure 6.16. Without any magnification, the sample display no signs of corrosion. When inspected more closely, the surface reveal major damage to the oxide layer.

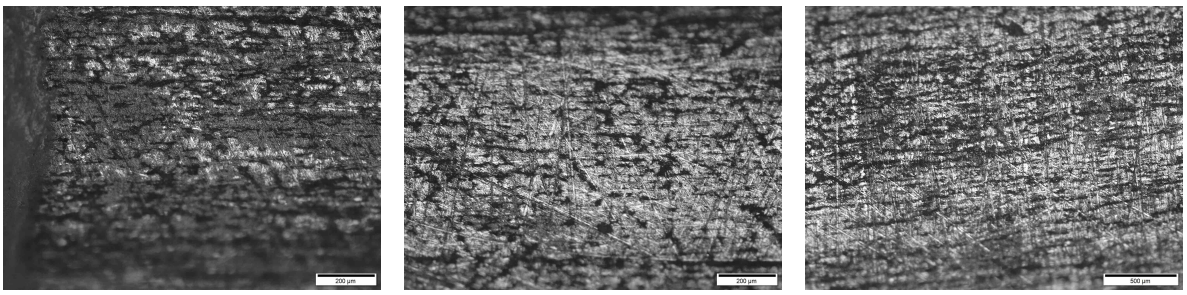

(a) Edge **(b)** Midsection **(c)** Midsection

Figure 6.16: OM imaging of solution 10.

After OCP/LPR measurements, the sample subjected to solution 9 had a large continuous corroded area. Within this area, the oxide layer appears to be completely dissolved, see Figure 6.17. When viewing the remaining surface area, the oxide appear unaffected by the exposure to the electrolyte, as can be seen by the lack of defects both along the edges and in the middle of the exposure area.

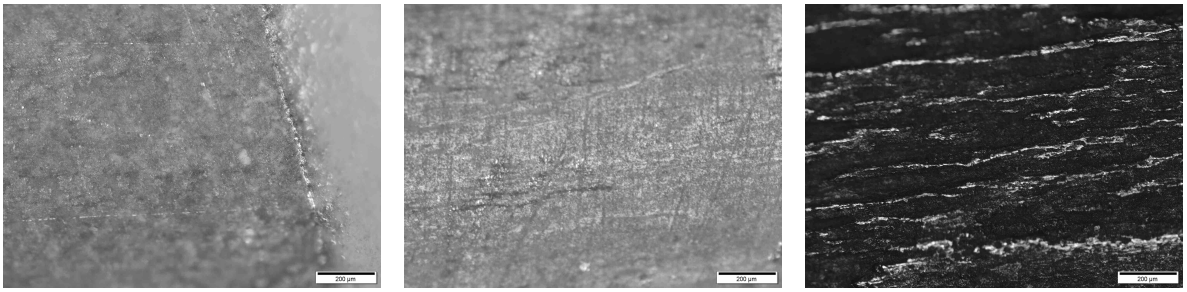

(a) Edge **(b)** Midsection **(c)** Corroded area

Figure 6.17: OM imaging of solution 9.

The rest of the results from the surface examinations using an optical microscope is given in section B.3 in Appendix B. Samples displayed there, show no signs of corrosion outside of what was visible to the naked eye. However, there are variations in the state of the oxide layer.

Summarized Findings from Method B

1. A clear distinction in potential ranges and i_{corr} is seen between solutions with a chloride concentration above and below 0.01 M. With a concentration $\leq$ 0.01 M, the solutions display high potentials, indicating passive behavior.
2. A chloride concentration $>$ 0.01 M results in solutions displaying corrosive behavior with samples subjected to corrosion attacks.
3. The removal of oxygen indicates a reduction in corrosivity.
4. Samples run without a pre-made oxide layer appear to form an oxide layer during their initial days of immersion in the test electrolyte. This was visualized by a rapid increase in potentials, until the potentials of the two parallels matched.
5. Samples displaying no visible corrosion, show varying states of the oxide layer when examined with an optical microscope.

Chapter 7

Discussion

7.1 Observations from the Bridge

One of the biggest takeaways from inspections performed on Herøysundet bridge, from preliminary testing and from the discussion made during the specialization project is that the source of the corrosion on the tensile wires stem from internal factors within the tendon ducts. This statement is based on the limited corrosion found on the reinforcement bars placed closer to the environment and the minimal corrosion found on the outside of the tendon ducts. Another potential cause of corrosion that was excluded was the use of seawater as mixing water for the grout. The low chloride concentrations measured by SINTEF [89, 90] in the dry grout lay grounds for this statement.

Factors emerging as important to the corrosion discovered were the presence of large voids, the state of the grout, high moisture contents and high ion contents. Tensile wires covered in firm grout displayed no corrosion, while areas subjected to voids or crumbled grout displayed corrosion attacks, shown in Appendix E. After inspections performed by Deka [82], large voids were discovered within the tendon ducts. Voids stretching over 1 meter in length were most likely the result of poor filling. The high moisture contents reported by SINTEF [90] could be the cause of a too high w/c-ratio, which is known to cause segregation and consequentially the formation of voids. Typical for high w/c-ratios is the presence of excess bleed water in voids. This could explain the corrosion attacks on the wires that show worse attacks along the bottom. A high w/c-ratio is most likely also the cause for the frost deteriorated grout found within the ducts.

Due to the size of the voids, it is likely they contained a surplus of oxygen which would contribute to intensify corrosion reactions. It is also a possibility that carbon dioxide

could be present within the large voids. This could then explain why parts of the wires exhibited general corrosion attacks, as carbonation lowers the pH enough to break down the passive layer on the steel.

SINTEF reported low concentrations of chlorides in the dry grout, 0.026-0.036 wt% (∼0.0075-0.01 M) [89], but higher values were found in the pore solutions of both moist and dry grout, 0.536-0.677 mmol/L (∼0.27-0.34 M) [90]. After experimental testing performed in this thesis, it has become apparent that corrosion can be initiated at chloride concentrations levels corresponding even to the lower levels discovered by SINTEF given a pH of 12.5 and 13. The documented presence of sulfur by SINTEF [90] could have contributed to worsening the pitting corrosion discovered on the wires.

7.2 Experimental Findings

7.2.1 Oxide Layer

During the preliminary work, several discoveries were made with regards to the oxide layer created on the surface of the samples. These findings led to conclusions being drawn regarding the time required for stabilization and the composition of the oxide layer. Figure D.8 showed that the oxide began to stabilize at a potential of -0.116 V vs. Ag/AgCl after six days of immersion, and the EDS analyses indicated that the oxide consisted of calcium carbonate, $CaCO_3$. The composition of the oxide was gathered from the results displayed in section D.3. SEM analyses also indicated that the calcium carbonate oxide had an uneven coverage. This could be seen both through imaging at high magnifications and through EDS results showing areas with high iron contents. A possible explanation could be uneven oxide thickness, which could lead to the electrons penetrating the substrate at thin areas. Another possible explanation for the high iron contents could be that the areas are covered with a natural passive layer that forms when steel reacts with oxygen in alkaline environments. As the iron dominating phases most likely consisted of FeO, a common oxide to form in alkaline solutions, both explanations seem plausible.

During the experimental program of the master thesis, new samples were immersed in the simulated concrete pore solution. It is apparent from potential measurements that an oxide has formed on the surface of the samples. As can be seen in Figure 6.1, the oxide layers reach a potential of approximately - 0.14 V vs. Ag/AgCl after seven days of immersion. This corresponds to results from preliminary work, as well as results from research by Poursaee et al. [94] and Sánchez et al. [19].

SEM images of the as-delivered samples were made in order to compare the natural oxide layer to the one created in the simulated pore solution. Imaging revealed the surface of the as-delivered samples to be covered with a naturally built oxide layer. The smoother appearing surface of the as-delivered samples displays large visual differences from the oxide created in the laboratory, see Figure 7.1. On the laboratory created oxide, the surface is covered with calcium carbonate, $CaCO_3$, micro particles. These particles are not visible under the same magnification on the surface of the as-delivered sample, which has an oxide layer that appear to provide an overall more even coverage.

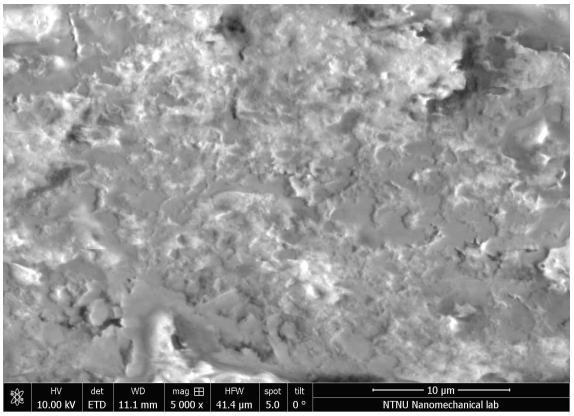

(a) As-delivered sample.

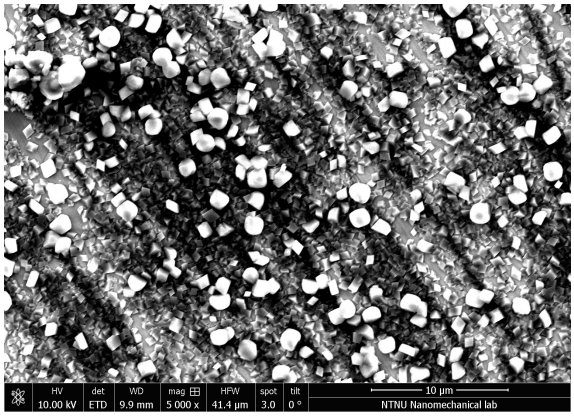

(b) Laboratory created oxide.

Figure 7.1: A comparison of the different oxide layers.

The difference in appearance might be the cause of several factors, such as mass transportation and diffusion rates. Firstly, the laboratory made oxide had one week to build, while the oxide immersed in grout could have continued to grow for years. Given the right conditions, particles will continue to grow and merge into one another through surface diffusion or volume diffusion, resulting in a fuller appearing layer. It is therefore possible to assume that the oxide layer on the as-delivered sample had an appearance similar to the laboratory made sample during its initial days covered in grout. Another influencing factor might be the availability of calcium. It is safe to assume that the growth of $CaCO_3$ is controlled by the diffusion of calcium in the surrounding medium. As calcium ions surrounding the steel gets used in the reactions creating the passive layer, more calcium ions present in the grout will be able to diffuse through the grout and into the pore solution, creating an endless supply. In the synthetic solution however, calcium surrounding the sample is more limited. As the calcium ions react, growth will slow down as less ions are available to diffuse towards the surface. Limited diffusion is also associated with rounder particles, which corresponds to the observations made on the laboratory created oxide layer.

Even though there is a visual difference between the oxide layers, the EDS analyses of

the as-delivered sample revealed the composition of the oxide layer to consist mainly of oxygen, calcium and carbon, which corresponds to the findings on the laboratory created oxide layer. By taking into account the atomic % of the elements found on both surfaces, it is highly probable that the layers consist of $CaCO_3$. As the iron content of the as-delivered sample is very low, it is plausible that $CaCO_3$ particles were the dominating oxides formed on surface, or that the oxide layer is thick enough that the electrons are not able to pass through to the substrate. Though low in %, there are trace elements of aluminum, magnesium, silicon, phosphate and sulfur present on the surface. These are likely present in the form of oxides which have developed from elements present in the steel or from trace elements found within the grout.

7.2.2 Method A

Simulating real conditions in a laboratory setting, with regards to corrosion testing of steel in concrete, can prove challenging. As pointed out by Angst et a. [5], among others, there are certain conditions that does not occur both on site and in the laboratory. In addition, a lot of previous research on the subject, see Chapter 4, is based on examining one critical factor at a time, and does not evaluate how different factors come into play together. In method A, CP measurements following ASTM G61 provide the grounds for testing. The ASTM G61 is developed to examine pitting and repassivation potentials on stainless steels and Ni-alloys. As the tensile wires are covered with an oxide layer in their passive condition, the method can be used to document E_{pit} and E_{rep} for the wires. These tests can also be used for giving an indication of what circumstances will make samples corrode. However, the test method has a short exposure time and run using high applied currents. Due to this, the tests usually provide lower threshold values for corrosion. Compared to long-term OCP/LPR measurements, the ASTM G61 provide high values for both pitting potentials and current densities. This might be a result of the high scanning rates (600 mV/t), that potentially are too high to reach initiation or to obtain an equilibrium. This being said, the ASTM G61 tests are a fast and simple way of testing and provide threshold values that can give an indication of when solutions turn corrosive.

Following the test program given in Figure 5.7b, the CP curves were measured for all given solutions. As can be seen from Figure 6.5, there was a clear distinction between corrosive and non-corrosive solutions. The large negative hysteresis loops correspond to a greater difficulty in restoring passivity, as it led to corrosion attacks on the surface of the samples, see Figure A.3. All corrosive solutions had a chloride concentration $\geq$ 0.0025 M. According to the 2020 SINTEF analyses [89, 90], the chloride concentration measured in the dry grout was at 0.026-0.037 %, which corresponds to a molarity

of 0.0075-0.01 M. This entails that the chloride concentration found on cite were high enough to initiate corrosion, given the right pH values. SINTEF also reported a chloride concentration of 0.27 to 0.34 M in the pore solution extracted from dry and moist grout samples, respectively [90]. These values are way above the critical chloride concentration of 0.0025 M, indicated from the ASTM G61 standardized CP tests. From visual inspections it was clear that the increase in chloride concentration led to an increase in corroded surface area as shown in Table 6.4. A general trend in the CP curves, which corresponds to the research by Moser et al. [3], is that an increase in concentration also corresponds to an increase in current densities reached and a decrease in pitting potentials.

The majority of samples tested were exposed to solutions with a pH of 12.5. This was determined following results from tests performed during the specialization project. Increasing pH levels require higher chloride ion levels in order for corrosion to occur, and this thesis was aimed to focus on corrosion in the presence of low chloride contents. At a pH of 12.5, corrosion was visible on samples with chloride concentrations as low as 0.0025 M. When examining the path of the reversed scan of the corrosive solutions in Figure 6.6, it was clear that the the solutions exhibit similar increases in current density as the potential decreases. This signifies that the samples continued in a state of pitting initiation and propagation, which can explain the amount of corrosion found. As the repassivation potential was around 0.5 V below OCP for all corrosive solutions, the corrosion continued to propagate throughout the test.

Solution 15, which had a chloride concentration of 0.01 M and was exposed to oxygen, was the solution with only chlorides present and a pH of 12.5 that displayed the largest amount of corrosion. It was also the solution that reached the highest current densities during its reversed scan, which signifies high corrosivity. The removal of oxygen from the solution, as was the case with solution 20, made the solution less aggressive. This was indicated by a lowering of current densities, during both the forward and reversed scan, and by an increase of OCP and E_{pit}. Research performed by M. Raupach in 1996 [24] noted that high cathodic reaction rates could occur in the early states of removal of oxygen, but a long-term removal would lower the potential and cause negligible corrosion rates. This corresponds to the literature presented in Subsection 2.2.2. As the CP measurements in method A were made over only hours, it is possible that the initial stages of oxygen removal is applicable to solution 20. If so, it could explain the increase in current density during the decrease in potential and the corrosion attacks present on the surface. However, the sample in the aerated solution displayed an approximately twice as large corroded area compared to the sample in the deaerated solution, building on the argument of reduced corrosivity.

Somewhat unexpected is the amount of corrosion discovered on the sample immersed in solution 22, with a chloride content of 0.0075 M. Compared to the samples subjected to solution 15 and 21, with chloride concentrations of 0.01 and 0.005, respectively, the corroded area was a quarter of their size. As the chloride concentration of solution 22 should entail a corroded area between that of solution 15 and 21, it is possible that there was an error during mixing, either with respect to the measurement of NaCl or the pH level. Solution 22 reached current densities similar to that of solution 23, which had a chloride content of 0.0025 M. From the results discovered during the specialization project, see Figure D.1 in section D.1, an increase in pH led to a shift of the curve to lower current densities. This corresponds to the observations made of solution 22. As E_{pit} has not increased compared to solution 15, an error in pH is more likely than an error regarding the chloride concentration. However, as only one sample was tested in each solution, the small differences between the solutions may be due to chance and minor differences in the oxide layer. If each solution were run with more samples, an average would present more accurate results.

Solutions exposed to electrolytes containing sulfates displayed three very different CP curves, as shown in Figure 6.8. The lack of corrosion found on the sample immersed in solution 18 is as expected as the pH was 13.5, and the low corrosivity was reflected in the positive hysteresis loop. As the pH was lowered to 12.5, the sample in solution 17 displayed metastable pitting during the passive state of the forward scan. The pitting potential was reached above typical passive current density levels, which can explain the corrosion attack found on the sample, displayed in Figure A.3. An addition of chloride ions given to solution 19 increased the corrosivity drastically, as can be seen from the large negative hysteresis loop that reaches high current densities and from the repassivation potential at 0.4 V below OCP. A common denominator for all magnesium sulfate containing solutions is that the solutions separated. By the end of the tests, sulfates were observed along the bottom of the test container, displayed for solution 19 in Figure A.2c. This may have affected the composition or the pH of the solutions. In future tests, the solutions should be filtered, and pH should be measured before testing is performed.

In Figure 7.2, the effect of different sources of sulfates are examined. Solution 7, 8 and 9 were given additions of sodium sulfate (Na_2SO_4), while 18, 19 and 20 were given additions of magnesium sulfate ($MgSO_4$). Both solution 7 and 18 have a pH of 12.5, solution 8 and 19 have a pH of 13.5 and solution 9 and 20 have a pH of 12.5 and an additional chloride concentration of 0.1 M. According to research by Xu et al. [2] and Dehwah et al. [57], different sources of sulfates result in varying corrosion rates. They discovered that magnesium sulfate made the electrolytes more corrosive than sodium sulfate. These findings correspond to the observations made during this thesis. With

a pH of 12.5 and no chlorides present, solution 18 displayed more corrosive behavior than its sodium sulfate containing counterpart. When the combination of sulfate and chloride was present, it is evident from the increased current densities reached and the enlarged negative hysteresis loop that magnesium sulfate created a more aggressive solution. However, a contradiction to the theory of increased corrosivity, is the change of the passive path towards lower current densities and the increase in OCP. The results of the CP might be affected by the separation of the solution, as discussed above. This being said, the sample immersed in solution 19 displayed worse corrosion attacks compared to solution 9. Solution 9 caused a corrosion attack on the sample dominated by several semi-large corrosion initiations, imaged in Figure D.3 in section D.1. The solution immersed in solution 19 displayed many small pit initiations, which correlates to the rapid increase in current density displayed after E_{pit} has been reached.

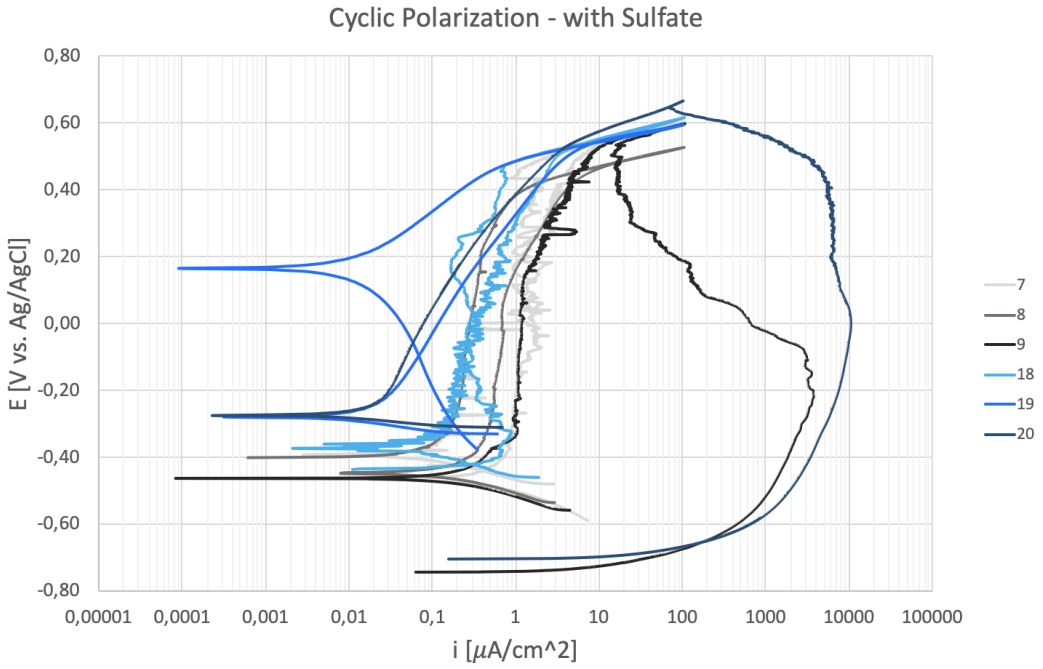

Figure 7.2: CP plots of solutions containing sulfates. Solution 7-9 were measured during the specialization project the fall of 2021.

When considering the combined effect of sulfates and chloride ions the results vary depending on the source of the sulfate ions. In Figure 7.3, the CP plots can be seen for solution 5, with a chloride concentration of 0.1 M, solution 9, with a chloride concentration of 0.1 M and a sulfate concentration stemming from sodium sulfate of 0.21 M, and solution 19, with a chloride concentration of 0.1 M and a sulfate concentration stemming from magnesium sulfate of 0.21 M. According to literature and previous research, as described in Subsection 2.2.5, the addition of sulfates can increase corrosion rates

when combined with chlorides. With regards to E_{pit}, sulfates appear to have increased the potential, indicating a reduction of corrosivity. A presence of sodium sulfate lowered the OCP and presented a forward scan at higher current densities, both of which indicate increased corrosivity. The solution with magnesium sulfate show lower current densities during the forward scan compared to the sulfate free solution, indicating that the solution is less aggressive. However, all solutions display forward scans within the range of typical passive current densities. Solution 19 display a reversed scan following a similar path to that of solution 5, both reaching higher current densities than solution 9. Both sulfate containing solutions have low E_{rep} which entails difficulties in restoring passivation after pitting was initiated. From visual inspections of the samples, given in Table 6.4 and D.2, it is clear that the solution with magnesium sulfate was the most corrosive, given an overall larger corrosion attack on the surface. Immersion in solution 9, however, resulted in less corrosion on the surface compared to the sulfate free solution. This could entail that the high current densities reached during the reversed scan and the low E_{rep} are the most determining factors of corrosivity from the CP plots. The effect of sulfates on the corrosivity of the solutions appear to be dependent on the source of sulfate ions.

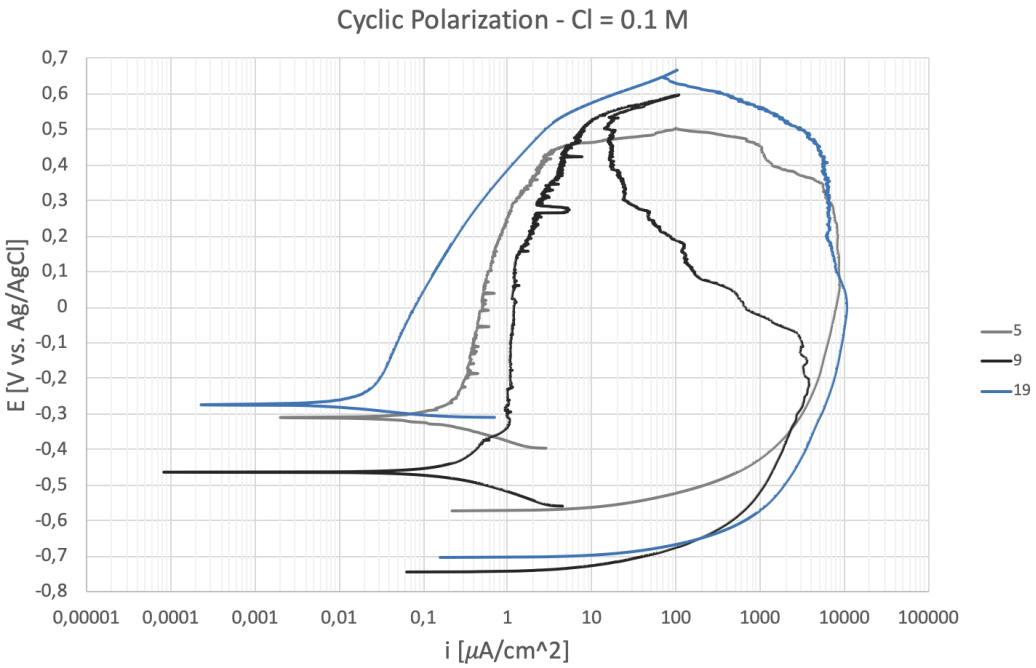

Figure 7.3: CP plots of solutions with a chloride concentration of 0.1 M. Solution 5 and 9 were measured during the specialization project the fall of 2021.

7.2.3 Method B

As previously mentioned, long-term exposure tests provide more accurate indications of the corrosivity of a solution as they run under conditions closer to the true exposure conditions. During method B, OCP measurements were made over the course of two to four weeks. Compared to the CP test run according to ASTM G61, the long-term OCP measurements provided less conservative chloride threshold values. From the OCP measurements displayed in Figure 6.9 a clear distinction was visible between the corrosive and non-corrosive solutions. In the ASTM G61 tests run with a pH of 12.5, the change in corrosivity was visible in the curves as the chloride concentrations reached 0.0025 M. From OCP measurements, the drop in potential indicating corrosion was not visible until the concentration exceeded 0.01 M for the same pH level. This corresponds to chloride threshold levels measured by Ioan Pepenar [100]. A threshold level of 0.01 M is within the upper range of the chloride levels discovered in the grout analysis performed by SINTEF [89], but is still way below the chloride levels of 0.27-0.34 M measured in the pore solution [90]. The corrosive solutions display potential developments that never go below the repassivation potential measured through CP curves. This could entail that corrosion continued until the end of the exposure and would explain the amount of corrosion found on samples immersed in solution 3, 5B, 9 and 19.

The only test run with chloride concentrations above what was measured by SINTEF in the pore solution is solution 3, which had a chloride concentration of 0.4 M in addition to a pH of 12. It displayed a OCP development with very low potentials that continued to drop until the exposure period was finished. Visual inspections performed after testing, indicated large corrosion attacks, both general and pitting. The CP curve for solution 3 were measured according to ASTM G61 during the specialization project and is displayed in Figure D.1. A small hysteresis loop placed at low potentials and with an undefined pitting potential correspond to the general corrosion visible on the samples used in both CP and OCP measurements.

When considering the chloride/pH combinations, most solutions follow potential developments at expected values. The exception is solution 16, which, with a chloride concentration of 0.01 and a pH of 13, displayed low potentials and was located among the corrosive solutions. This is not as expected as solution 15, which had a chloride concentration of 0.01 and a pH of 12.5, resided within the upper non-corrosive potential group. Based on literature [16] and research by Li et al. [6], the resistance towards pitting should increase with increasing pH. Another inconsistency regarding the low potential values of solution 16 was the lack of corrosion on the exposure area of the immersed sample. However, under closer inspection, the sample does exhibit signs of

corrosion on the upper unpainted area that was connected to the potentiostat. As each solution was only tested once, minor deviations from the intended mixture can be a possibility. Another potential influencing factor is the addition of KOH added to all solutions with a pH of 13 in order to obtain the high pH level. None of the other solutions with a pH of 13 display low potential, however, solution 16 had the highest chloride level of them.

As shown in Figure 6.10a, the test run without oxygen provided an indication of an initial increase in potential compared to the aerated counterpart (5B), even though the test experienced several problems. In comparison to the aerated solution, solution 4 displayed an initial increase in potential up to values reaching approximately 0.2 V vs. Ag/AgCl above solution 5B. As the nitrogen was reported cut off after two days of exposure, there is a corresponding dip in potential dropping to values similar to the aerated solution. As the nitrogen return, the potential increases again to values similar to the initial potential. A new reduction in potential appears, most likely due to the evaporation of the electrolyte as imaged in Figure 6.10b. Even through the difficulties, it is visible that at times when the oxygen was removed, the solution became less aggressive.

The two solutions with magnesium sulfate and sodium chloride contents, 19 and 25, yielded very different potential results. In Figure 6.9, Solution 19, which had a sulfate content of 0.21 M and a chloride content of 0.1 M, resided within the lower potential group and displayed a turbulent potential development. The solution displayed corrosive tendencies and caused corrosion attacks on the sample immersed. Solution 25, with a sulfate content of 0.21 M and a chloride content of 0.01 M, did not inflict any corrosion attacks on the sample immersed. This was as expected considering the high stable potentials displayed in Figure 6.9. A chloride concentration of 0.01 M, given to solution 15, was not able to initiate corrosion on its own, while a chloride content of 0.1 M in solution 5B proved to make the solution corrosive. Knowing this, it is possible to assume that sulfates only worsen corrosion attacks that already have presented themselves and are not able to participate in the initiation of corrosion.

Similar to the magnesium sulfate containing solutions tested according to method A, the sulfate containing solutions used in method B separated during the exposure period, imaged in Figure B.6. This resulted in an opaque and highly concentrated sulfate solution lining the bottom of the test container. As sulfates are known to worsen corrosion attack when combined with sulfates [56–58], a bigger difference was expected when comparing potential developments of solution 19 and 25 to the solutions with similar chloride concentrations. However, if the sulfates were not actively participating, due to the separation, it could explain the lack of major differences. From Figure 7.4 it is

visible that there is a potential difference during the first 6 days of exposure. As the immersion continues, the potential developments become more similar. Worth noting is that solution 19 caused a smaller percentage of corroded surface area compared to its sulfate free parallel. This could entail reduced corrosivity, but the most probable explanation is the shorter immersion time. As the sample in solution 5B was kept for an additional week, it is clear that the potential continued to drop during the last week, causing further corrosion. It is possible that the initial difference is caused by the magnesium sulfate, and as the ions settle at the bottom of the beaker, they stop affecting the corrosion and only chloride ions contribute to the corrosivity. During long-term exposure tests, a magnetic stirrer may prevent the separation and yield more distinctions in potential developments.

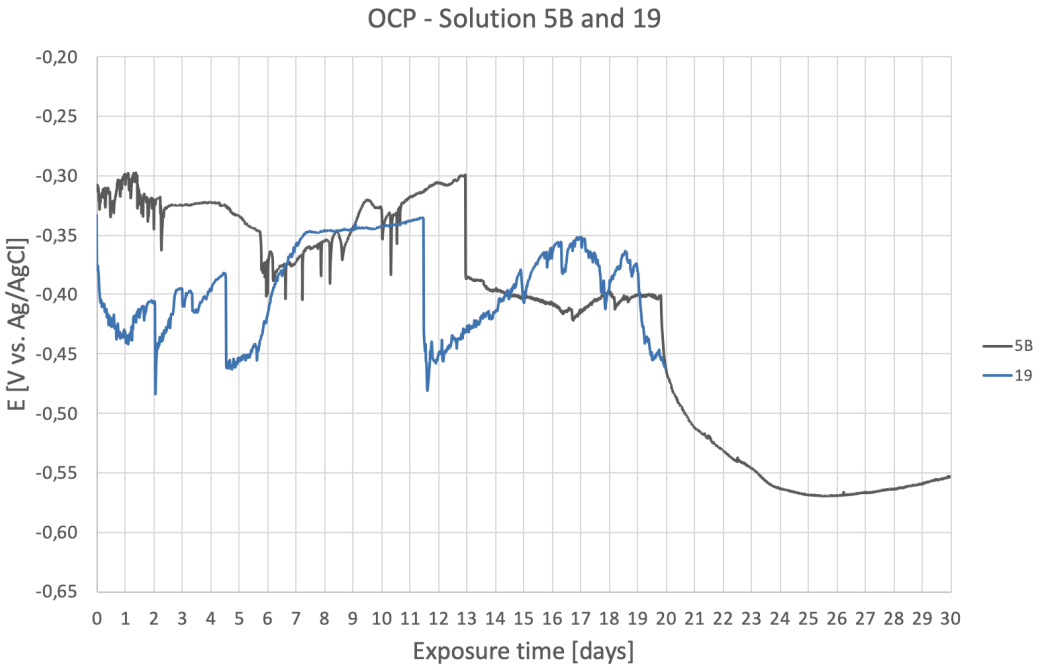

Figure 7.4: OCP developments in solution 5B and 19.

Both tests run with samples that had the passive layers grinded away prior to testing showed potential developments in Figure 6.11 that indicated a new passive layer developed within a week of exposure. As the solutions chosen previously yielded results of low corrosivity when samples with pre-built passive layers were submerged, it is as expected that the samples were able to passivate. From these tests it is found that a chloride concentrations of 0.01 M is not sufficient to cause corrosion before the samples passivate. This was confirmed by a lack of corrosion on the test samples after ended testing. Larger differences might appear if tests were run at higher chloride concentrations.

In between OCP measurements, LPR measurements were made once every 24 hours. The corrosion current densities were then calculated assuming a Stearn-Geary constant of 26 mV. Important to note is that the original exposure area was used for the calculations of all samples. For non-corroded samples, this will not result in any errors of current density. However, for corroded samples, the effective anodic area would have changed. As solution 3, 5B and 19 caused corrosion on the immersed samples, the effective anodic area would have minimized during the exposure period. A reduction in area would lead to an increase in current density, as $i = I/A$ [39]. Because of this, the current density values calculated towards the end of the exposure period for solution 3, 5B and 19 displayed in Figure 6.12 and 6.13a might be somewhat lower than what they actually were.

This being menitioned, there are clear correlations between the OCP and LPR measurements. When inspecting the corrosion current density development of solution 5B, it is evident that the first notable increase after 13 days of exposure corresponds to a dip in potential from the OCP measurements, see Figure 7.5a. As the current density rapidly increases at day 20, the potential drops. Similar correlations are visible in solution 19, where peaks in the current density corresponds to dips in the potentials, and vice versa, as displayed in Figure 7.5b.

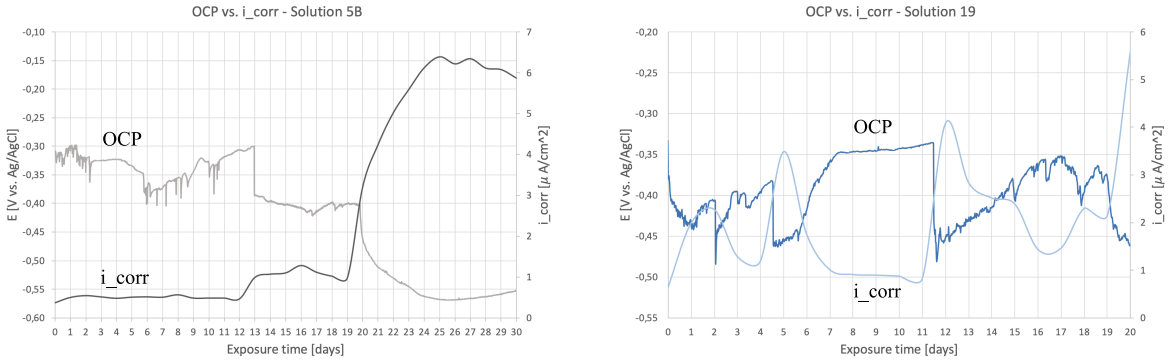

(a) Solution 5B **(b)** Solution 19

Figure 7.5: OCP vs. i_{corr}.

The final measurements performed during method B were the potentiodynamic scans made at the end of the exposure period. In Figure 6.14 distinctive groups of corrosive and non-corrosive solutions are slightly blurred by the position of the curve belonging to solution 16. The low chloride containing solutions that have previously exhibited non-corrosive behavior still occupy high potentials and low current densities. Their potentiodynamic curves display anodic branches with slopes that approaches infinite values, which confirms passive behavior. As previously mentioned, solution 16 displayed a potential development similar to that of a corrosive solution. The LPR measurements,

however, indicate that the solution is non-corrosive. A corrosion current density between 0.175 and 0.36 μA/cm^2 is below 1 μA/cm^2, which is typically marked as the upper value of passive current densities as noted in Subsection 2.2.4. Even though solution 16 deviates from the clearly passive solution, it is still within the passive ranges of the current density and display the characteristic steep anodic branch. A potential reason for the low i_{corr} values calculated from LPR measurements and lack of corrosion on the specimen in solution 16 could be that the current density values in the potentiodynamic scan never surpasses the passive region.

Within the lower potentials and higher current densities reside the same corrosive solutions, 3, 5B and 19. A common denominator for all three solutions, is that they all exhibit an initial passivation polarization as indicated by the steep initial anodic branch. However, as the the current densities reach values between 50-100 μA/cm^2, the increase in potential subsides and they enter stages of activation polarization indicated by the rapid increases in current density. These observations coincides with the visual inspections that indicated all three samples had a large increase in corroded surface area after polarization, see Table 6.7.

The anodic Tafel slopes measured from the potentiodynamic scans differ from literature. The high values of b_a are most likely caused by the initial passivation polarization that the solutions exhibit. By measuring the slope of the activation polarization, the Tafel constants are all below the 90 mV/decade. The total slope, as shown in Figure 7.6, give a b_a values closer to 120 mv/decade, which was the value used for the calculations of corrosion current density.

After ended testing, visual inspections using an optical microscope led to discoveries of defects in the oxide layers of samples that displayed little to no corrosion. The different states of the oxide layer may be the result of a too short immersion time during creation. Confirming this theory is the state of the oxide layer on the sample immersed in solution 10, displayed in Figure 6.16. The solution had no chloride ions present, making the solution non-corrosive, in theory. Immersion should therefore have caused a further passivation of the sample, not a breakdown of the passive layer. Solution 15, which have a chloride concentration of 0.01 M have shown passive behavior during all tests performed according to method B. Observations using the microscope show damages to the oxide layer but no corrosion initiation. This observation emphasizes the theory that the chloride threshold level is above 0.01 M.

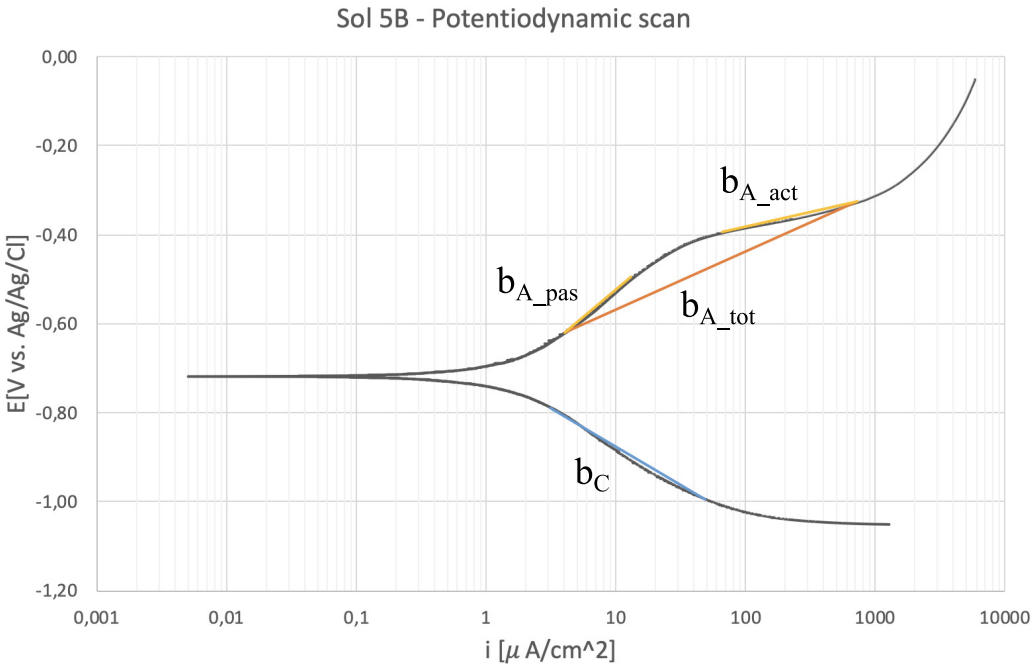

Figure 7.6: Illustration of the average slope of the anodic branch.

7.3 New Test Methods

Inside the tendon ducts, the wires can be exposed to several conditions. From the images gathered from the bridge in Herøysundet, see Appendix E, it is visible that the wires are partially surrounded by firm grout, while other sections are exposed to crumbled grout, moisture or air. These different exposure conditions have resulted in different types and different amounts of corrosion. In order to get a more correct understanding of the processes that takes place inside the ducts, a new test method needs to be developed that takes into consideration all the exposure conditions inside.

The test methods used for experimental testing during this thesis base themselves on the tensile wires being subjected to only concrete pore solutions. Research by Dong et al. [62] and Castel et al. [61, 101], as described in Chapter 4, use tests that take into account galvanic elements. Dong et al. [62] look at how corrosion proceeds when parts of the sample is covered in non-corrosive pore solutions, while other parts are subjected to chloride contaminated pore solutions. Castel et al. [61, 101] use samples cast into concrete to test the effect of galvanic couplings between carbonated and uncarbonated concrete.

In order to create a more realistic testing method, elements from all these tests should to be taken into account. In addition, there should be a part of the test that equip

atmospheric corrosion tests to account for the situation in empty voids. New test methods should be developed to measure rate determining conditions and how these affect one another. In addition, the test should have a way of controlling the diffusion rates of factors such as oxygen and aggressive ions.

Chapter 8

Conclusions

This study has consisted of drawing conclusions from observations and inspections performed on Herøysundet bridge. These have been followed by experimental testing in order to determine the consequences of the findings made during the inspections and to determine the causes of corrosion. From preliminary work and inspections performed on Herøysundet bridge, it is evident that the source of corrosion on the tensile wires stems from within the tendon ducts. Further, the presence of grout was determined to be a critical factor influencing whether or not corrosion presented itself. In areas containing large voids and/or crumbled grout, the tensile wires displayed large corrosion attacks. Sulfate and chloride levels measured in both grout and pore water was found through experimental testing to be above levels that initiate corrosion.

In this study, test samples used were grinded before an oxide layer was created by exposure to a simulated pore solution. The process created a oxide layer consisting of $CaCO_3$ that, through observations with a SEM, was different in appearance from, though similar in composition to the oxide layer present on the samples extracted from the bridge. This leads to the conclusion that the samples tested provide good representation of the tensile wires in the reinforcement of the bridge.

Cyclic polarization measurements following ASTM G61 were used to determine how ion contents, pH levels and the presence of oxygen affected corrosion of steel immersed in simulated pore solutions. Measurements lead to the following conclusions:

- Corrosion is initiated in solutions with a chloride concentration ≥ 0.0025M given a pH of 12.5. Increasing chloride levels lead to increasing corrosivity, as shown through decreasing E_{pit} and increasing anodic current densities reached. The increased corrosivity is also visible through increased percentage of corroded area.

- Removal of oxygen makes the solution less aggressive, as seen from an increase in E_{pit} and OCP, and from a shift of the curve towards lower current densities.
- A sole presence of magnesium sulfates is able to cause a minor corrosion attack when the pH = 12.5, but not sufficient to cause corrosion at pH = 13.
- When sulfate ions from magnesium sulfate are combined with chlorides, the solution becomes more aggressive than when chlorides ions are present alone. The increased corrosivity can be seen through larger corrosion attacks on immersed samples.
- The source of sulfate ions has an effect on the corrosivity. Magnesium sulfate containing solutions are able to cause corrosion under conditions that the sodium sulfate containing solutions are not.

Long-term tests were performed in order to investigate potential development under true exposure conditions. Tests were run with varying exposure time in saturated $Ca(OH)_2$ solutions with varying concentrations of Cl^- and SO_4^{2-} and varying pH levels, measuring OCP and LPR followed in most cases by potentiodynamic scans. Following conclusion can be drawn:

- For corrosion to occur, the chloride concentration have to exceed 0.01 M in solutions with pH = 12.5. This was confirmed by all tests and visual observations.
- A removal of oxygen gives indications of reduced corrosivity from increased potentials and decreases in current densities.
- The combination of sulfate and chloride ions appear to increase corrosivity during the initial days of exposure in solutions where the chloride concentration was high enough to cause corrosion on its own. The lack of major differences in potential developments further out in the exposure period in chloride containing solutions with and without sulfates present can be explained by the separation of the solutions.
- A pH level of 12 combined with chloride concentration of 0.4 leads makes the solution highly aggressive and leads to general corrosion on the immersed steel. Therefore the pH level should be kept $\geq$ 12.5 when combined with high chloride contents in order to avoid general corrosion attacks.

As the ASTM G61 is known to provide more conservative threshold values due to extreme test conditions, the long-term tests provide more realistic results. Due to this, this thesis concludes that the chloride threshold concentration is above 0.01 M.

When taking into account everything that has been discovered through inspections, analyzes and experimental work, it appears that the chlorides found in the pore solution combined with a presence of large voids is the main cause of the corrosion found on

the tensile wires in Herøysundet bridge. Through experimental testing, the chloride levels discovered have been determined to be high enough to cause corrosion given the pH levels measured on site. The presence of sulfates found in the grout have likely contributed to worsen the already corrosive environment inside the large voids detected. However, there might be other factors not considered in this thesis that have contributed to the corrosion.

Chapter 9

Recommendations for Future Work

As long-term testing appears to give the most realistic results, testing following method B should be the main focus in succeeding research. To get a deeper understanding of what effect the different factors have and how they affect each other, future work can include:

- Testing to more accurately determine chloride threshold levels:
  - Tests with chloride concentrations between 0.01 M and 0.1 M at pH = 12.5.
  - Tests with chloride concentrations between 0.01 M and 0.1 M at pH = 13.
- Testing to further investigate the effect of sulfates:
  - Tests with the addition of only sulfates from both sources.
  - Tests run with both chloride and sulfate ions of varying concentrations.
  - Tests run with new sources of sulfates to further test the effects.

In order to measure the long-term effect of oxygen removal, a solution has to discovered with regards to the evaporation of the electrolyte, alternately a new test method has to be created. New test methods should also be developed to take into account the galvanic corrosion that present itself due to the varying states within the tendon ducts.

Bibliography

[1] K.K. Krishna Vigneshwaran, S. Permeh, M. Echeverría, K. Lau and I. Lasa, 'Corrosion of Post-Tensioned Tendons with Deficient Grout, Part 1: Electrochemical Behavior of Steel in Alkaline Sulfate Solutions,' English, *Corrosion*, vol. 74, no. 3, pp. 362–371, Mar. 2018, Place: Houston Publisher: NACE International, issn: 00109312. doi: 10.5006/2541. [Online]. Available: https://www.proquest.com/scholarly-journals/corrosion-post-tensioned-tendons-with-deficient/docview/2422151872/se-2?accountid=12870.

[2] P. Xu, L. Jiang, M.-Z. Guo, J. Zha, L. Chen, C. Chen and N. Xu, 'Influence of sulfate salt type on passive film of steel in simulated concrete pore solution,' *Construction and Building Materials*, vol. 223, pp. 352–359, 2019, issn: 0950-0618. doi: 10.1016/j.conbuildmat.2019.06.209. [Online]. Available: https://www.sciencedirect.com/science/article/pii/S0950061819316381.

[3] R. D. Moser, P. M. Singh, L. F. Kahn and K. E. Kurtis, 'Chloride-Induced Corrosion of Prestressing Steels Considering Crevice Effects and Surface Imperfections,' English, *Corrosion*, vol. 67, no. 6, Jun. 2011, Place: Houston Publisher: NACE International, issn: 00109312. doi: 10.5006/1.3595096. [Online]. Available: https://www.proquest.com/scholarly-journals/chloride-induced-corrosion-prestressing-steels/docview/2421538145/se-2?accountid=12870.

[4] S.-K. Lee and J. Zielske, 'An FHWA special study: Post-tensioning tendon grout chloride thresholds,' English, Federal Highway Administration and Rutgers University, Piscataway, Tech. Rep. FHWA-HRT-14-039, 2014, p. 200. [Online]. Available: https://www.fhwa.dot.gov/publications/research/infrastructure/structures/bridge/14039/14039.pdf.

[5] U. M. Angst, M. R. Geiker, A. Michel, C. Gehlen, H. Wong, O. B. Isgor, B. Elsener, C. M. Hansson, R. François, K. Hornbostel, R. Polder, M. C. Alonso, M. Sanchez, M. J. Correia, M. Criado, A. Sagüés and N. Buenfeld, 'The steel–concrete interface,' *Materials and Structures*, vol. 50, no. 2, p. 143, Feb. 2017, issn: 1871-

6873. doi: 10.1617/s11527-017-1010-1. [Online]. Available: https://doi.org/10.1617/s11527-017-1010-1.

[6] L. Li and A. A. Sagüés, 'Chloride Corrosion Threshold of Reinforcing Steel in Alkaline Solutions—Open-Circuit Immersion Tests,' English, *Corrosion*, vol. 57, no. 1, pp. 19–28, Jan. 2001, Place: Houston Publisher: NACE International, issn: 00109312. doi: 10.5006/1.3290325. [Online]. Available: https://www.proquest.com/scholarly-journals/chloride-corrosion-threshold-reinforcing-steel/docview/2421220238/se-2?accountid=12870.

[7] L. Mammoliti, L. Brown, C. Hansson and B. Hope, 'The influence of surface finish of reinforcing steel and ph of the test solution on the chloride threshold concentration for corrosion initiation in synthetic pore solutions,' *Cement and Concrete Research*, vol. 26, no. 4, pp. 545–550, Apr. 1996, issn: 0008-8846. doi: 10.1016/0008-8846(96)00018-X. [Online]. Available: https://www.sciencedirect.com/science/article/pii/000888469600018X.

[8] S. Ahmad, 'Reinforcement corrosion in concrete structures, its monitoring and service life prediction—a review,' *Concrete Durability*, vol. 25, no. 4, pp. 459–471, 2003, issn: 0958-9465. doi: 10.1016/S0958-9465(02)00086-0. [Online]. Available: https://www.sciencedirect.com/science/article/pii/S0958946502000860.

[9] L. Bertolini, 'Chapter 4: General aspects,' English, in *Corrosion of steel in concrete : prevention, diagnosis, repair*, 2nd. completely rev. & enl. ed., Weinheim, Germany: Wiley-VCH, 2013, pp. 71–78, isbn: 1-5231-1549-1. [Online]. Available: http://ebookcentral.proquest.com/lib/ntnu/detail.action?docID=1138979.

[10] R. Holland, *Appraisal and repair of building structures: Reinforced concrete*. Thomas Telford Publishing, Jan. 1997, isbn: 978-0-7277-3717-5. doi: 10.1680/rc.25837. [Online]. Available: https://doi.org/10.1680/rc.25837 (visited on 15/09/2021).

[11] C. M. Hansson, 'Comments on electrochemical measurements of the rate of corrosion of steel in concrete,' *Cement and Concrete Research*, vol. 14, no. 4, pp. 574–584, Jul. 1984, issn: 0008-8846. doi: 10.1016/0008-8846(84)90135-2. [Online]. Available: https://www.sciencedirect.com/science/article/pii/0008884684901352.

[12] M. Pourbaix, *Atlas of electrochemical equilibria in aqueous solutions*, English, ser. Atlas d'équilibres électrochimiques. Oxford: Pergamon Press, 1966.

[13] T. D. Marcotte, 'Characterization of chloride-induced corrosion products that form in steel-reinforced cementitious materials,' English, Publisher: University of Waterloo, Ph.D. dissertation, University of Waterloo, Waterloo, Ontario, Canada, 2001. [Online]. Available: https://uwspace.uwaterloo.ca/bitstream/handle/10012/694/NQ65251.pdf?sequence=1.

[14] A. Poursaee, '2 - Corrosion of steel in concrete structures,' in *Corrosion of Steel in Concrete Structures*, A. Poursaee, Ed., Oxford: Woodhead Publishing, Jan. 2016, pp. 19–33, isbn: 978-1-78242-381-2. doi: 10.1016/B978-1-78242-381-2.00002-X. [Online]. Available: https://www.sciencedirect.com/science/article/pii/B978178242381200002X.

[15] K. Tuutti, 'Corrosion of steel in concrete,' English, Ph.D. dissertation, KTH, Kungliga Tekniska Högskolan i Stockholm, Swedish Cement and Concrete Research Institute, Stockholm, 1982. [Online]. Available: http://www.cbi.se/viewNavMenu.do?menuID=317&oid=857.

[16] L. Bertolini, 'Chapter 7: Electrochemical aspects,' English, in *Corrosion of steel in concrete : prevention, diagnosis, repair*, 2nd. completely rev. & enl. ed., Weinheim, Germany: Wiley-VCH, 2013, pp. 113–128, isbn: 1-5231-1549-1. [Online]. Available: http://ebookcentral.proquest.com/lib/ntnu/detail.action?docID=1138979.

[17] S. Laurens, P. Hénocq, N. Rouleau, F. Deby, E. Samson, J. Marchand and B. Bissonnette, 'Steady-state polarization response of chloride-induced macrocell corrosion systems in steel reinforced concrete — numerical and experimental investigations,' *Cement and Concrete Research*, vol. 79, pp. 272–290, Jan. 2016, issn: 0008-8846. doi: 10.1016/j.cemconres.2015.09.021. [Online]. Available: https://www.sciencedirect.com/science/article/pii/S0008884615002598.

[18] P. Ghods, O. B. Isgor, J. R. Brown, F. Bensebaa and D. Kingston, 'XPS depth profiling study on the passive oxide film of carbon steel in saturated calcium hydroxide solution and the effect of chloride on the film properties,' English, *Applied Surface Science*, vol. 257, no. 10, pp. 4669–4677, 2011, ISBN: 0169-4332 Publisher: Elsevier. doi: https://doi.org/10.1016/j.apsusc.2010.12.120.

[19] M. Sánchez, J. Gregori, C. Alonso, J. García-Jareño, H. Takenouti and F. Vicente, 'Electrochemical impedance spectroscopy for studying passive layers on steel rebars immersed in alkaline solutions simulating concrete pores,' *ELECTROCHEMICAL METHODS IN CORROSION RESEARCH Selection of papers from the 9th International Symposium (EMCR 2006) 18-23 June 2006, Dourdan, France*, vol. 52, no. 27, pp. 7634–7641, 2007, issn: 0013-4686. doi:

10.1016/j.electacta.2007.02.012. [Online]. Available: https://www.sciencedirect.com/science/article/pii/S0013468607002162.

[20] R. Janssen-Van Rosmalen, P. Bennema and J. Garside, 'The influence of volume diffusion on crystal growth,' *Journal of Crystal Growth*, vol. 29, no. 3, pp. 342–352, Jul. 1975, issn: 0022-0248. doi: 10.1016/0022-0248(75)90182-7. [Online]. Available: https://www.sciencedirect.com/science/article/pii/0022024875901827.

[21] Allan S. Myerson, *Handbook of industrial crystallization*, Second Edition. Boston: Butterworth-Heinemann, 2002, isbn: 1-281-07737-2.

[22] C. Andrade, 'Propagation of reinforcement corrosion: Principles, testing and modelling,' *Materials and Structures*, vol. 52, no. 1, p. 2, 2018, issn: 1871-6873. doi: 10.1617/s11527-018-1301-1. [Online]. Available: https://doi.org/10.1617/s11527-018-1301-1.

[23] O. Burkan Isgor, '13 - Modeling corrosion of steel in concrete,' in *Corrosion of Steel in Concrete Structures*, A. Poursaee, Ed., Oxford: Woodhead Publishing, Jan. 2016, pp. 249–267, isbn: 978-1-78242-381-2. doi: 10.1016/B978-1-78242-381-2.00013-4. [Online]. Available: https://www.sciencedirect.com/science/article/pii/B9781782423812000134.

[24] M. Raupach, 'Investigations on the influence of oxygen on corrosion of steel in concrete—Part I,' *Materials and Structures*, vol. 29, no. 3, pp. 174–184, Apr. 1996, issn: 1871-6873. doi: 10.1007/BF02486163. [Online]. Available: https://doi.org/10.1007/BF02486163.

[25] Portland Cement Association, *Corrosion of Embedded Materials*, English. [Online]. Available: https://www.cement.org/learn/concrete-technology/durability/corrosion-of-embedded-materials (visited on 07/12/2021).

[26] G. L. Cox and B. E. Roetheli, 'Effect of oxygen concentration on corrosion rates of steel and composition of corrosion products formed in oxygenated water,' *Industrial & Engineering Chemistry*, vol. 23, no. 9, pp. 1012–1016, 1931, ISBN: 0019-7866 Publisher: ACS Publications. [Online]. Available: https://pubs.acs.org/doi/pdf/10.1021/ie50261a011.

[27] P. Chess and W. Green, *Durability of Reinforced Concrete Structures*. Milton, UNITED KINGDOM: Taylor & Francis Group, 2020, isbn: 978-1-00-076668-4. [Online]. Available: http://ebookcentral.proquest.com/lib/ntnu/detail.action?docID=6001649.

[28] R. S. Raman, 'Characterisation of 'rolled-in', 'fragmented' and 'red' scale formation during secondary processing of steels,' *Engineering Failure Analysis*, vol. 13, no. 7, pp. 1044–1050, Oct. 2006, issn: 1350-6307. doi: 10.1016/j.engfailanal.2005.07.011. [Online]. Available: https://www.sciencedirect.com/science/article/pii/S1350630705001706.

[29] P. Ghods, O. Isgor, G. McRae, J. Li and G. Gu, 'Microscopic investigation of mill scale and its proposed effect on the variability of chloride-induced depassivation of carbon steel rebar,' *Corrosion Science*, vol. 53, no. 3, pp. 946–954, Mar. 2011, issn: 0010-938X. doi: 10.1016/j.corsci.2010.11.025. [Online]. Available: https://www.sciencedirect.com/science/article/pii/S0010938X10005706.

[30] U. M. Angst, M. R. Geiker, M. C. Alonso, R. Polder, O. B. Isgor, B. Elsener, H. Wong, A. Michel, K. Hornbostel, C. Gehlen, R. François, M. Sanchez, M. Criado, H. Sørensen, C. Hansson, R. Pillai, S. Mundra, J. Gulikers, M. Raupach, J. Pacheco and A. Sagüés, 'The effect of the steel–concrete interface on chloride-induced corrosion initiation in concrete: A critical review by RILEM TC 262-SCI,' *Materials and Structures*, vol. 52, no. 4, p. 88, Aug. 2019, issn: 1871-6873. doi: 10.1617/s11527-019-1387-0. [Online]. Available: https://doi.org/10.1617/s11527-019-1387-0.

[31] K. Xiao, C.-f. Dong, X.-g. Li and F.-m. Wang, 'Corrosion products and formation mechanism during initial stage of atmospheric corrosion of carbon steel,' *Journal of Iron and Steel Research International*, vol. 15, no. 5, pp. 42–48, May 2008, issn: 2210-3988. doi: 10.1016/S1006-706X(08)60247-2. [Online]. Available: https://doi.org/10.1016/S1006-706X(08)60247-2.

[32] X. Nie, X. Li, C. Du, Y. Huang and H. Du, 'Characterization of corrosion products formed on the surface of carbon steel by Raman spectroscopy,' *Journal of Raman Spectroscopy*, vol. 40, no. 1, pp. 76–79, Jan. 2009, Publisher: John Wiley & Sons, Ltd, issn: 0377-0486. doi: 10.1002/jrs.2082. [Online]. Available: https://doi.org/10.1002/jrs.2082 (visited on 12/05/2022).

[33] P. Refait, A.-M. Grolleau, M. Jeannin, C. Rémazeilles and R. Sabot, 'Corrosion of Carbon Steel in Marine Environments: Role of the Corrosion Product Layer,' *Corrosion and Materials Degradation*, vol. 1, no. 1, 2020, issn: 2624-5558. doi: 10.3390/cmd1010010.

[34] J. Avila-Mendoza, J. Flores and U. Castillo, 'Effect of Superficial Oxides on Corrosion of Steel Reinforcement Embedded in Concrete,' *Corrosion (Houston, Tex.)*, vol. 50, no. 11, pp. 879–885, 1994, Place: United States Publisher: United States: NACE International, issn: 0010-9312. doi: 10.5006/1.3293478.

[35] F. Li, Y. Yuan and C.-Q. Li, 'Corrosion propagation of prestressing steel strands in concrete subject to chloride attack,' *Construction and Building Materials*, vol. 25, no. 10, pp. 3878–3885, 2011, issn: 0950-0618. doi: 10.1016/j.conbuildmat.2011.04.011. [Online]. Available: https://www.sciencedirect.com/science/article/pii/S0950061811001516.

[36] P. Ghods, O. Isgor, G. McRae and G. Gu, 'Electrochemical investigation of chloride-induced depassivation of black steel rebar under simulated service conditions,' *Corrosion Science*, vol. 52, no. 5, pp. 1649–1659, May 2010, issn: 0010-938X. doi: 10.1016/j.corsci.2010.02.016. [Online]. Available: https://www.sciencedirect.com/science/article/pii/S0010938X10000752.

[37] C. Alonso, M. Castellote and C. Andrade, 'Chloride threshold dependence of pitting potential of reinforcements,' *Electrochimica Acta*, vol. 47, no. 21, pp. 3469–3481, Aug. 2002, issn: 0013-4686. doi: 10.1016/S0013-4686(02)00283-9. [Online]. Available: https://www.sciencedirect.com/science/article/pii/S0013468602002839.

[38] E. Bardal, *Corrosion and protection*. Springer Science & Business Media, 2007, isbn: 1-85233-845-8.

[39] K. B. Oldham, *Electrochemical science and technology : fundamentals and applications*, J. C. Myland and A. M. Bond, Eds. Chichester: Wiley, 2012, isbn: 978-0-470-71084-5.

[40] J. R. Scully and K. Lutton, '3.1 Polarization Behavior of Active Passive Metals and Alloys,' English, Center for Electochemical Science, Engineering, Department of Materials Science and Engineering, University of Virginia, Charlottesville, VA, United States, Tech. Rep., 2018, p. 13.

[41] S. Goñi and C. Andrade, 'Synthetic concrete pore solution chemistry and rebar corrosion rate in the presence of chlorides,' *Cement and Concrete Research*, vol. 20, no. 4, pp. 525–539, Jul. 1990, issn: 0008-8846. doi: 10.1016/0008-8846(90)90097-H. [Online]. Available: https://www.sciencedirect.com/science/article/pii/000888469090097H.

[42] M. Moreno, W. Morris, M. Alvarez and G. Duffó, 'Corrosion of reinforcing steel in simulated concrete pore solutions: Effect of carbonation and chloride content,' *Corrosion Science*, vol. 46, no. 11, pp. 2681–2699, Nov. 2004, issn: 0010-938X. doi: 10.1016/j.corsci.2004.03.013. [Online]. Available: https://www.sciencedirect.com/science/article/pii/S0010938X04000770.

[43] C. Alonso, C. Andrade, M. Castellote and P. Castro, 'Chloride threshold values to depassivate reinforcing bars embedded in a standardized OPC mortar,' *Cement and Concrete Research*, vol. 30, no. 7, pp. 1047–1055, Jul. 2000, issn: 0008-8846. doi: 10.1016/S0008-8846(00)00265-9. [Online]. Available: https://www.sciencedirect.com/science/article/pii/S0008884600002659.

[44] A. C. I. Committee, 'Building code requirements for structural concrete (ACI 318-08) and commentary,' American Concrete Institute, 2008, isbn: 0-87031-264-2.

[45] Virmani, Paul Y. and Ghasemi, Hamid, 'Literature Review of Chloride Threshold Values for Grouted Post-Tensioned Tendons,' English, United States. Federal Highway Administration. Office of Infrastructure ..., Tech. Rep. FHWA-HRT-12-067, 2012, p. 16. [Online]. Available: https://www.fhwa.dot.gov/publications/research/infrastructure/structures/bridge/12067/12067.pdf.

[46] B. Pradhan and B. Bhattacharjee, 'Rebar corrosion in chloride environment,' *Construction and Building Materials*, vol. 25, no. 5, pp. 2565–2575, 2011, issn: 0950-0618. doi: 10.1016/j.conbuildmat.2010.11.099. [Online]. Available: https://www.sciencedirect.com/science/article/pii/S095006181000629X.

[47] B. Martıén-Pérez, H. Zibara, R. Hooton and M. Thomas, 'A study of the effect of chloride binding on service life predictions,' *Cement and Concrete Research*, vol. 30, no. 8, pp. 1215–1223, Aug. 2000, issn: 0008-8846. doi: 10.1016/S0008-8846(00)00339-2. [Online]. Available: https://www.sciencedirect.com/science/article/pii/S0008884600003392.

[48] C. Hansson, '1 - An introduction to corrosion of engineering materials,' in *Corrosion of Steel in Concrete Structures*, A. Poursaee, Ed., Oxford: Woodhead Publishing, Jan. 2016, pp. 3–18, isbn: 978-1-78242-381-2. doi: 10.1016/B978-1-78242-381-2.00001-8. [Online]. Available: https://www.sciencedirect.com/science/article/pii/B9781782423812000018.

[49] C. M. Hansson, 'The Impact of Corrosion on Society,' *Metallurgical and Materials Transactions A*, vol. 42, no. 10, pp. 2952–2962, 2011, issn: 1543-1940. doi: 10.1007/s11661-011-0703-2. [Online]. Available: https://doi.org/10.1007/s11661-011-0703-2.

[50] R. Johnsen, 'Corrosion testing of tensile wire,' English, Department of Mechanical and Industrial Engineering (MTP), NTNU, Tech. Rep. 90599200-03, Aug. 2021, p. 14.

[51] L. Bertolini, B. Elsener, P. Pedeferri, E. Redaelli and R. B. Polder, 'Chapter 2: Transport Processes in Concrete,' English, in *Corrosion of steel in concrete : prevention, diagnosis, repair*, 2nd. completely rev. & enl. ed., Weinheim, Germany: John Wiley & Sons, 2013, pp. 21–48, isbn: 3-527-65171-3. [Online]. Available: http://ebookcentral.proquest.com/lib/ntnu/detail.action?docID=1138979.

[52] S. Mindess, *Concrete*, 2nd ed., D. Darwin and J. F. Young, Eds. Upper Saddle River, N.J: Prentice Hall, 2003, isbn: 0-13-064632-6.

[53] O. S. B. Al-Amoudi, 'Sulfate attack and reinforcement corrosion in plain and blended cements exposed to sulfate environments,' *Building and Environment*, vol. 33, no. 1, pp. 53–61, Jan. 1998, issn: 0360-1323. doi: 10.1016/S0360-1323(97)00022-X. [Online]. Available: https://www.sciencedirect.com/science/article/pii/S036013239700022X.

[54] T. Nijland and J. Larbi, '8 - Microscopic examination of deteriorated concrete,' in *Non-Destructive Evaluation of Reinforced Concrete Structures*, C. Maierhofer, H.-W. Reinhardt and Gerd Dobmann, Eds., vol. 1, Woodhead Publishing, Jan. 2010, pp. 137–179, isbn: 978-1-84569-560-6. doi: 10.1533/9781845699536.2.137. [Online]. Available: https://www.sciencedirect.com/science/article/pii/B9781845695606500088.

[55] Corrosionpedia, *What is Ettringite? - Definition from Corrosionpedia*, en. [Online]. Available: http://www.corrosionpedia.com/definition/473/ettringite (visited on 25/11/2021).

[56] B. Pradhan, 'Corrosion behavior of steel reinforcement in concrete exposed to composite chloride–sulfate environment,' *Construction and Building Materials*, vol. 72, pp. 398–410, 2014, issn: 0950-0618. doi: 10.1016/j.conbuildmat.2014.09.026. [Online]. Available: https://www.sciencedirect.com/science/article/pii/S0950061814010423.

[57] H. Dehwah, M. Maslehuddin and S. Austin, 'Long-term effect of sulfate ions and associated cation type on chloride-induced reinforcement corrosion in Portland cement concretes,' *CORROSION AND CORROSION MONITORING*, vol. 24, no. 1, pp. 17–25, Feb. 2002, issn: 0958-9465. doi: 10.1016/S0958-9465(01)00023-3. [Online]. Available: https://www.sciencedirect.com/science/article/pii/S0958946501000233.

[58] Y. Xu, 'The influence of sulphates on chloride binding and pore solution chemistry,' *Cement and Concrete Research*, vol. 27, no. 12, pp. 1841–1850, 1997, issn: 0008-8846. doi: 10.1016/S0008-8846(97)00196-8. [Online]. Available: https://www.sciencedirect.com/science/article/pii/S0008884697001968.

[59] A. Köliö, T. A. Pakkala, J. Lahdensivu and M. Kiviste, 'Durability demands related to carbonation induced corrosion for Finnish concrete buildings in changing climate,' *Engineering Structures*, vol. 62-63, pp. 42–52, Mar. 2014, issn: 0141-0296. doi: 10.1016/j.engstruct.2014.01.032. [Online]. Available: https://www.sciencedirect.com/science/article/pii/S0141029614000467.

[60] L. Bertolini, B. Elsener, P. Pedeferri, E. Redaelli and R. B. Polder, 'Chapter 8: Macrocells,' English, in *Corrosion of Steel in Concrete : Prevention, Diagnosis, Repair*, Weinheim, GERMANY: John Wiley & Sons, Incorporated, 2014, pp. 129–139, isbn: 978-3-527-65171-9. [Online]. Available: http://ebookcentral.proquest.com/lib/ntnu/detail.action?docID=1138979.

[61] A. Castel and A. Nasser, 'Microcell versus galvanic corrosion currents in carbonated concrete,' *Magazine of Concrete Research*, vol. 66, no. 14, pp. 697–707, 2014, tex.eprint: https://doi.org/10.1680/macr.13.00214. doi: 10.1680/macr.13.00214. [Online]. Available: https://doi.org/10.1680/macr.13.00214.

[62] Z. Dong and A. Poursaee, 'Corrosion behavior of coupled active and passive reinforcing steels in simulated concrete pore solution,' *Construction and Building Materials*, vol. 240, p. 117 955, Apr. 2020, issn: 0950-0618. doi: 10.1016/j.conbuildmat.2019.117955. [Online]. Available: https://www.sciencedirect.com/science/article/pii/S0950061819334087.

[63] ACI Committee 201 and American Concrete Institute, *Guide to durable concrete*, en. Farmington Hills, Mich.: American Concrete Institute, 2008, OCLC: 244388069, isbn: 978-0-87031-284-7.

[64] L. Bertolini, B. Elsener, P. Pedeferri, E. Redaelli and R. B. Polder, 'Chapter 1: Cements and Cement Paste,' English, in *Corrosion of Steel in Concrete : Prevention, Diagnosis, Repair*, Weinheim, GERMANY: John Wiley & Sons, Incorporated, 2014, pp. 1–20, isbn: 978-3-527-65171-9. [Online]. Available: http://ebookcentral.proquest.com/lib/ntnu/detail.action?docID=1138979.

[65] O. Jensen, P. Hansen, A. Coats and F. Glasser, 'Chloride ingress in cement paste and mortar,' *Cement and Concrete Research*, vol. 29, no. 9, pp. 1497–1504, Sep. 1999, issn: 0008-8846. doi: 10.1016/S0008-8846(99)00131-3. [Online]. Available: https://www.sciencedirect.com/science/article/pii/S0008884699001313.

[66] B. H. Oh, S. W. Cha, B. S. Jang and S. Y. Jang, 'Development of high-performance concrete having high resistance to chloride penetration,' *Nuclear Engineering and Design*, vol. 212, no. 1, pp. 221–231, Mar. 2002, issn: 0029-5493. doi: 10.1016/S0029-5493(01)00484-8. [Online]. Available: https://www.sciencedirect.com/science/article/pii/S0029549301004848.

[67] S. H. Kosmatka, B. Kerkhoff and W. C. Panarese, *Design and control of concrete mixtures*. Portland Cement Association Skokie, IL, 2002, vol. 5420.

[68] B. Yu, J. Liu and B. Li, 'Improved numerical model for steel reinforcement corrosion in concrete considering influences of temperature and relative humidity,' *Construction and Building Materials*, vol. 142, pp. 175–186, Jul. 2017, issn: 0950-0618. doi: 10.1016/j.conbuildmat.2017.03.045. [Online]. Available: https://www.sciencedirect.com/science/article/pii/S095006181730418X.

[69] J. Balayssac, C. Détriché and J. Grandet, 'Effects of curing upon carbonation of concrete,' *Construction and Building Materials*, vol. 9, no. 2, pp. 91–95, Apr. 1995, issn: 0950-0618. doi: 10.1016/0950-0618(95)00001-V. [Online]. Available: https://www.sciencedirect.com/science/article/pii/095006189500001V.

[70] R. Holland, K. Kurtis and L. Kahn, '7 - Effect of different concrete materials on the corrosion of the embedded reinforcing steel,' in *Corrosion of Steel in Concrete Structures*, A. Poursaee, Ed., Oxford: Woodhead Publishing, Jan. 2016, pp. 131–147, isbn: 978-1-78242-381-2. doi: 10.1016/B978-1-78242-381-2.00007-9. [Online]. Available: https://www.sciencedirect.com/science/article/pii/B9781782423812000079.

[71] L. Bertolini, B. Elsener, P. Pedeferri, E. Redaelli and R. B. Polder, 'Chapter 3: Degredation of Concrete,' English, in *Corrosion of steel in concrete : prevention, diagnosis, repair*, 2nd. completely rev. & enl. ed., Weinheim, Germany: John Wiley & Sons, 2013, pp. 49–69, isbn: 3-527-65171-3. [Online]. Available: http://ebookcentral.proquest.com/lib/ntnu/detail.action?docID=1138979.

[72] C. L. Page and Ø. Vennesland, 'Pore solution composition and chloride binding capacity of silica-fume cement pastes,' *Matériaux et construction*, vol. 16, no. 1, pp. 19–25, 1983, ISBN: 1871-6873 Publisher: Springer. doi: https://doi.org/10.1007/BF02474863.

[73] British Standards Institution, 'BS EN 206-1:2000 Concrete - part 1: Specification, performance, production and conformity,' English, British Standards Institution, London, Standard 0 580 36882 3, Dec. 2000, p. 69. [Online]. Available: https://allbeton.ru/upload/iblock/d27/bs_en_206_1_2000_concrete_part_1_specification_performance_production_and_conformity.pdf.

[74] N. R. Hewson, '4: Grouting post-tensioned tendons,' English, in *Prestressed concrete bridges: design and construction*, Thomas Telford, 2003, pp. 46–59, isbn: 0-7277-3223-4. [Online]. Available: https://www.icevirtuallibrary.com/doi/abs/10.1680/pcbdac.32231.0004.

[75] British Standards Institution, 'BS EN 447:2007 Grout for prestressing tendons - Basic requirements,' English, British Standards Institution, London, Standard 978 0 580 55814 6, Nov. 2007, p. 14. [Online]. Available: https://www.academia.edu/42469121/Grout_for_prestressing_tendons_Basic_requirements.

[76] J. Corven and A. J. Moreton, 'Post-tensioning tendon installation and grouting manual,' English, Federal Highway Administration (US), Tech. Rep. FHWA-NHI-13-026, 2013, p. 184. [Online]. Available: https://rosap.ntl.bts.gov/view/dot/53649.

[77] Stanton Walker and Delmar L. Bloem, 'Effects of Aggregate Size on Properties of Concrete,' *ACI Journal Proceedings*, vol. 57, no. 9, Sep. 1960. doi: 10.14359/8021.

[78] P. Bhatt, *Reinforced concrete : design theory and examples*, 3rd ed., B. Choo and T. MacGinley, Eds. London: Taylor & Francis, 2006, isbn: 0-415-30795-3.

[79] R. Johnsen, 'Herøysund bru - korrosjon av spenntråd,' Norsk, NTNU, Tech. Rep. 90599200-1, 2021, p. 37.

[80] L. Steinholt, *Ny bru skal opp på under tre år*, nb-NO, Oct. 2020. [Online]. Available: https://www.hblad.no/2020/nyheter/ny-bru-skal-opp-pa-under-tre-ar/ (visited on 27/09/2021).

[81] *Vektbegrensning over brua*, nb-NO, Dec. 2019. [Online]. Available: https://www.hblad.no/2019/nyheter/vektbegrensning-over-brua/ (visited on 27/09/2021).

[82] A. Karlsson and P. Jilderda, 'Utredning av metoder for inspeksjon av etterspent armering i betongbruer,' p. 186, 2021, ISBN: 1893-1162 Publisher: Statens vegvesen. [Online]. Available: https://hdl.handle.net/11250/2728767.

[83] N. Hewson, 'Proprietary systems,' in *Prestressed Concrete Bridges: Design and Construction*, ICE Publishing, 2012, pp. 377–400.

[84] Hewson, Nigel R., 'Prestress design,' English, in *Prestressed concrete bridges: design and construction*, Thomas Telford, 2003, pp. 60–97, isbn: 0-7277-3223-4. doi: 10.1680/pcbdac.32231.0005. [Online]. Available: https://www.icevirtuallibrary.com/doi/abs/10.1680/pcbdac.32231.0005.

[85] C. W. Dolan and H. R. (Hamilton, 'Basic Concepts,' in *Prestressed Concrete: Building, Design, and Construction*, C. W. Dolan and H. R. (Hamilton, Eds., Cham: Springer International Publishing, 2019, pp. 1–30, isbn: 978-3-319-97882-6. doi: 10.1007/978-3-319-97882-6_1. [Online]. Available: https://doi.org/10.1007/978-3-319-97882-6_1.

[86] N. R. Hewson, '18: Problems and failures,' English, in *Prestressed concrete bridges: design and construction*, Thomas Telford, 2003, pp. 314–325, isbn: 0-7277-3223-4. [Online]. Available: https://www.icevirtuallibrary.com/doi/abs/10.1680/pcbdac.32231.0018.

[87] L. Bertolini and M. Carsana, 'High pH corrosion of prestressing steel in segregated grout,' in *Modelling of corroding concrete structures*, Springer, 2011, pp. 147–158.

[88] J. P. Wouters, K. Kesner and R. W. Poston, 'Tendon corrosion in precast segmental bridges,' English, *Transportation research record*, vol. 1654, no. 1, pp. 128–132, 1999, ISBN: 0361-1981 Publisher: SAGE Publications Sage CA: Los Angeles, CA. [Online]. Available: https://journals.sagepub.com/doi/abs/10.3141/1654-15.

[89] Marit Haugen, 'Prøvingsrapport - Laboratorieundersøkelse av injiseringsmasse fra innsiden av kabelkanal for spennarmering på Herøysundet bru,' Norsk, SINTEF, Tech. Rep. 3040-163, Mar. 2020, Prosjektnummer: 102003040-163, p. 5.

[90] Tobias Danner, 'Prøvingsrapport - Undersøkelser av injiseringsmassen fra kabelkanal til Herøysund bru,' Norsk, SINTEF, Tech. Rep. 3039-282, Nov. 2020, p. 9.

[91] N. R. Hewson, '3: Durability and detailing,' English, in *Prestressed concrete bridges: design and construction*, Thomas Telford, 2003, pp. 34–45, isbn: 0-7277-3223-4. [Online]. Available: https://www.icevirtuallibrary.com/doi/abs/10.1680/pcbdac.32231.0003.

[92] K. Andersson, B. Allard, M. Bengtsson and B. Magnusson, 'Chemical composition of cement pore solutions,' *Cement and Concrete Research*, vol. 19, no. 3, pp. 327–332, 1989, issn: 0008-8846. doi: 10.1016/0008-8846(89)90022-7. [Online]. Available: https://www.sciencedirect.com/science/article/pii/0008884689900227.

[93] A. Vollpracht, B. Lothenbach, R. Snellings and J. Haufe, 'The pore solution of blended cements: A review,' *Materials and Structures*, vol. 49, no. 8, pp. 3341–3367, 2016, ISBN: 1871-6873 Publisher: Springer. doi: https://doi.org/10.1617/s11527-015-0724-1.

[94] A. Poursaee and C. M. Hansson, 'Reinforcing steel passivation in mortar and pore solution,' English, *Cement and Concrete Research*, vol. 37, no. 7, pp. 1127–1133, 2007, ISBN: 0008-8846 Publisher: Elsevier. [Online]. Available: https://www.sciencedirect.com/science/article/pii/S0008884607000993.

[95] Y.-M. Chen and M. E. Orazem, 'Impedance analysis of ASTM A416 tendon steel corrosion in alkaline simulated pore solutions,' *Corrosion Science*, vol. 104, pp. 26–35, Mar. 2016, issn: 0010-938X. doi: 10.1016/j.corsci.2015.11.027. [Online]. Available: https://www.sciencedirect.com/science/article/pii/S0010938X15301694.

[96] S. Abd El Haleem, S. Abd El Wanees, E. Abd El Aal and A. Diab, 'Environmental factors affecting the corrosion behavior of reinforcing steel II. Role of some anions in the initiation and inhibition of pitting corrosion of steel in Ca(OH)2 solutions,' *Corrosion Science*, vol. 52, no. 2, pp. 292–302, Feb. 2010, issn: 0010-938X. doi: 10.1016/j.corsci.2009.09.004. [Online]. Available: https://www.sciencedirect.com/science/article/pii/S0010938X09004375.

[97] J. Flis, H. Pickering and K. Osseo-Asare, 'Interpretation of impedance data for reinforcing steel in alkaline solution containing chlorides and acetates,' *Electrochimica Acta*, vol. 43, no. 12, pp. 1921–1929, 1998, issn: 0013-4686. doi: 10.1016/S0013-4686(97)10004-4. [Online]. Available: https://www.sciencedirect.com/science/article/pii/S0013468697100044.

[98] P. Ghods, O. B. Isgor, F. Bensebaa and D. Kingston, 'Angle-resolved XPS study of carbon steel passivity and chloride-induced depassivation in simulated concrete pore solution,' English, *Corrosion Science*, vol. 58, pp. 159–167, 2012, ISBN: 0010-938X Publisher: Elsevier. doi: https://doi.org/10.1016/j.corsci.2012.01.019.

[99] A. Al-Tayyib, S. Somuah, J. Boah, P. Leblanc and A. Al-Mana, 'Laboratory study on the effect of sulfate ions on rebar corrosion,' *Cement and Concrete Research*, vol. 18, no. 5, pp. 774–782, Sep. 1988, issn: 0008-8846. doi: 10.1016/0008-8846(88)90102-0. [Online]. Available: https://www.sciencedirect.com/science/article/pii/0008884688901020.

[100] I. Pepenar, 'Electrochemical Behavior of the Prestressing Steel in Alkaline Electrolytes: Influence of Chloride Ions,' English, *NACE International Corrosion Conference Proceedings*, pp. 1–8, 2017, Place: Houston Publisher: NACE International. [Online]. Available: https://www.proquest.com/conference-papers-proceedings/electrochemical-behavior-prestressing-steel/docview/2459460729/se-2?accountid=12870.

[101] A. Nasser, A. Clément, S. Laurens and A. Castel, 'Influence of steel–concrete interface condition on galvanic corrosion currents in carbonated concrete,' *Corrosion Science*, vol. 52, no. 9, pp. 2878–2890, Sep. 2010, issn: 0010-938X. doi: 10.1016/j.corsci.2010.04.037. [Online]. Available: https://www.sciencedirect.com/science/article/pii/S0010938X10002246.

[102] P. R. Roberge, *Corrosion engineering : principles and practice*. New York: McGraw-Hill, 2008, isbn: 978-0-07-148243-1.

[103] C. Andrade and J. A. González, 'Quantitative measurements of corrosion rate of reinforcing steels embedded in concrete using polarization resistance measurements,' *Materials and Corrosion*, vol. 29, no. 8, pp. 515–519, 1978, ISBN: 0947-5117 Publisher: Wiley Online Library. doi: https://doi.org/10.1002/maco.19780290804.

Appendix A

Results from Method A

A.1 Cyclic Polarization Curves

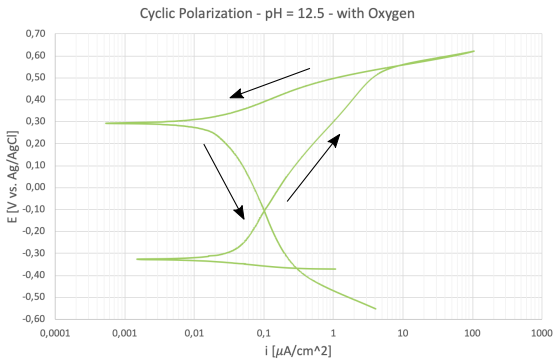

(a) Solution 10

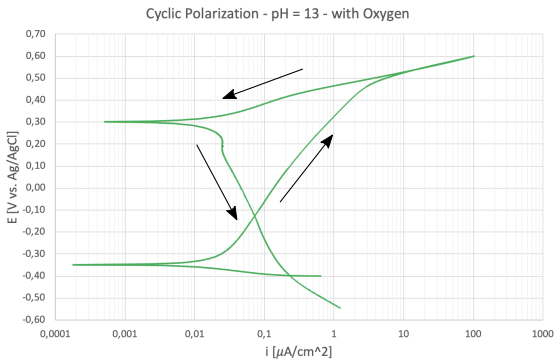

(b) Solution 11

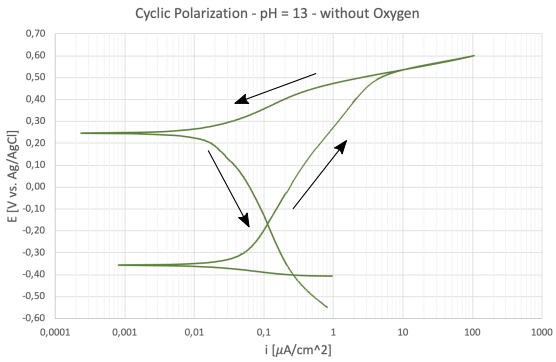

(c) Solution 12

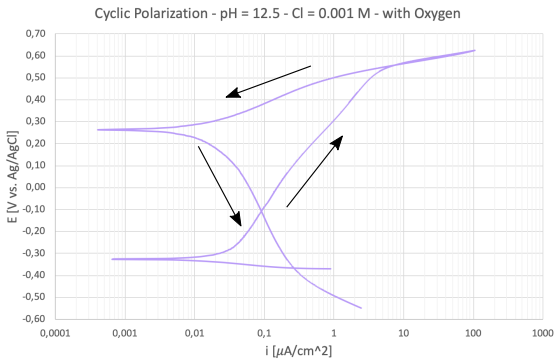

(d) Solution 13

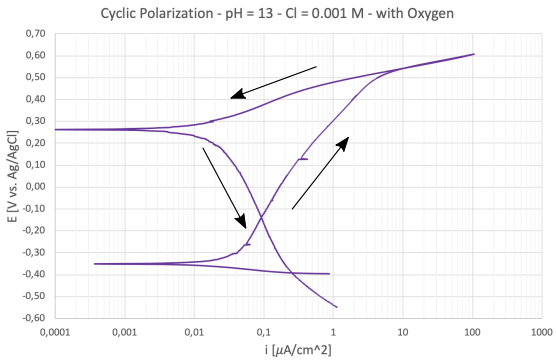

(e) Solution 14

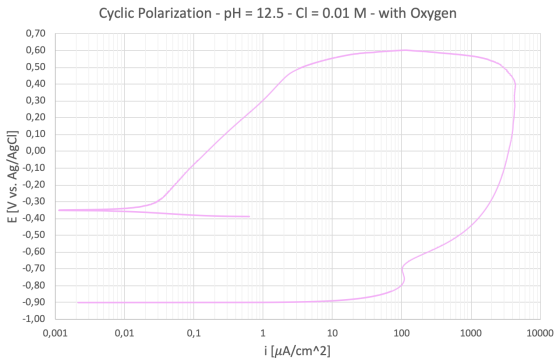

(f) Solution 15

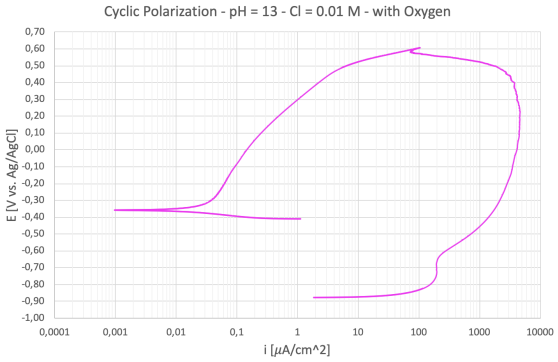

(g) Solution 16

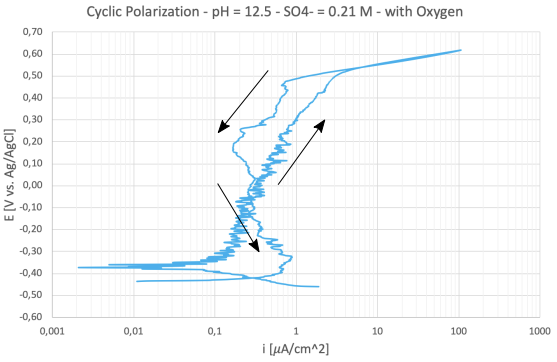

(h) Solution 17

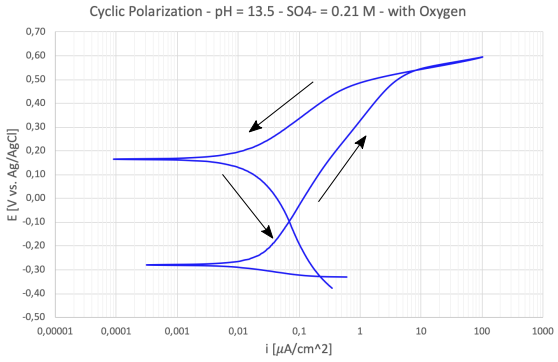

(i) Solution 18

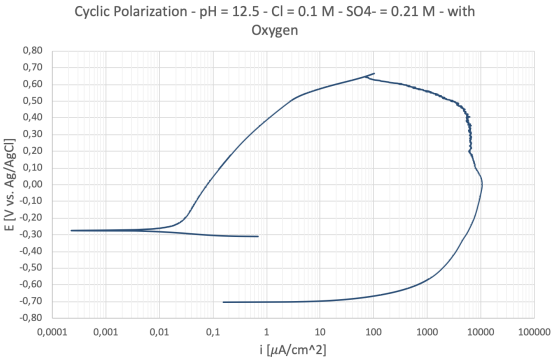

(j) Solution 19

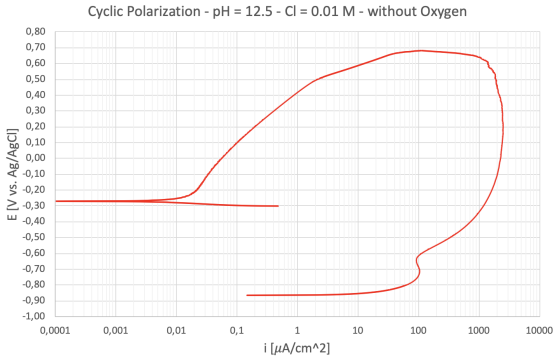

(k) Solution 20

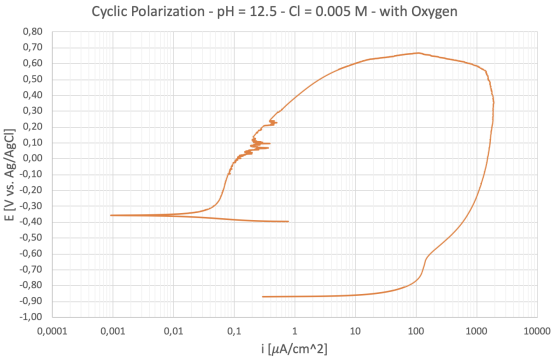

(l) Solution 21

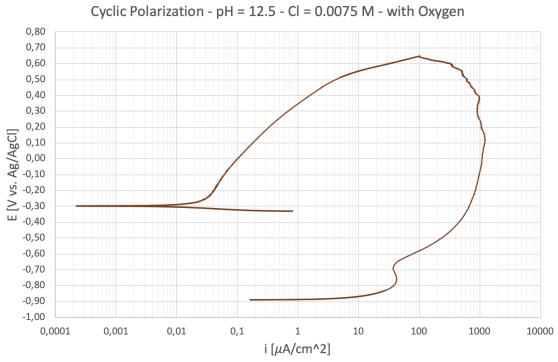

(m) Solution 22

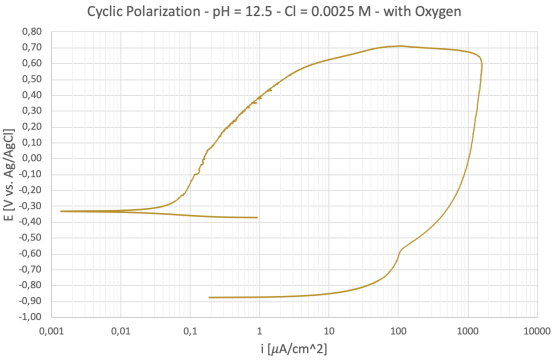

(n) Solution 23

Figure A.1: All individual CP curves measured according to method A.

A.2 Visual Inspections

(a) Solution 15

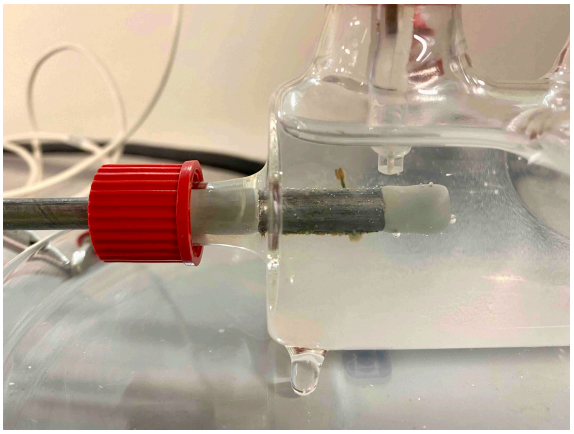

(b) Solution 16

(c) Solution 19

(d) Solution 20

(e) Solution 21

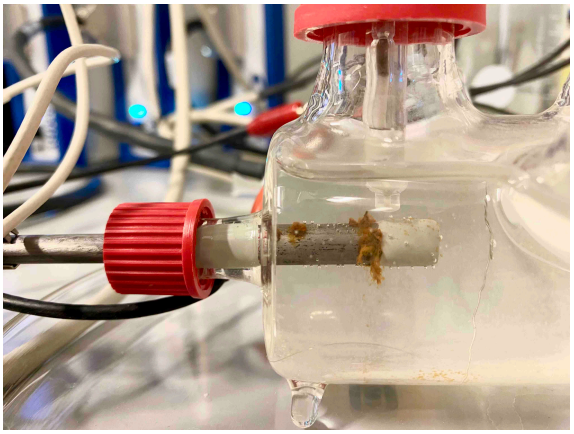

(f) Solution 22

(g) Solution 23

Figure A.2: Images depicting the situation after ended CP measurements for the corroded samples.

Test Samples

(a) Solution 15

(b) Solution 16

(c) Solution 17

(d) Solution 19

(e) Solution 20

(f) Solution 21

(g) Solution 22

(h) Solution 23

Figure A.3: Visual inspections of samples displaying signs of corrosion.

Appendix B

Results from Method B

B.1 OCP Measurements

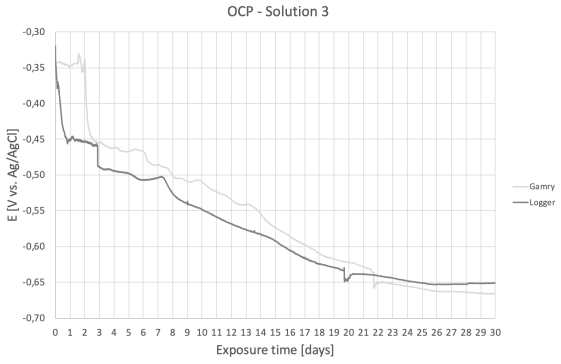

(a) Solution 3

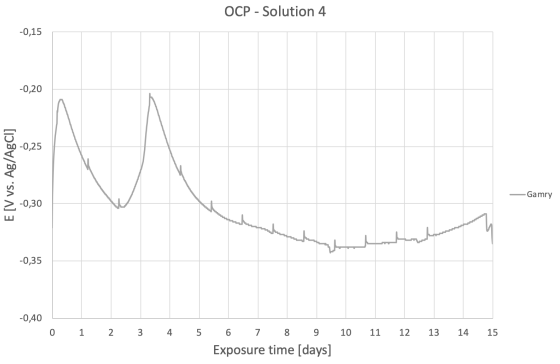

(b) Solution 4

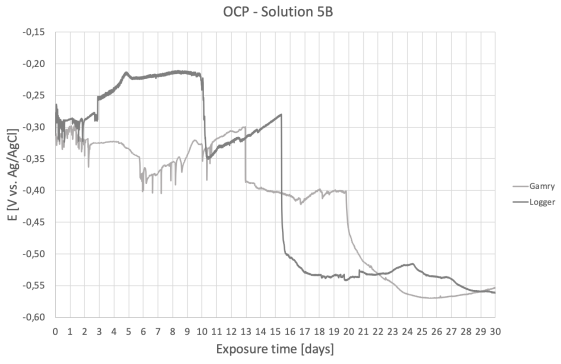

(c) Solution 5B

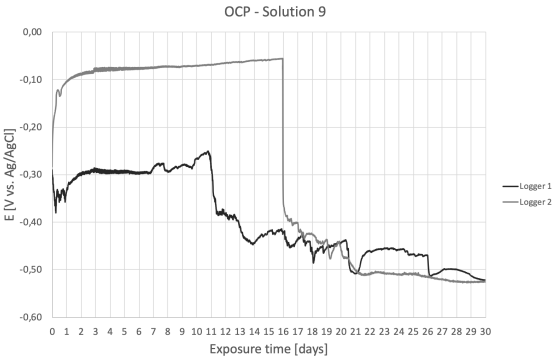

(d) Solution 9

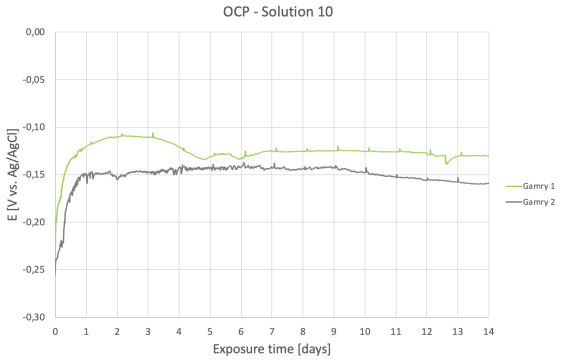

(e) Solution 10

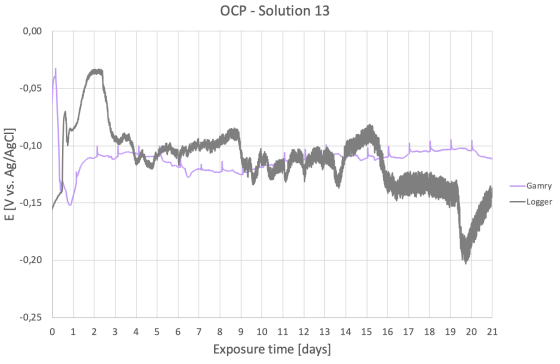

(f) Solution 13

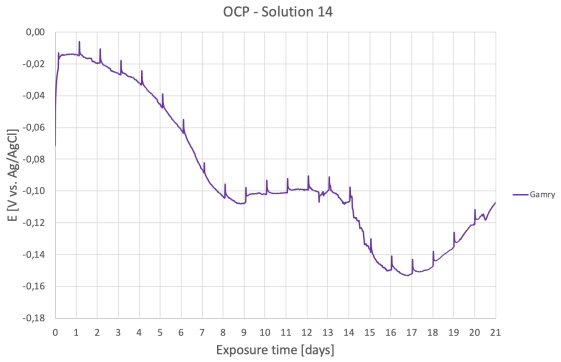

(g) Solution 14

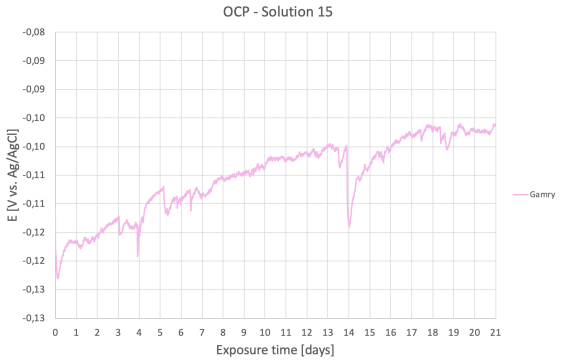

(h) Solution 15

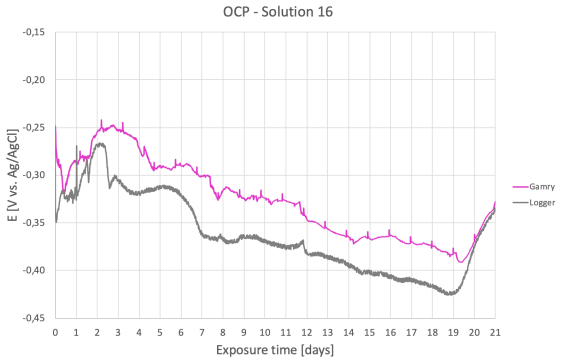

(i) Solution 16

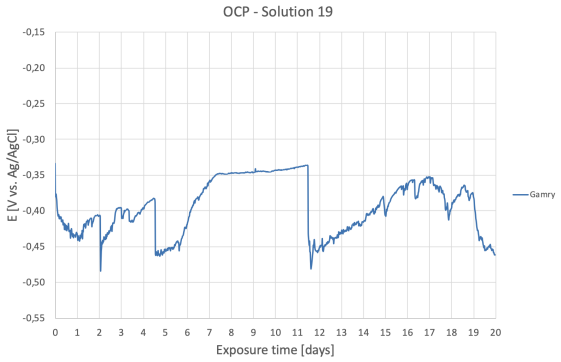

(j) Solution 19

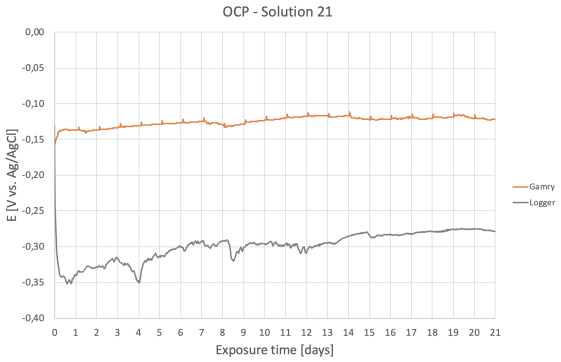

(k) Solution 21

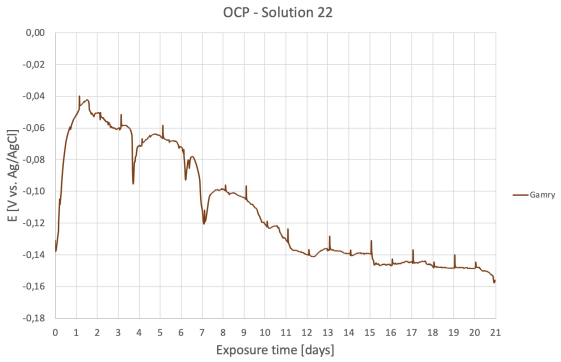

(l) Solution 22

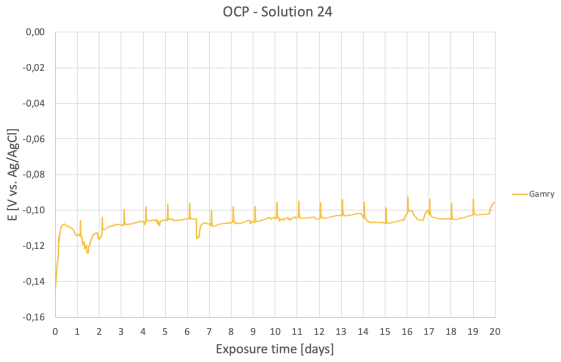

(m) Solution 24

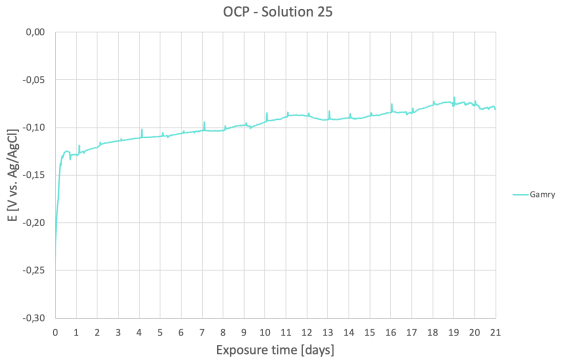

(n) Solution 25

Figure B.1: OCP measurements performed using either or both a Gamry potentiostat and a potential logger.

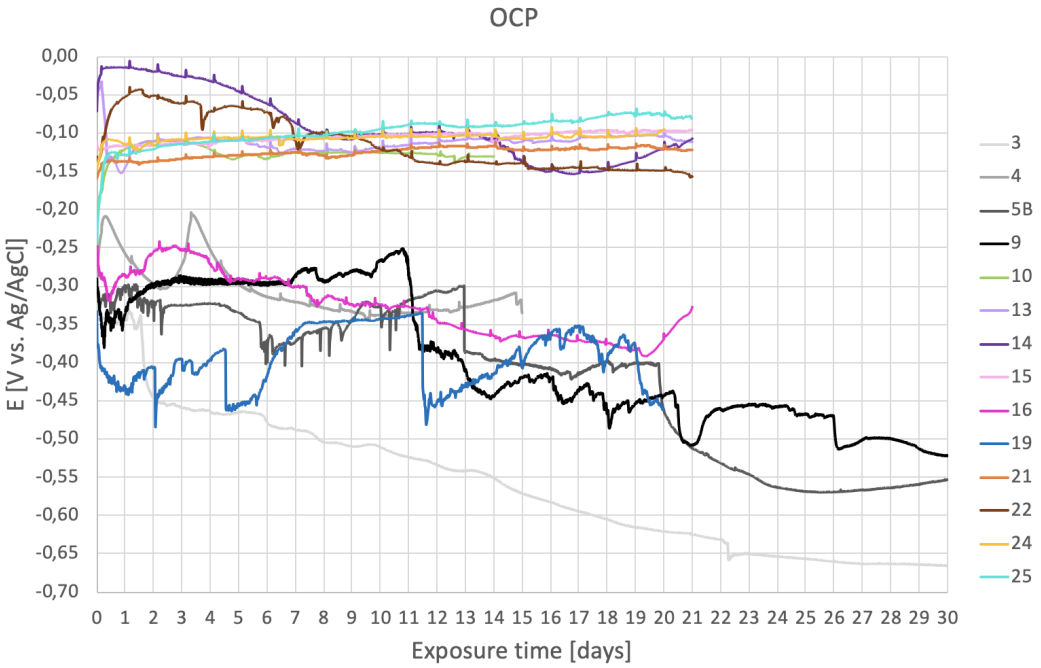

Figure B.2: Plot showing the OCP development made with a Gamry potentiostat for all solutions during the exposure time. Illustrates the difference in potential between the different solutions.

B.2 LPR Measurements

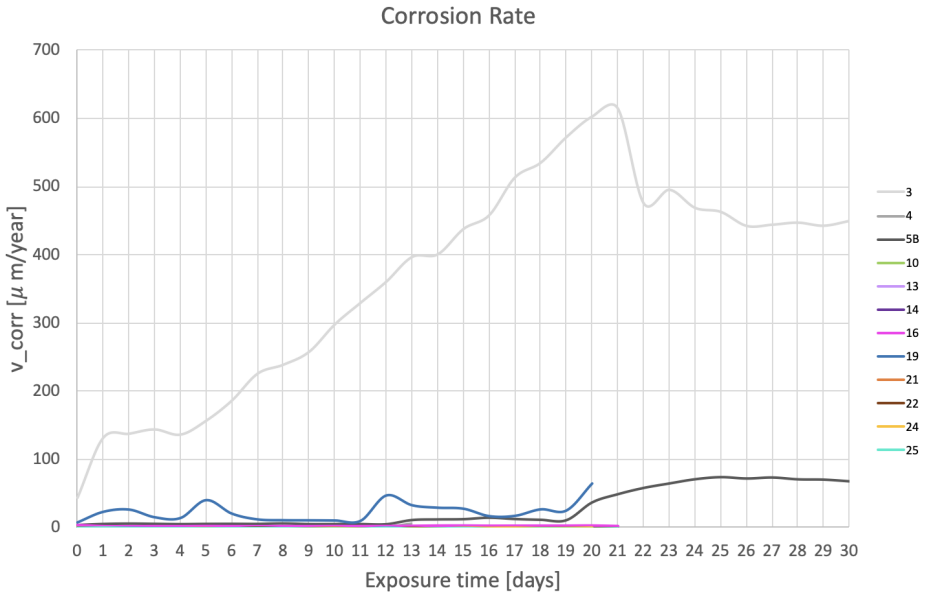

Figure B.3: Corrosion rates for all solutions tested. Calculated from LPR measurements using the original surface area.

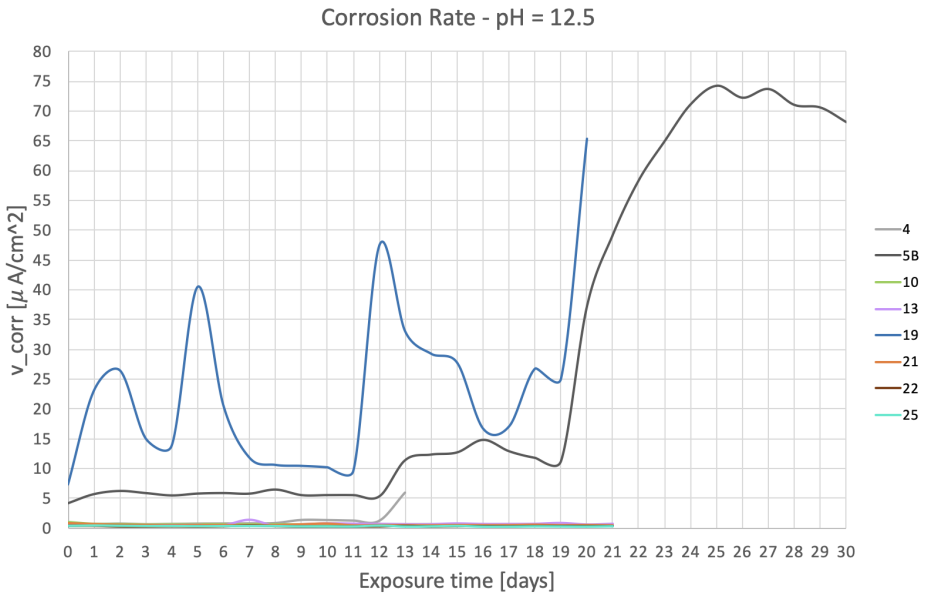

Figure B.4: Corrosion rates for solutions with a pH of 12.5, calculated from LPR measurements.

Table B.1: Results from method B. Data extracted from the polarization curves shown in Figure B.2 and B.3

Solution[1]	OCP-start [$mV_{Ag/AgCl}$]	OCP-finish [$mV_{Ag/AgCl}$]	i_{corr}−start [$\mu A/cm^2$]	i_{corr}−finish [$\mu A/cm^2$]
3 (Logger)	-335	-651	-	-
3 (Gamry)	-342	-666	3.827	38.826
4 (Gamry)	-321	-335	0.050	0.520
5B (Logger)	-313	-562	-	-
5B (Gamry)	-309	-553	0.358	5.870
9 (Logger1)	-283	-530	-	-
9 (Logger2)	-290	-525	-	-
10 (Gamry1)	-255	-159	0.234	0.091
10 (Gamry2)	-253	-130	0.089	0.050
13 (Logger)	-155	-138	-	-
13 (Gamry)	-62	-111	0.046	0.069
14 (Gamry)	-71	-107	0.037	0.026
15 (Logger)	-111	-96	-	-
16 (Logger)	-254	-336	-	-
16 (Gamry)	-250	-328	0.360	0.202
19 (Gamry)	-333	-462	0.626	5.626
21 (Logger)	-130	-279	-	-
21 (Gamry)	-159	-122	0.065	0.045
22 (Gamry)	-131	-157	0.037	0.036
24 (Gamry)	-147	-95	0.029	0.031
25 (Gamry)	-242	-81	0.039	0.035

[1] Solution referred to according to Figure 5.8.

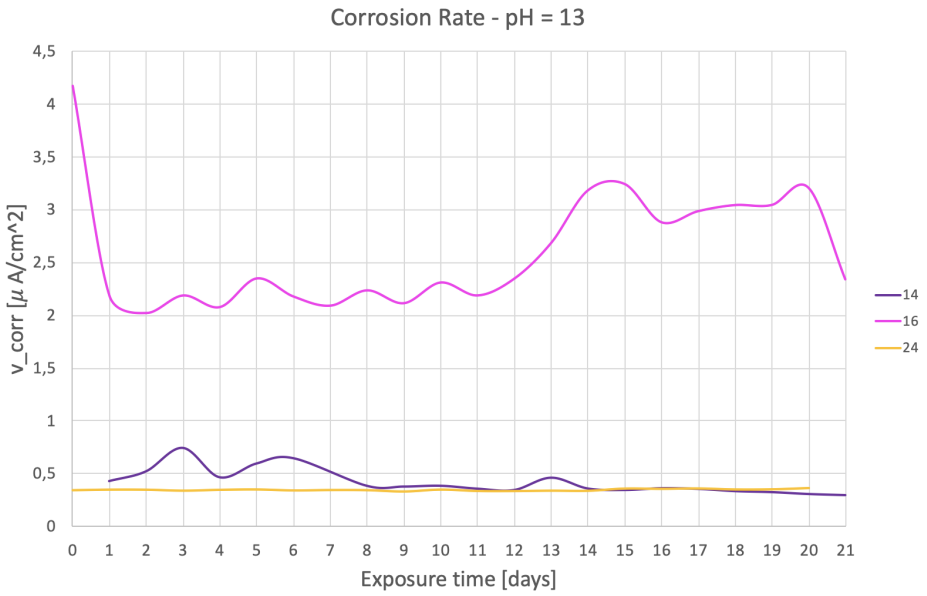

Figure B.5: Corrosion rates for solutions with a pH of 13, calculated from LPR measurements.

B.3 Visual Inspections

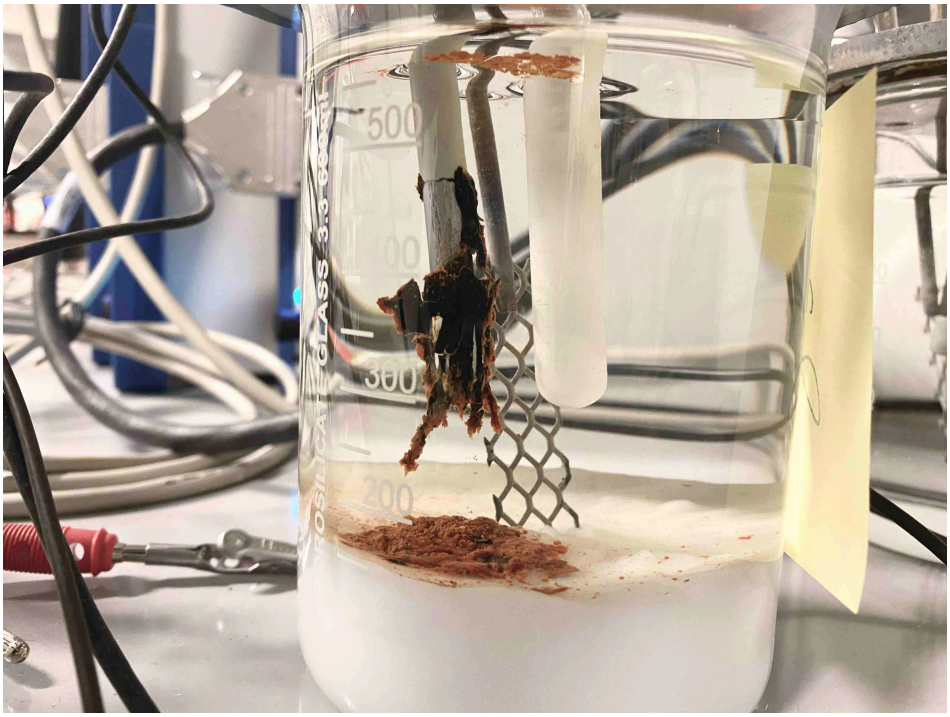

Figure B.6: Image depicting the situation after ended OCP/LPR and polarization measurements for solution 19.

Test Samples

(a) Solution 3

(b) Solution 4

(c) Solution 5B

(d) Solution 9

(e) Solution 14

(f) Solution 19

Figure B.7: Visual inspections of samples displaying signs of corrosion.

Optical Microscope Imaging

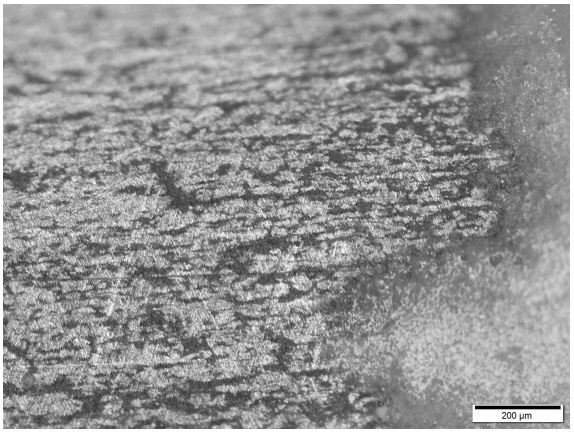

(a) Edge

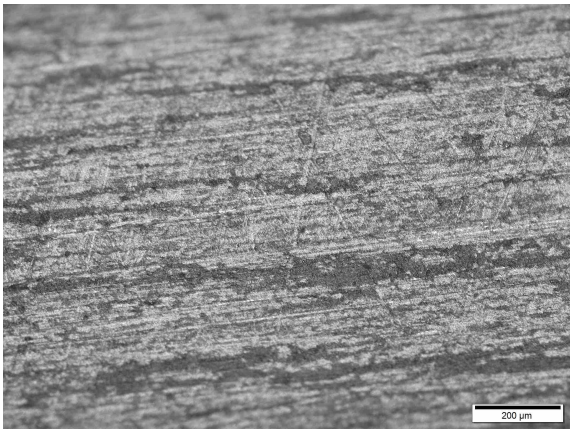

(b) Midsection

Figure B.8: OM imaging of solution 13.

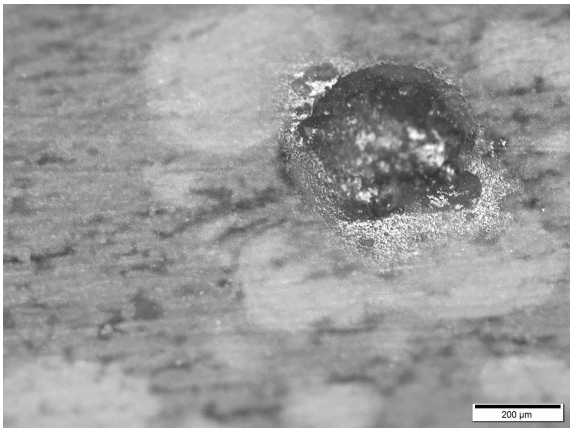

(a) Visible corrosion

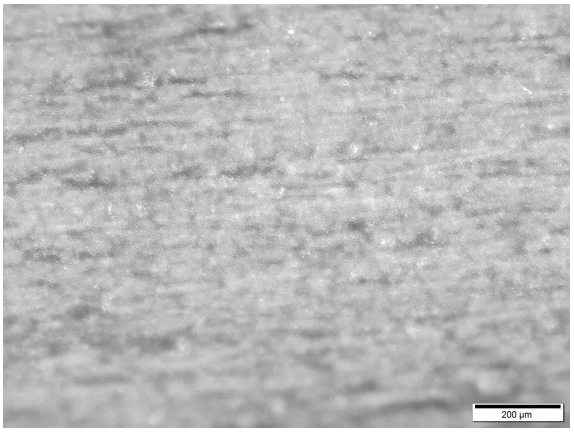

(b) Midsection

Figure B.9: OM imaging of solution 14.

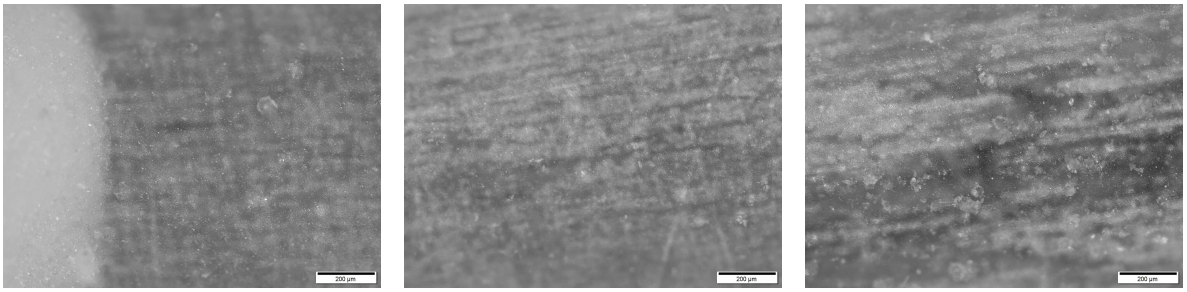

(a) Edge **(b)** Midsection **(c)** Midsection

Figure B.10: OM imaging of solution 16.

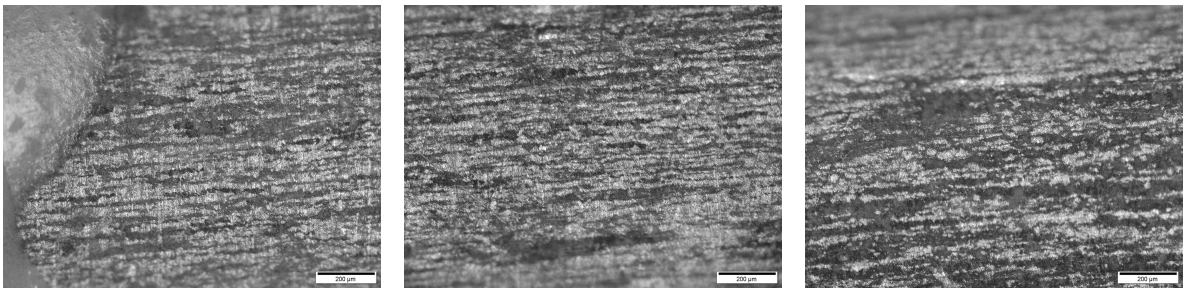

(a) Edge **(b)** Midsection **(c)** Midsection

Figure B.11: OM imaging of solution 21.

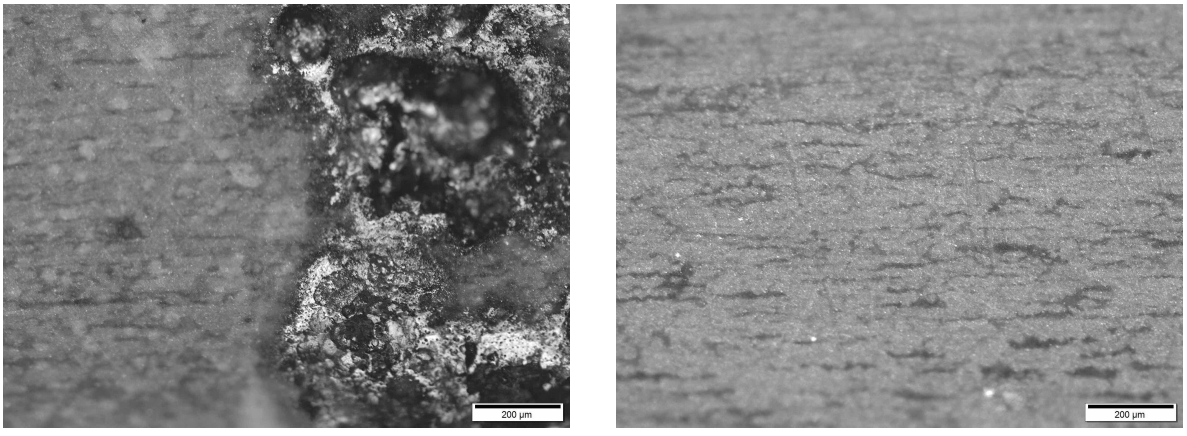

(a) Visible corrosion **(b)** Midsection

Figure B.12: OM imaging of solution 22.

Appendix C

Results from Oxide Layer Analysis

C.1 Mapping Analysis

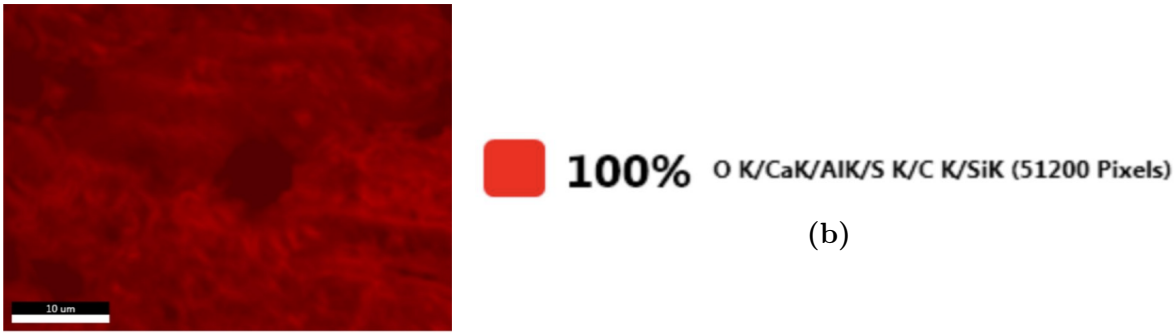

(a) (b)

Figure C.1: Live map from EDS mapping analysis.

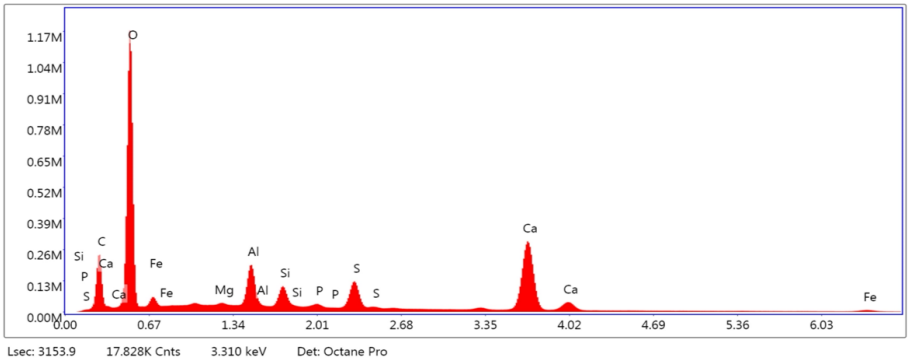

Figure C.2: The sum of the spectrum recorded during the mapping analysis.

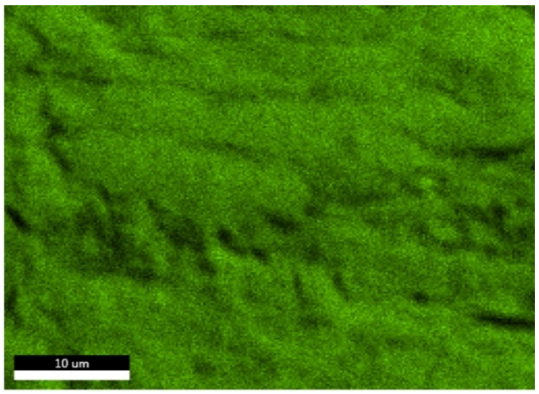

(a) Oxygen content

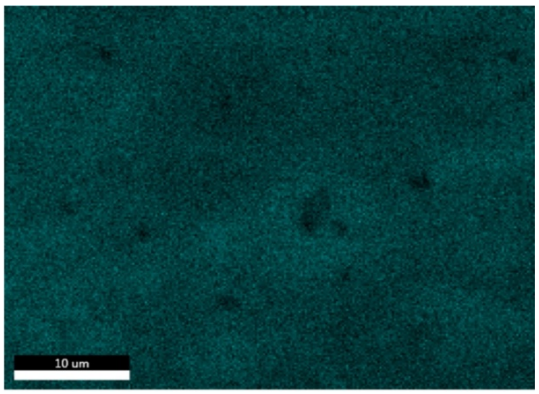

(b) Calcium content

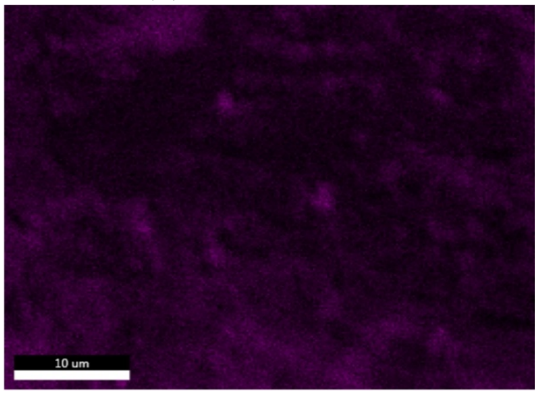

(c) Carbon content

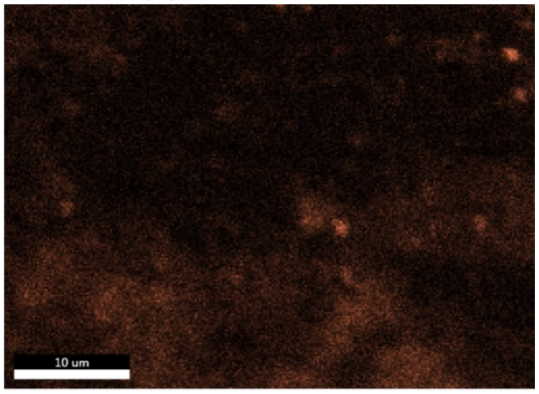

(d) Iron content

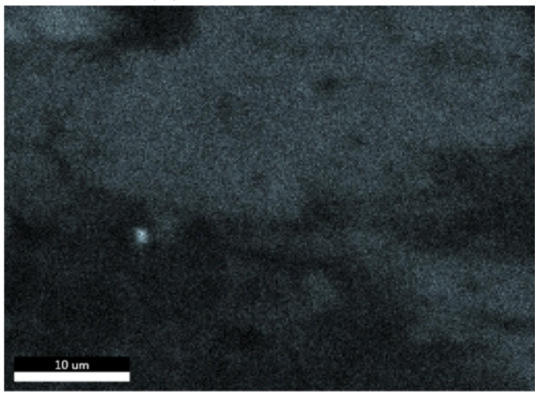

(e) Aluminum content

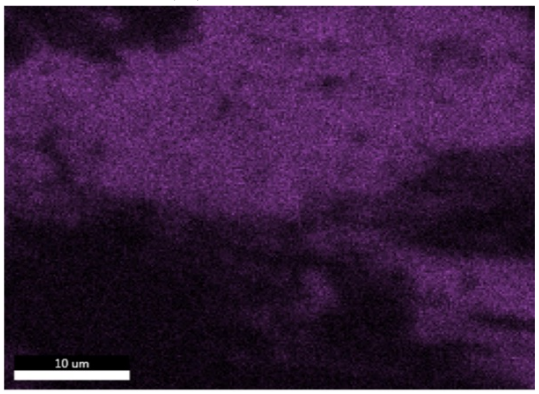

(f) Sulfur content

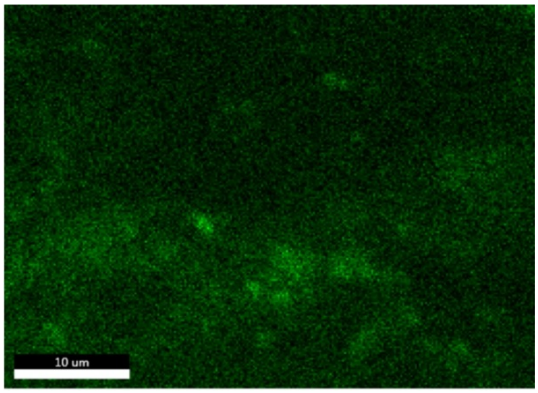

(g) Phosphate content

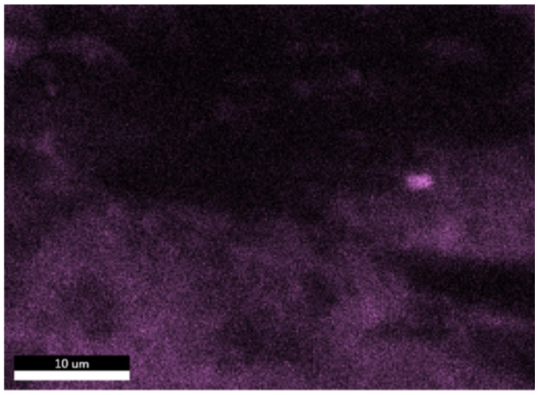

(h) Silicon content

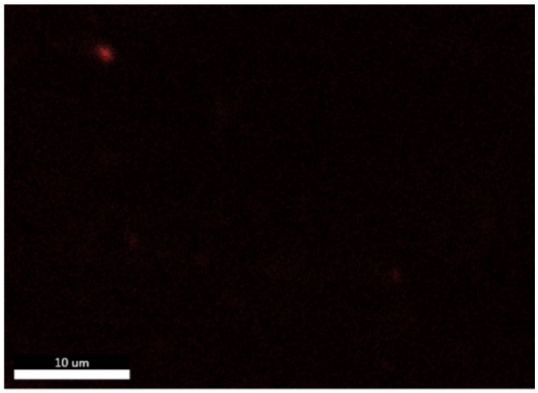

(i) Magnesium content

Figure C.3: Individual element overlays from the EDS mapping analysis.

Appendix D

Results from the Specialization Project

D.1 Method A

Cyclic Polarization Curves

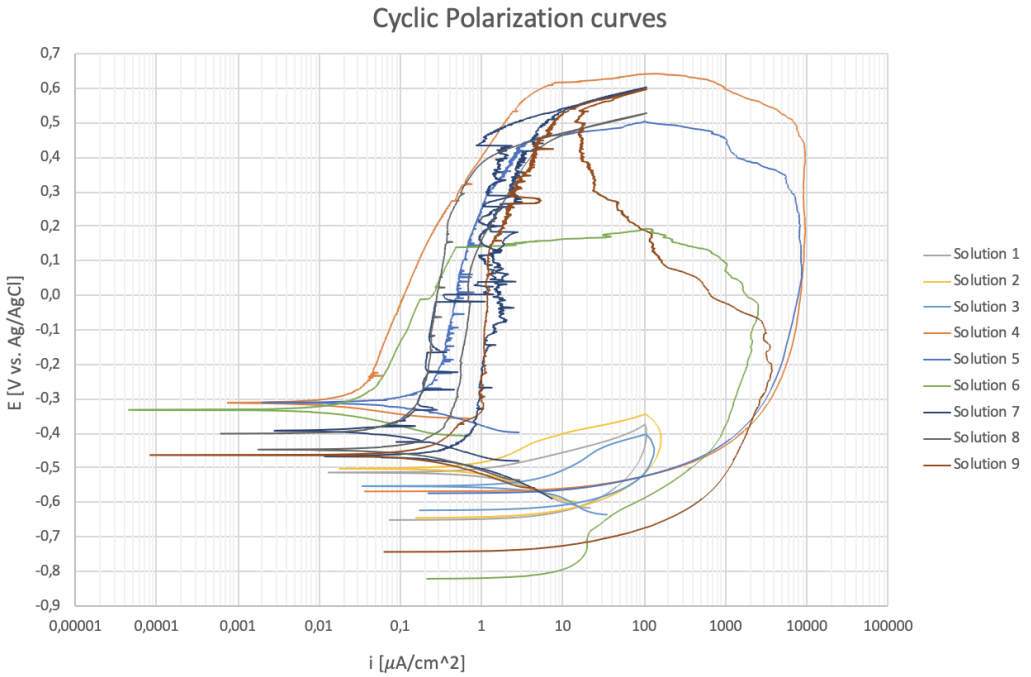

Figure D.1: Plot showing all cyclic polarization curves measured according to ASTM G61 during the specialization project.

Table D.1: Results from method A. Data extracted from the polarization curves shown in Figure D.1

Solution[1]	E_{corr} [$mV_{Ag/AgCl}$]	E_{pit} [$mV_{Ag/AgCl}$]	E_{rep} [$mV_{Ag/AgCl}$]	$I_{pass}1$ [μA]	$I_{pass}2$ [μA]
1	-453	-320	-591	-	376
2	-442	-368	-578	12.2	525.4
3	-493	-386	-546	62.27	460.6
4	-251	657	-508	9.696	35 250
5	-250	494	-513	6.337	26 748.45
6	-272	198	-761	0.99	8497.6
7	-332	526	-390	2.37	8.0746
8	-341	466	NA	8.469	2.224
9	-403	184	-682	4.23	83.532 and 12 314

[1] Solution referred to according to Figure 5.7.

Notes to Table D.1:

- $I_{pass}1$: Average anodic current in the passive region during the increase of the potential.
- $I_{pass}2$: Average anodic current in the passive region during the decrease of the potential.
- - : No passive area present.
- NA: The polarization curve has a positive hysteresis loop, therefore it has no active part.

Visual Inspections

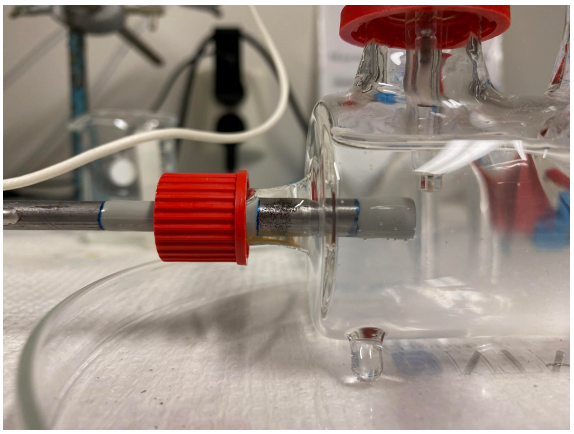

(a) Solution 1

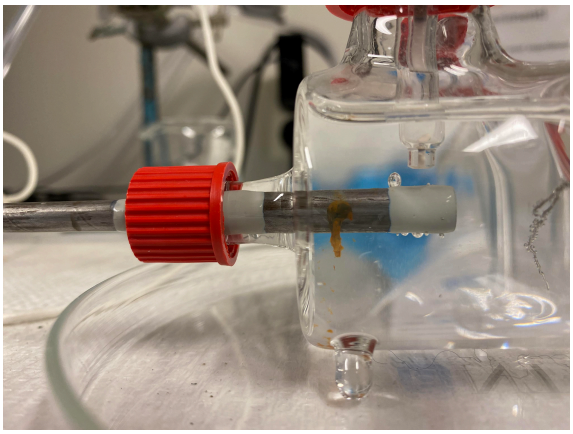

(b) Solution 2

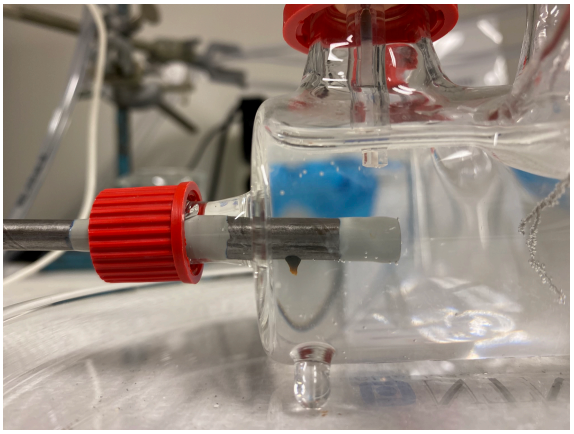

(c) Solution 3

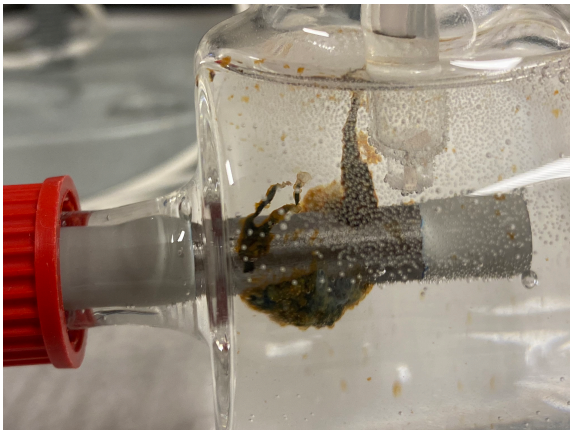

(d) Solution 5

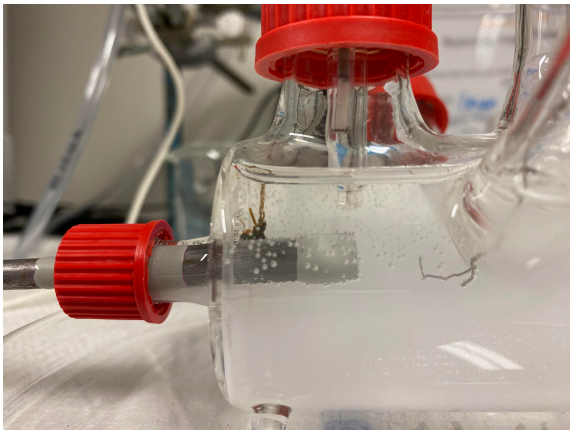

(e) Solution 6

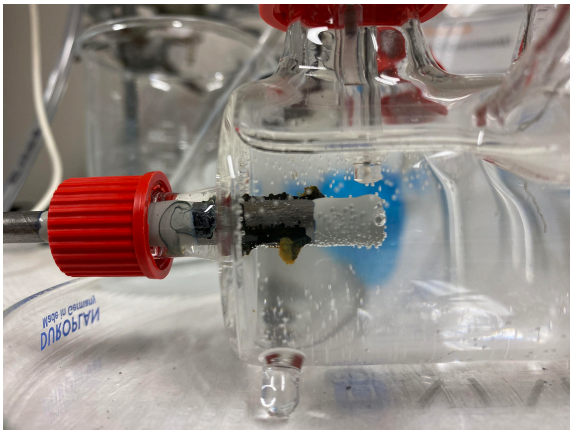

(f) Solution 9

Figure D.2: Images depicting the situation after ended measurements for a selection of the samples.

(a) Solution 1

(b) Solution 2

(c) Solution 3

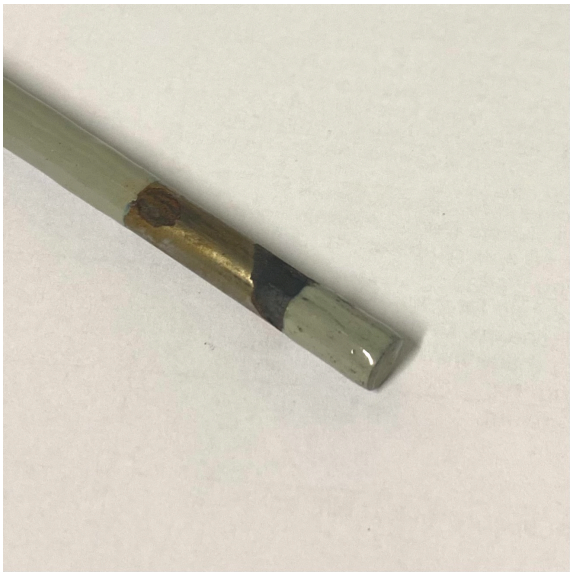

(d) Solution 4

(e) Solution 5

(f) Solution 5 - other side

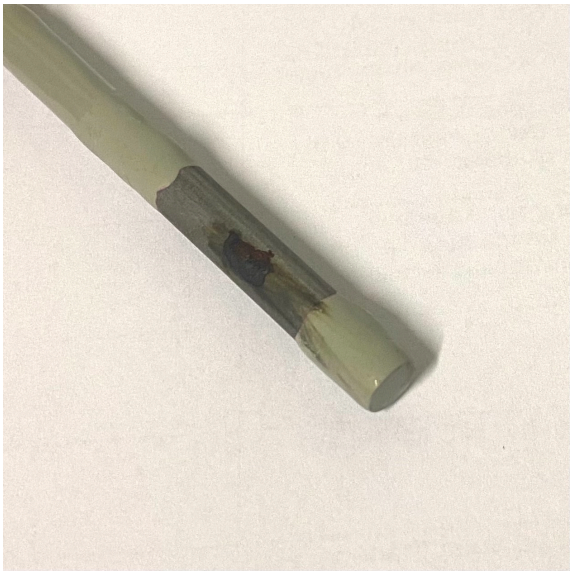

(g) Solution 6

(h) Solution 9

Figure D.3: Visual inspections on the samples that showed corrosion.

The percentage of the surface area covered in corrosion is given in Table D.2. These values are based on visual inspections and simple measurements with a ruler. The table is sorted from the most corroded samples to the least.

Table D.2: The percentage of the surface area subjected to corrosion.

Sample[1]	Percentage of Area Corroded [%]
5	25-30
9	20-25
4	15-20
6	0-5
2	0-5
1	0-5
3	0-5
7	0
8	0

[1] Sample number refers to the solutions given in Figure 5.7.

D.2 Method B

Table D.3: Results from method B.Results from method A. Data extracted from the polarization curves shown in Figure D.5 and Figure D.6.

Solution[1]	OCP-start [$mV_{Ag/AgCl}$]	OCP-finish [$mV_{Ag/AgCl}$]	i_{corr}−start [$\mu A/cm^2$]	i_{corr}−finish [$\mu A/cm^2$]
5A	-224	-452	0.084	1.64

[1] Solution referred to according to Figure 5.8.

Notes to Table D.3:

- OCP-start: Potential measured 1 hour after start.
- OCP-finish: Potential measured at the end of the experiment, after 14 days.
- i_{corr}-start: Corrosion current density calculated from LPR measurements 1 hour after start.
- i_{corr}-finish: Corrosion current density calculated from LPR measurements at the end of the experiment, after 14 days.

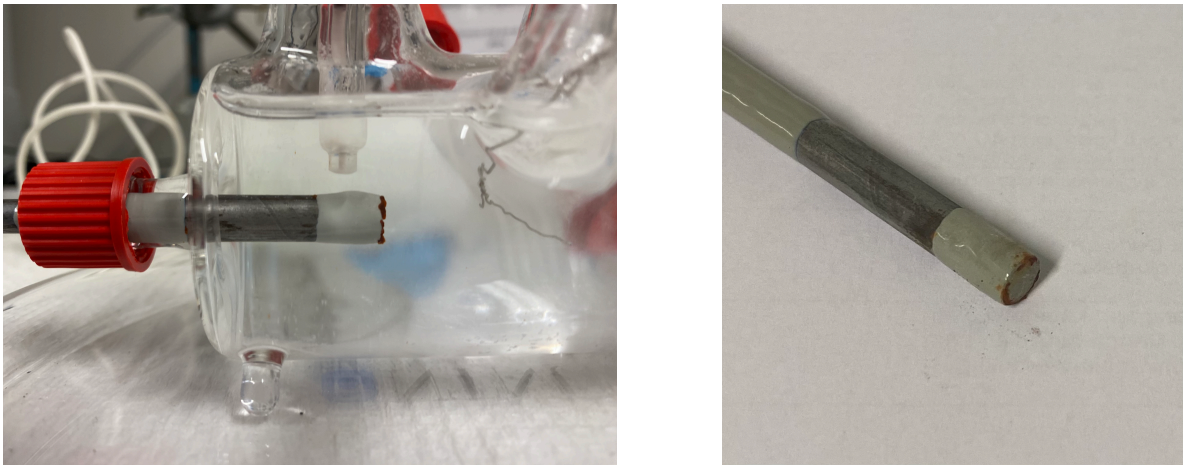

Figure D.4: Sample 5 after 14 days of testing.

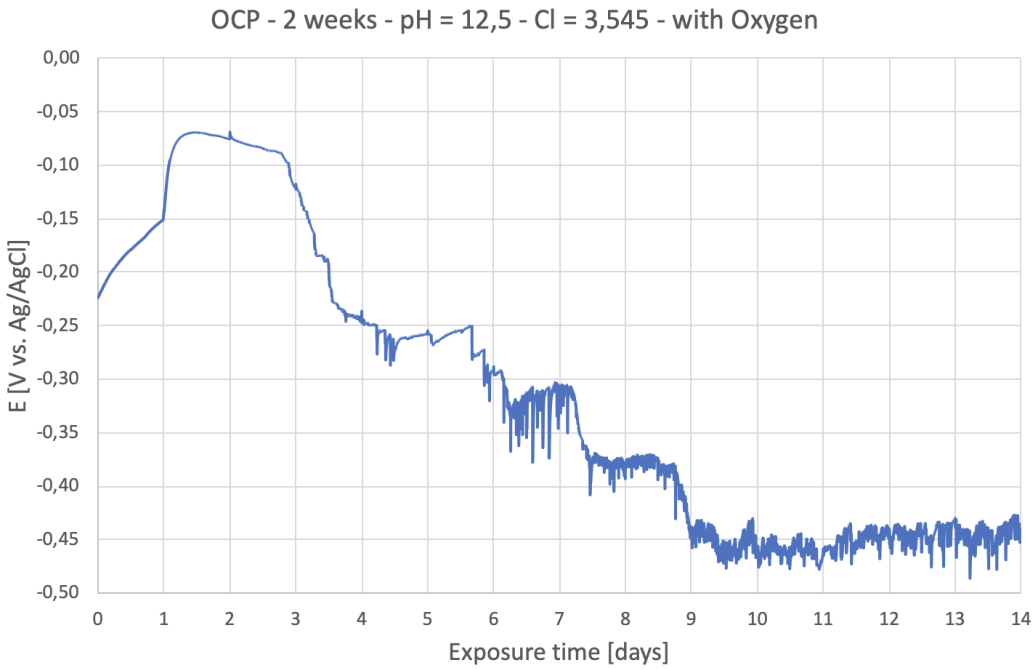

Figure D.5: OCP development for solution 5 during 2 weeks of exposure.

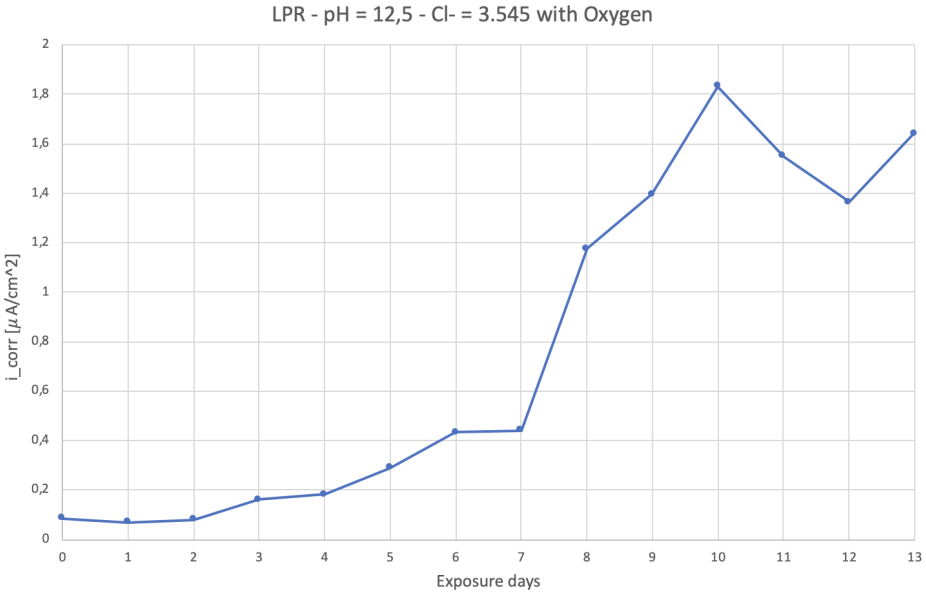

Figure D.6: Calculated corrosion current density development based on LPR measurements during 2 weeks of exposure.

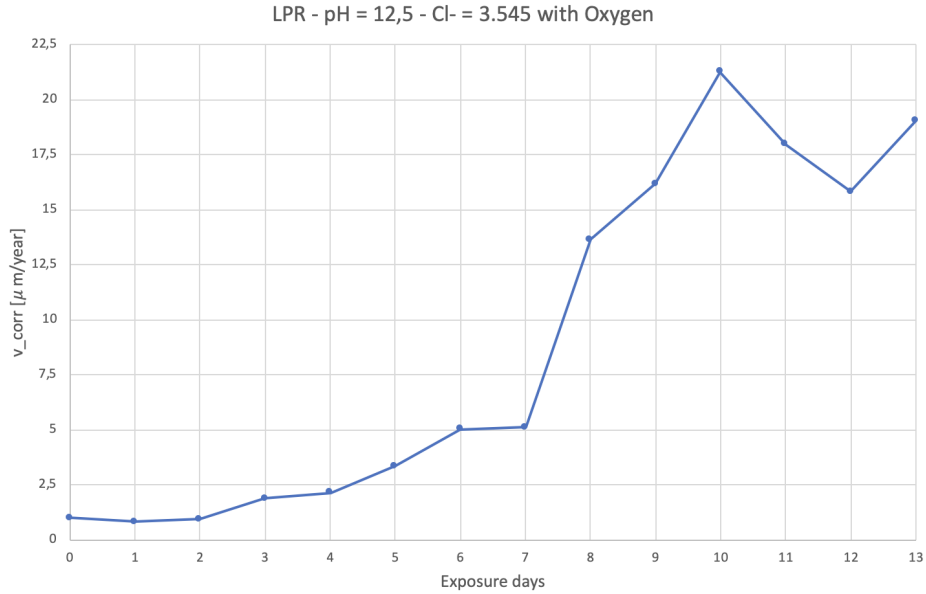

Figure D.7: Calculated corrosion rate development based on LPR measurements during 2 weeks of exposure.

The plot in Figure D.6 and Figure D.7 was calculated using Equation 5.2 and Equation 5.4, respectfully.

D.3 Oxide Layer

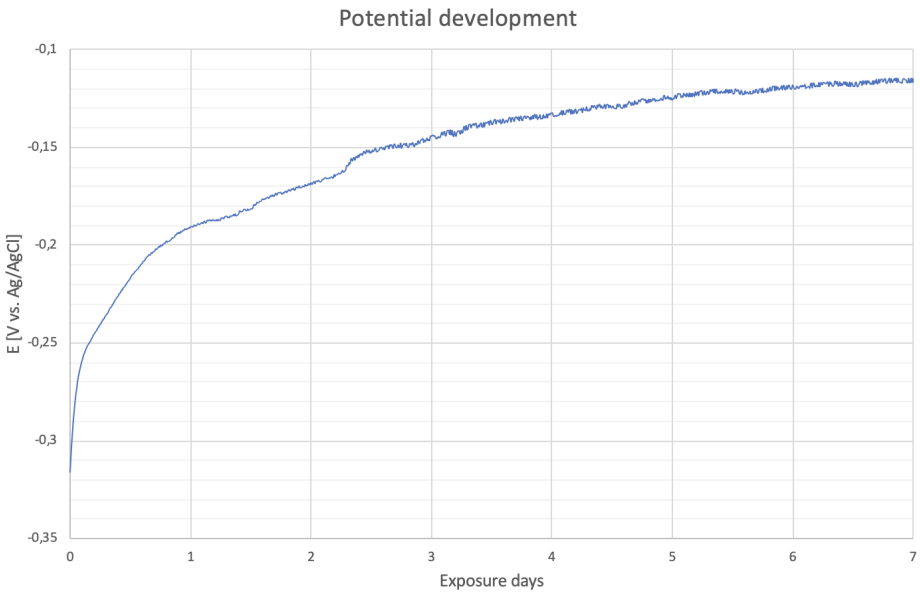

Figure D.8: The potential development on sample during the buildup of oxide layer.

Figure D.9: Left sample: with oxide layer. Right sample: without oxide layer.

SEM Analysis

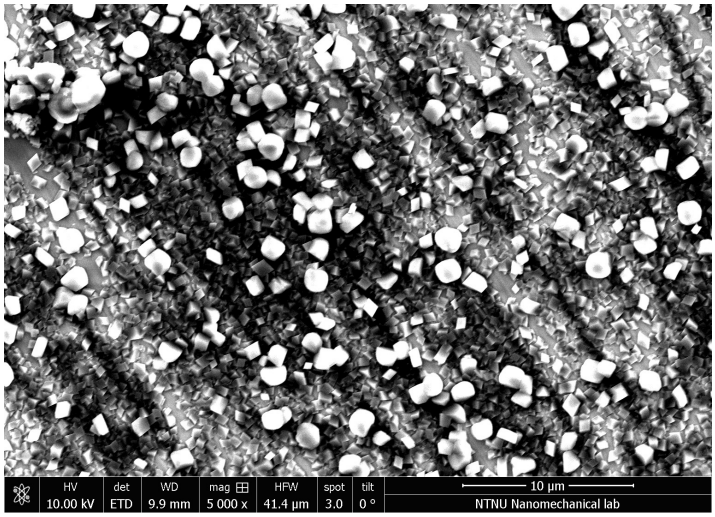

Figure D.10: Image taken with SEM at a magnification of 5000x.

EDS Analyses

Point Analysis

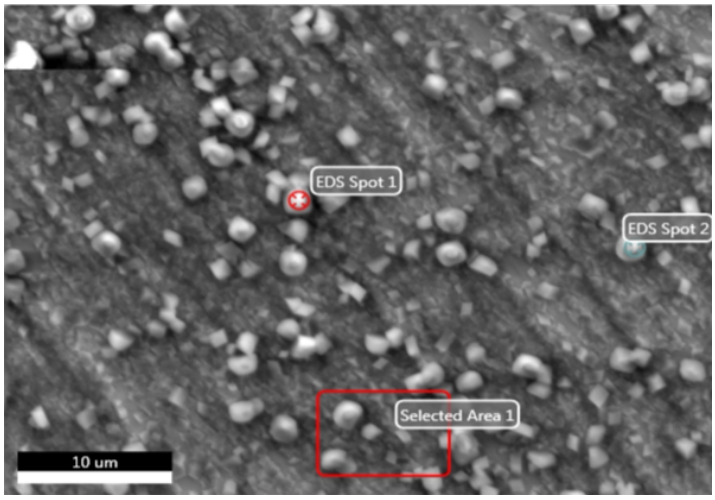

Figure D.11: The overview over the sites used for the point analyses.

Table D.4: Lists the average results from the EDS point analysis given in Figure D.12.

Element	Weight %	Atomic %	Error %
C	11.06	19.40	6.42
O	43.93	57.71	9.16
Fe	5.20	2.02	43.59
Ca	39.80	20.87	3.79

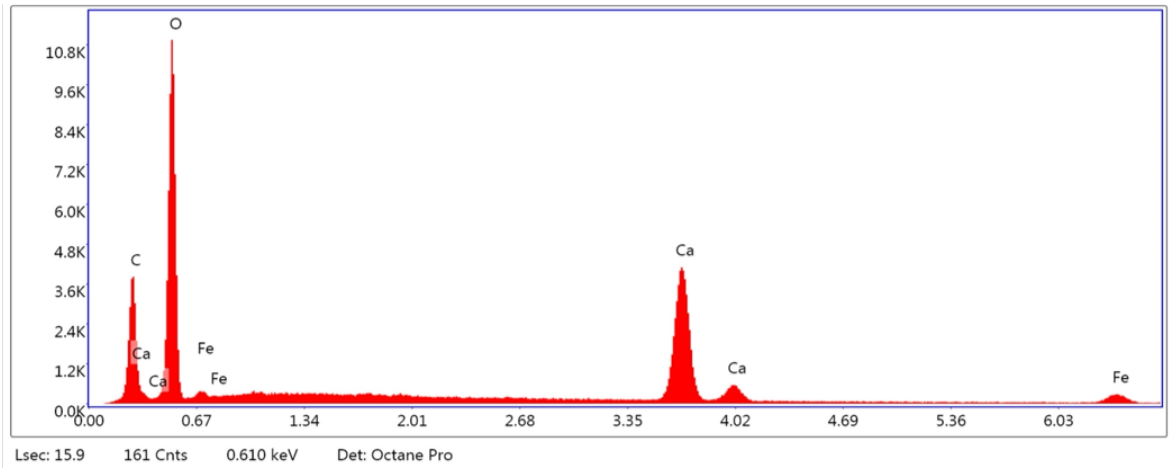

(a) Point analysis from spot 1.

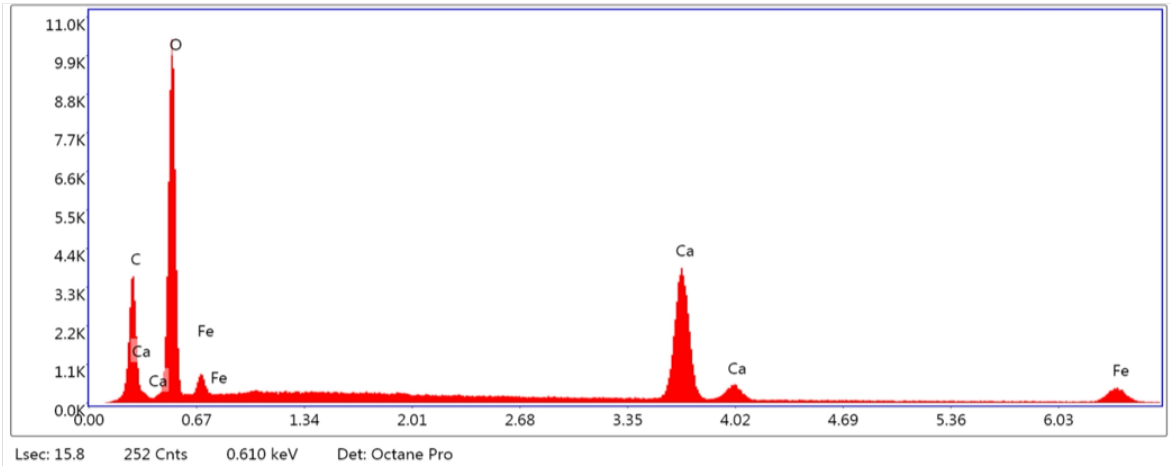

(b) Point analysis from spot 2.

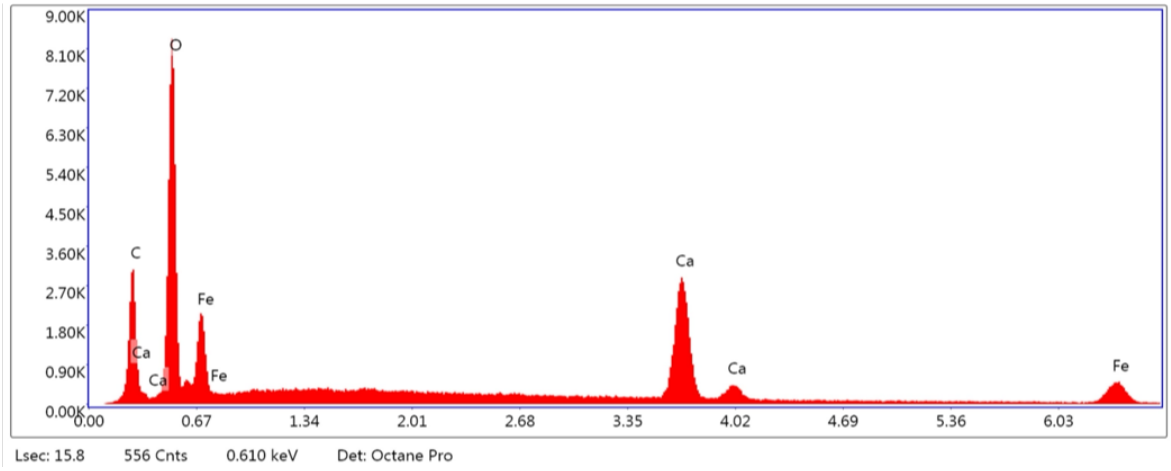

(c) Point analysis from area 1.

Figure D.12: Spectrum analyses from the EDS point analysis.

Mapping Analysis

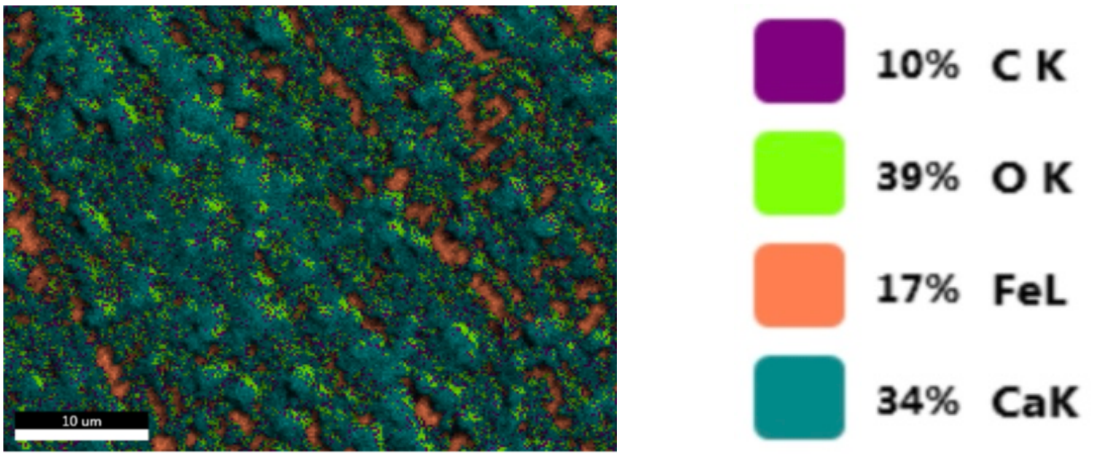

(a) (b)

Figure D.13: Shows the element overlay map with explanations and results from the EDS mapping analysis.

Table D.5: Results from the EDS mapping analysis.

Element	Weight %	Atomic %	Error %
C	9.71	18.88	6.24
O	35.96	52.50	8.49
Fe	18.51	7.74	7.03
Ca	35.83	20.88	3.02

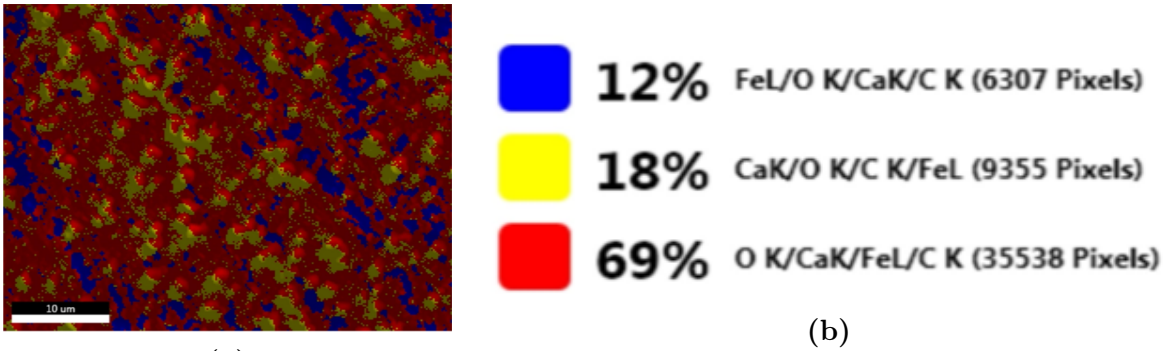

(a) (b)

Figure D.14: Live map from EDS mapping analysis.

Table D.6: Results from the FeL/O K/CaK/C K phase (blue area).

Element	Weight %	Atomic %	Error %
C	8.80	23.02	7.89
O	15.80	31.03	7.36
Fe	59.50	33.48	5.09
Ca	15.90	12.47	3.78

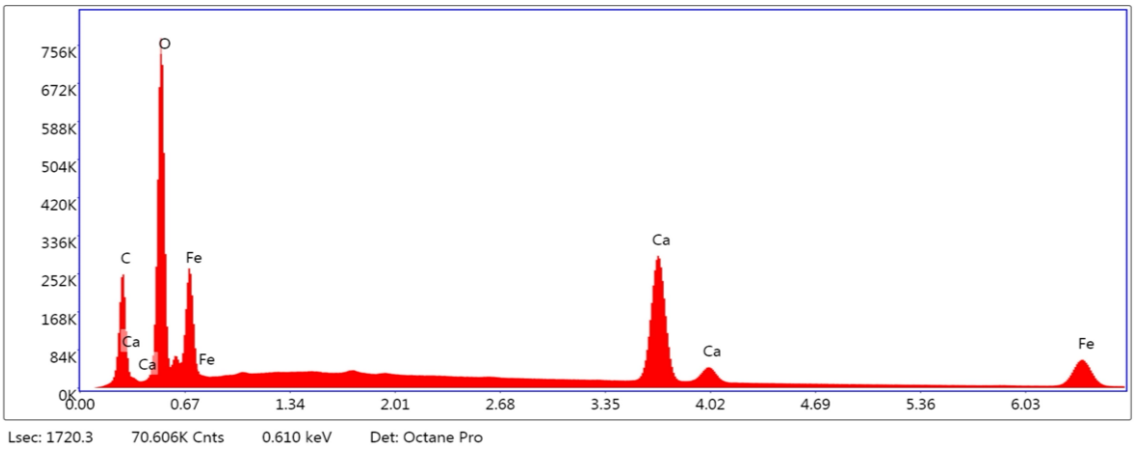

Figure D.15: Shows the sum of the spectrum recorded during the EDS mapping analysis.

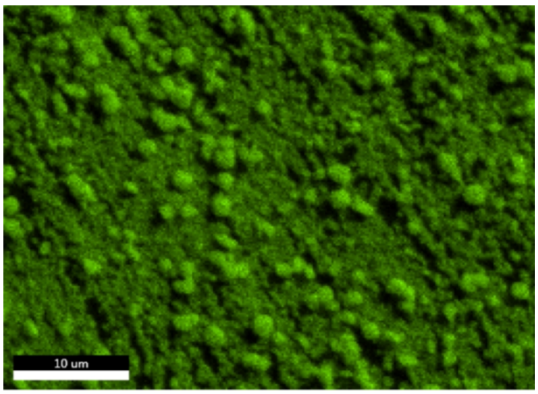

(a) Oxygen content

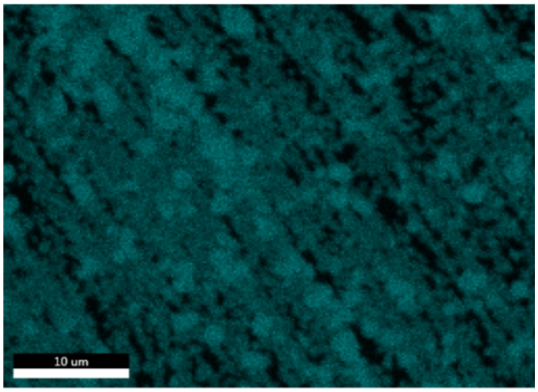

(b) Calcium content

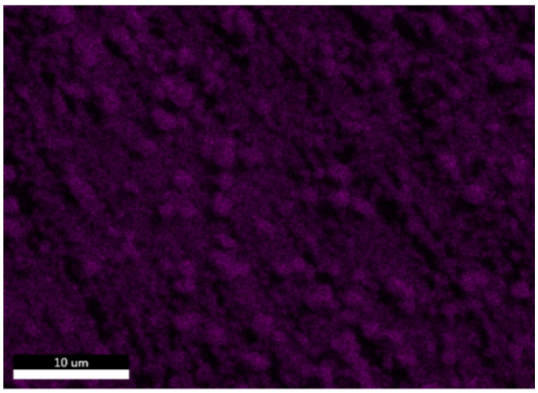

(c) Carbon content

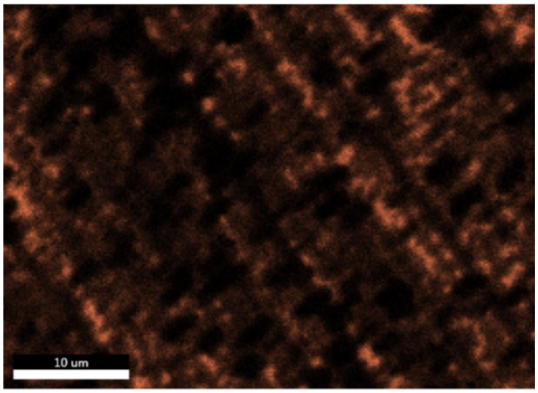

(d) Iron content

Figure D.16: Individual element overlay from EDS mapping analysis.

Appendix E

Images From the Site

All images are gathered from a 2021 report by Roy Johnsen [79].

E.1 Focus on corrosion

Figure E.1: Images taken from inspection site 1. Corresponds to image E1-1 to E1-4 in Appendix F, respectively

Figure E.2: Images taken from inspection site 2. Corresponds to image E1-5 to E1-9 in Appendix F, respectively

Figure E.3: Images taken from inspection site 3. Corresponds to image E1-10 to E1-17 in Appendix F, respectively

E.2 Focus on the grout

Figure E.4: Images taken from inspection site 1. Corresponds to image E2-1 to E2-4 in Appendix F, respectively

Figure E.5: Images taken from inspection site 2. Corresponds to image E2-5 to E2-7 in Appendix F, respectively

Figure E.6: Images taken from inspection site 3. Corresponds to image E2-8 to E2-11 in Appendix F, respectively

Appendix F

Image descriptions

A description of the images displayed in the figures in Appendix E. Image numbers are given in the captions of the figures.

Image number	**Camera**	**Motive**
E1-1	Mobile	Surface corrosion on all armour wires, some signs of cross sectional area reduction.
E1-2	Mobile	Same as E1-1.
E1-3	Endoscope	Large differences regarding the corrosion on the wires. The wires on the bottom of the duct show greater signs of corrosion compared to the ones on top. Can also see signs of frost deteriorated grout.
E1-4	Endoscope	Can see signs of corrosion in the form of black "pearls".
E1-5	Mobile	Corroded reinforcement bars.
E1-6	Mobile	Corrosion on all armour wires. The ones on the bottom show again a higher degree of corrosion compared to the ones on top. Shows also crumbled grout.
E1-7	Mobile	Corroded armour wires are being bent by a crowbar.
E1-8	Mobile	Same as E1-7.
E1-9	Mobile	Depicts the situation right after a wire was cut with an angle grinder. A retraction of approximately 3 cm is visible.
E1-10	Mobile	Heavily corroded armour wires. Shows signs of pitting corrosion and shows a fracture in one of the wires. The grout is heavily crumbled.
E1-11	Mobile	The lower side of the duct after the grout has been removed. Signs of heavy corrosion on the wires.
E1-12	Mobile	Piece extracted from the inside of a duct.
E1-13	Mobile	Piece extracted from the outside of a duct.
E1-14	Mobile	A loose wire that has most likely fractured due to corrosion.
E1-15	Mobile	Cut armour wires.

Image number	**Camera**	**Motive**
E1-16	Mobile	Fracture of a armour wire as a result of corrosion. High degree of corrosion on surrounding wires. Moist grout containing corrosion products. No corrosion on the outside of the duct.
E1-17	Mobile	A section of an armour wire showing a reduction in the cross sectional area.
E2-1	Endoscope	The topside of the duct showing signs of corrosion. Dry grout but incomplete filling.
E2-2	Endoscope	Bottom side of a duct. No grout present and corrosion along the inside of the duct.
E2-3	Endoscope	Close up of the armour wires and showing the state of the crumbled grout and low degree of filling.
E2-4	Endoscope	The grout is crumbled and there is incomplete filling around the wires.
E2-5	Mobile	Frost detriorated grout (light yellow powder) and solid grout (gray lumps).
E2-6	Mobile	Solid grout close to the surface of the armour wires.
E2-7	Mobile	Image taken close to the injection point ($\sim$ 6m). Should have been a complete filling, but only signs of grout in the top part of the duct. The filling is separated - signs of evaporated water. The grout present show signs of frost deterioration.
E2-8	Mobile	Wet grout. Samples brought back in bag for further testing.
E2-9	Mobile	Showing the surrounding area where a wire had fractured. Frost deteriorated grout can be seen at the bottom of the duct in addition to a low degree of filling. No sign of corrosion on the reinforcement bar below. Solid concrete.
E2-10	Endoscope	The grout found in the duct is moist and crumbled. Shows the duct facing west of the fracture.
E2-11	Endoscope	The grout found in the duct is moist and crumbled. Shows the duct facing east of the fracture.

Bettina Horn Myhre

Effects of chloride, sulfate and pH on the corrosion of tensile wires in grouted tendon ducts in Herøysundet bridge

NTNU
Kunnskap for en bedre verden